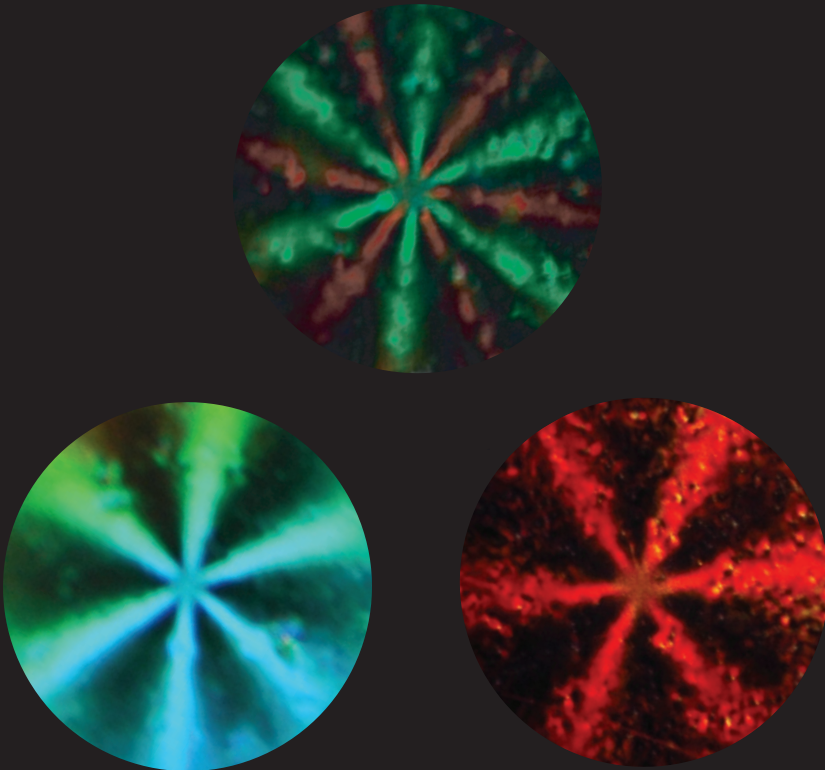


# Control over colloidal crystallization by shear and electric fields



Yu Ling Wu

**Control over colloidal  
crystallization by shear and  
electric fields**

ISBN: 978-90-39345-26-9

A digital (color) version of this thesis is available at <http://www.colloid.nl>

# **Control over colloidal crystallization by shear and electric fields**

**Controle over colloïdale kristallisatie via  
vloeistofstromingen en elektrische velden**

(met een samenvatting in het Nederlands)

## **Proefschrift**

ter verkrijging van de graad van doctor aan de Universiteit Utrecht op gezag  
van de rector magnificus, prof.dr. W.H. Gispen, ingevolge het besluit van het  
college voor promoties in het openbaar te verdedigen op

**woensdag 16 mei 2007 des ochtends te 10.30 uur**

door

**Yu Ling Wu**

geboren op 18 juni 1980 te Amsterdam



Promotor: prof. dr. A. van Blaaderen  
Co-promotor: dr. A. Imhof

This work is part of the research programme of the ‘Stichting voor Fundamenteel Onderzoek der Materie (FOM), which is financially supported by the ‘Nederlandse Organisatie voor Wetenschappelijk Onderzoek (NWO)’.

*“Een nieuwe lente en een nieuw geluid:”*

Herman Gorter



# Contents

<b>1</b>	<b>Introduction</b>	<b>1</b>
1.1	Colloids . . . . .	1
1.2	Shear flow . . . . .	2
1.3	Electric fields . . . . .	4
1.4	Permanent structures . . . . .	6
1.5	Scope of this thesis . . . . .	7
<b>2</b>	<b>A new parallel plate shear cell</b>	<b>9</b>
2.1	Introduction . . . . .	10
2.2	Shear cell construction . . . . .	11
2.2.1	Layout of the shear cell . . . . .	11
2.2.2	Design of a high precision shear cell . . . . .	12
2.2.3	Design of the stages . . . . .	13
2.2.4	The motor stages . . . . .	15
2.2.5	Cassette design . . . . .	15
2.2.6	Cassette alignment . . . . .	15
2.2.7	The control loop . . . . .	17
2.3	Operation . . . . .	18
2.4	Experimental . . . . .	20
2.4.1	Determination of the alignment and motion of the plates	20
2.4.2	Characterization of the flow profile . . . . .	21
2.4.3	Observation of shear induced crystallization and melting of colloidal dispersions . . . . .	22
2.5	Results and discussion . . . . .	22
2.5.1	Determination of the alignment and motion of the plates	22
2.5.2	Characterization of the flow profile . . . . .	29
2.5.3	Observation of shear induced crystallization and melting of colloidal dispersions . . . . .	31
2.6	Conclusion . . . . .	32
<b>3</b>	<b>Colloidal suspensions under shear</b>	<b>33</b>
3.1	Introduction . . . . .	34
3.2	Experimental details . . . . .	35
3.3	Results and discussion . . . . .	37
3.3.1	Flow profile of crystallizing suspensions . . . . .	37
3.3.2	Motion of crystalline layers . . . . .	40
3.3.3	Shear induced melting and crystallization . . . . .	42
3.4	Conclusions and outlook . . . . .	48

<b>4</b>	<b>Formation of colloidal crystals by spin coating</b>	<b>51</b>
4.1	Introduction . . . . .	52
4.2	Theory of spin coating . . . . .	53
4.3	Experimental details . . . . .	55
4.3.1	Dispersions . . . . .	55
4.3.2	Spin coating of films . . . . .	56
4.3.3	Microscopy . . . . .	57
4.3.4	Refractive index measurements . . . . .	57
4.4	Results and discussion . . . . .	57
4.4.1	Refractive index . . . . .	57
4.4.2	Film thickness . . . . .	58
4.4.3	White light illumination . . . . .	59
4.4.4	3D structure determination with confocal microscopy . .	60
4.5	Conclusion . . . . .	74
<b>5</b>	<b>Freestanding films of colloidal crystals</b>	<b>77</b>
5.1	Introduction . . . . .	78
5.2	Experimental details . . . . .	79
5.2.1	Making freestanding films . . . . .	79
5.2.2	Selective removal of the polymer matrix . . . . .	80
5.2.3	Selective removal of the silica particles . . . . .	81
5.2.4	Spectroscopy . . . . .	81
5.2.5	Ion beam deformation . . . . .	81
5.3	Results and discussion . . . . .	81
5.3.1	Freestanding films . . . . .	81
5.3.2	Selective removal of the polymer matrix . . . . .	82
5.3.3	Selective removal of the silica particles . . . . .	87
5.3.4	Spectroscopy . . . . .	89
5.3.5	Ion beam deformation . . . . .	90
5.4	Conclusion . . . . .	91
<b>6</b>	<b>Epitaxial colloidal crystal growth</b>	<b>95</b>
6.1	Introduction . . . . .	96
6.2	Colloids in electric fields . . . . .	97
6.3	Experimental details . . . . .	98
6.3.1	Fabrication of patterned electrodes . . . . .	98
6.3.2	Conservation of the template . . . . .	100
6.3.3	Electric field cell . . . . .	102
6.3.4	Colloidal systems . . . . .	102
6.4	Results and discussion . . . . .	103
6.4.1	Fabrication of patterned electrodes . . . . .	103
6.4.2	Guiding the attachment of dipolar particle strings . . .	106
6.5	Conclusion and outlook . . . . .	110

*CONTENTS*

ix

<b>Bibliography</b>	<b>113</b>
<b>Summary</b>	<b>125</b>
<b>Samenvatting voor iedereen</b>	<b>127</b>
<b>Dankwoord</b>	<b>131</b>
<b>Curriculum vitae</b>	<b>133</b>



# 1

## Introduction

### 1.1 Colloids

Colloids play an important role in everyday life. Without noticing we encounter them very frequently. Some examples of colloidal systems are milk, blood, smoke and foams. What do these examples have in common and why are they called colloids? It is the size that matters. Colloids are entities with at least one characteristic length in the size range from a few nanometers to a few micrometers. They are dispersed in a medium that can be regarded as a continuum because it consists of units much smaller than the colloids. Both the colloids and the surrounding medium can be a gas, liquid or solid. Milk is a system of fat droplets in water (an emulsion), blood is a dispersion of red blood cells in serum, smoke is a collection of solid particles in a gas and a foam can either consist of gas bubbles in a liquid, e.g. beer, or in a solid, e.g. zeolites.

Thomas Graham, often called the father of colloid chemistry, was the one who gave the colloid its name. Graham was studying osmosis and observed that some substances of an aqueous solution could pass a parchment membrane, whereas others could not. He called the apparently larger substances that stuck to the membrane “colloid”, after the Greek word *κόλλα* meaning glue.

Because colloids are large compared to molecules, but small compared to for example granular matter, they show Brownian motion. This erratic diffusive motion was observed soon after the appearance of the microscope, but at first scientists thought that it had some living origin. In 1827 Robert Brown [1] and Adolphe Brongniart [2] independently were the first to claim that this motion was a fundamental physical property [3]. Molecules of the surroundings are continuously colliding with every object. In the case of large macroscopic objects, the forces that are exerted via these collisions are balanced in all directions and are giving rise to what we call pressure. However, colloids are so small that the forces momentarily do not average out in all directions and



therefore colloids show an erratic, Brownian motion. This motion ensures that colloids can move through space and that they can self-organize until their free energy is minimal.

At low particle volume fractions, colloids are randomly distributed in a liquid-like fashion. When the volume fraction reaches  $\phi_f = 0.494$ , a dispersion of colloids that interact via a hard-sphere potential starts to crystallize and liquid and solid coexist. Above the melting transition at  $\phi_m = 0.545$ , a dispersion of hard-sphere like colloids is completely crystalline. [4, 5]

Colloidal crystals with various symmetries exist. For specific symmetries a photonic crystal has a band gap, provided that the dielectric contrast between the particles and the surrounding medium is large enough. A photonic crystal with a band gap is a material in which the dielectric constant varies periodically such that a photon within a certain frequency range cannot propagate inside the crystal. They can for example be used as optical filters and waveguides [6].

To make colloidal crystals useful for applications, they have to be large and single crystalline. However, when no special effort is made, they are usually small and polycrystalline. Therefore, we use external fields to control colloidal crystallization and to make large aligned crystals. Moreover, external fields can be used to manipulate the symmetry of the structures. Examples of commonly used external fields to make colloidal crystals are: gravity [7], electric fields [8], shear flow [9–11] and confinements [12]. In this thesis we will use shear flow and an electric field to control colloidal crystallization.

## 1.2 Shear flow

Simple shear flow is a special type of flow in which there is only one non-zero velocity component with a velocity gradient perpendicular to the velocity direction, the shear rate  $\dot{\gamma}$ . Examples are a flow between two parallel plates that move along a line or a Poiseuille flow in a tube.

Shear can be used to make colloidal particles order. Sawada and co-workers [11, 13] used a Poiseuille flow to make colloidal crystals of charged polystyrene particles in water. They applied a momentary strong flow by which the particles arranged in hexagonal layers at locations where the local shear rate was sufficiently high. The shear flow brought the system out of equilibrium, but when the nonequilibrium ordered structure was close to the equilibrium structure, the well-oriented crystal structure was maintained after cessation of the high shear.

Amos *et al.* [14–16] used a parallel plate setup to shear-align hard sphere-like polymethylmethacrylate (PMMA) particles in dodecane or octanol. Face centered cubic (FCC) crystals formed. In this crystal structure hexagonal layers are ABC stacked, where A, B and C are the lateral positions of the layers. Often, an FCC crystal of ABC stacked layers combined with its mirror image of CBA stacked layers, a so-called twinned crystal forms. Amos *et*

*al.* showed that only one of the mirror images formed, when shearing in one direction and that the other mirror image formed, when shearing in the other direction. After cessation the crystal relaxed to a twinned FCC crystal. When they applied a shear in a 2D scheme by moving the plates in a closed triangular loop, i.e. successively in three directions  $120^\circ$  apart, they obtained only one of the stacking types. After cessation of this 2D shear, the crystal remained in the pure FCC form.

Different crystal structures are obtained when an additional external field is applied. Cohen *et al.* [17] combined shear flow and confinement. When the number of layers exceeded 11, the symmetry of the crystal was identical to that of bulk suspensions. However, when the gap of the shear cell contained less than 11 layers and if the gap width was incommensurate with an integer number of layers, the layers buckled in a regular way in order to pack more efficiently.

Also with other types of flow colloidal crystals have been made. By melt compression Ruhl *et al.* [18–20] formed colloidal crystals with sizes up to 1 mm in thickness and 10 cm in diameter. Their system consisted of hard-soft core-shell particles. A hard core made of polystyrene was coated with a layer of PMMA and covered with a soft shell of poly(ethyl acrylate). The latex dispersion was heated and compressed uniaxially to allow the melt of the latex spheres to flow sideways. Except at the center where the shear rate was close to zero, the particles arranged in hexagonal layers parallel to the plates.

Another technique to make colloidal crystals is spin coating. With this simple method Jiang and McFarland [21] fabricated colloidal crystalline films as large as 4 inch in diameter. By tuning the spin speed and spin time they were able to set the film thickness. Also monolayers can be made with this technique [22, 23].

To examine the microstructure under shear usually scattering techniques are used [9, 24–27]. This gives a wealth of information. It was for example found that shear makes colloidal particles arrange in hexagonal layers parallel with the velocity-vorticity plane. A close-packed line is oriented along the flow direction. However, the mechanisms behind shear induced structure formation are complicated and there is a need for real-space observations. Fuller and co-workers [28, 29] observed the effect of shear flow on 2D layers of polystyrene particles at the interface between decane and water. They used a dual band shear cell that consisted of two o-rings moving parallel to each other in opposite direction. While a shear was applied the particles were monitored with a microscope to which a CCD camera was attached. Real-space measurements on 3D systems were done e.g. by Tolpekin *et al.* [30]. They studied aggregation and breakup of colloidal particle aggregates under shear with video microscopy. However, they were only able to examine the bottom part of the shear cell and the objects were moving out of the field of view during the measurement. Under shear the aggregates appeared smeared out in images making it impossible to

determine the structures on a single-particle level. In addition, the resolution in  $z$ , perpendicular to the flow direction was low.

With confocal microscopy also a differentiation in depth can be made. The confocal microscope was invented by Minsky [31]. Only the plane that is in focus is illuminated by placing a pinhole close to the light source and by focussing the light to a point. In front of the detector a second pinhole is placed. This selects only the light that comes from the plane that is in focus. In 1995, the first quantitative 3D datasets of colloidal structures, crystals and glasses were obtained [32].

Confocal microscopy has been shown to be beneficial in for example the determination of the stacking of hexagonal layers that form under shear. With scattering techniques only the average stacking order can be determined, but by using confocal microscopy Solomon and Solomon [33] were able to determine the local stacking of shear induced colloidal crystals. Because the structure moved by the flow and the data acquisition time is finite, they had to stop shearing before taking the data.

Derks *et al.* [34] used a shear cell with which it was possible to study colloidal suspensions with confocal microscopy under shear. To prevent the particles in the focal plane from moving out of the field of view, the shear cell was designed with a zero-velocity plane, i.e. a plane that does not move with respect to the laboratory coordinate system. This concept was invented by Taylor [35] and was first only incorporated in shear cells to which an optical microscope was coupled [36–38]. Derks *et al.* used a cone-plate shear cell with a zero-velocity plane that was mounted on top of a confocal microscope. They were able to examine the structure in 3D on a single-particle level. In confocal microscopy high numerical aperture objective lenses are used and they have a limited working distance of about 100  $\mu\text{m}$ . The gap width of the cone-plate shear cell of Derks *et al.* was too large to be able to examine the complete gap. Complex fluids may exhibit complicated flow profiles and one therefore wants to be able to observe the complete gap. Therefore, we developed a new parallel plate shear cell with a variable, but small gap width to enable visualization of the complete gap with a confocal microscope. Images like the one in Figure 1.1 can then be taken. Additionally, this new shear cell can both apply an oscillatory and a continuous shear. Moreover, the shear cell is of a modular design and it can be adapted such that it is possible to apply an electric field in addition to a shear.

### 1.3 Electric fields

Electric fields are also used to control the assembly of colloidal crystals. Both direct current (DC) [39] and alternating current (AC) [8] electric fields have been used. For the experiments described in this thesis, we used high frequency (1 MHz) alternating current electric fields. In a high frequency AC

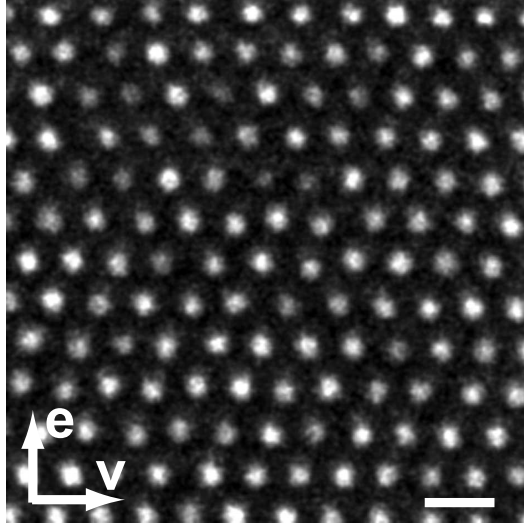


**Figure 1.1:** Confocal micrograph taken under shear of a layer of  $1.2\ \mu\text{m}$  diameter silica particles in the zero-velocity plane. The velocity direction,  $v$ , is from left to right, the vorticity direction,  $e$ , from bottom to top. The scale bar is  $2\ \mu\text{m}$ .

electric field, particles can acquire an induced dipole moment, but the high alternating frequency prevents polarization of the double layer. The induced dipole moment of the particles leads to structure formation. Which structures form, depends on the particle volume fraction and the electric field strength. When an electric field is applied over a dilute colloidal suspension, the particles chain along the electric field lines. Upon increasing the field strength longer strings of particles form that arrange into body centered tetragonal structures at high fields. Also metastable sheets can form. This phase behavior has been established by theory and computer simulations [40–42] as well as by experiments [43, 44].

When the electric field is inhomogeneous an additional force is applied to the particles: a dielectrophoretic force. This makes the particles move along the gradient of the electric field strength. This can for example be used to manipulate the local particle volume fraction inside a sealed cell [45, 46]. Large colloidal crystals have been formed by slowly increasing the local volume fraction under the influence of a dielectrophoretic force [46, 47]. We will use this force to control the lateral position of strings of particles that form along the electric field lines. Inhomogeneities in the electric field strength were established by height modulations on one of the electrodes. The height modulations were colloidal particles arranged in a regular pattern (Figure 1.2). We made the pattern by positioning colloidal particles one by one on a substrate using optical tweezers.

Optical tweezers have been developed by Arthur Ashkin [48–50]. By using a tightly-focussed laser beam, micron-sized objects with a refractive index different from that of the surrounding medium can be trapped near the focus

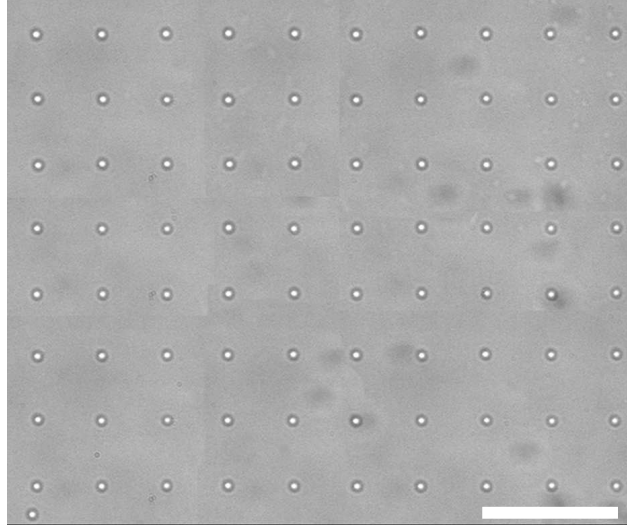


**Figure 1.2:** Pattern of colloidal particles made by placing micron-sized silica particles one by one on a substrate by means of optical tweezers. The scale bar is 20  $\mu\text{m}$ .

of the laser or be repelled from it. It is based on forces of radiation pressure. Light reflects when it hits an interface between two media with a different refractive index. The photons change direction and thus momentum. This momentum change results in a force on the particle. Traditionally, this force is decomposed into a scattering force and a gradient force [49]. The scattering force points along the propagation direction of the light. The gradient force is along the light intensity gradient. When the refractive index of the object is higher than that of the medium, this gradient force is towards the highest intensity, i.e. towards the focus of the beam. Due to the scattering force the stable position of the particle is just behind the focus. With this technique we positioned colloidal silica particles one by one on a substrate to make a patterned electrode.

#### 1.4 Permanent structures

For most applications, any prepared colloidal crystalline structure has to be made permanent. Amos *et al.* [14–16] fixed the structures within an epoxy resin. The particles of Ruhl *et al.* [18–20] were fixed in the matrix of their own soft shells. Jiang and McFarland [21] dispersed the particles in a medium that could be polymerized by illuminating it with UV light. We also used this medium. It is important not to destroy or distort the crystals while fixing them. Therefore, we used confocal microscopy with which we could determine particle positions before and after making the structures permanent.

If the matrix is elastomeric, the structure can be deformed after polyme-

rization. Several groups [51–54] already prepared elastomeric colloidal crystals that they reversibly deformed. By changing the lattice constants they changed the optical properties, e.g. a shift in the Bragg peak. Such materials can be used as optical sensors for probing displacements or pressures or for detecting chemicals. It also becomes possible to combine shear with another external field. For example, electric field induced structures can be deformed by which crystals with even different symmetries can be made.

## 1.5 Scope of this thesis

In this thesis we used both shear flow and an electric field to control colloidal crystallization. Chapter 2 deals with the description and the characterization of a new parallel plate shear cell that we developed. It has been designed such that it can be mounted on top of a confocal microscope which enables us to examine structures under shear. First, the performance of the shear cell without a colloidal dispersion between the plates was tested. Then, the flow profile of a dilute dispersion was measured.

Experiments performed with this shear cell are described in Chapter 3. The flow profile of a colloidal dispersion above its bulk crystallization volume fraction was measured. Next, crystallization and melting of this dispersion were examined under shear.

In Chapter 4 we describe the preparation of colloidal crystalline films by spin coating. From these films self-supporting freestanding colloidal crystalline films could be made. This is described in Chapter 5.

In Chapter 6 we used an electric field to arrange colloidal particles in a regular structure. By making a template on one of the electrodes not only the order along the field lines, but also the position of the strings of particles perpendicular to the electric field was controlled.



# 2

## A new parallel plate shear cell for *in situ* real-space measurements under shear flow

### Abstract

We developed and tested a parallel plate shear cell that can be mounted on top of a confocal microscope to perform real-space measurements on complex fluids under shear. To follow structural changes in time a plane of zero velocity is created by letting the plates move in opposite directions. The gap width is variable between 20 – 200  $\mu\text{m}$ . Such a small gap width enables us to examine the total sample thickness using high NA objective lenses. The achieved shear rates cover the range of  $0.02 - 10^3 \text{ s}^{-1}$ . This shear cell can apply an oscillatory shear with adjustable amplitude and frequency. The maximum travel of each plate equals 1 cm. For most complex fluids an oscillatory shear with such a large amplitude can be regarded as a continuous shear. We measured the flow profile of a suspension of silica colloids in this shear cell. It was linear except for a small deviation caused by sedimentation. To demonstrate the excellent performance of this new setup we examined shear induced crystallization and melting of concentrated suspensions of 1  $\mu\text{m}$  diameter silica colloids.



## 2.1 Introduction

Complex fluids already exhibit a rich phase behavior under undisturbed conditions. Applying an external field like a shear flow makes them even more interesting [55]. Shear flow can, for example, change the location of phase transitions, it can induce both crystallization and melting [9, 26, 56–59]. A system under shear can separate into phases with different viscosities leading to shear banding. Shear can also promote a specific orientation: polymers stretch in the flow direction [60] and colloidal particles tend to align in the flow direction [10, 61]. Liquid crystalline systems can undergo an isotropic to nematic transition under shear [62–64].

Originally, shear cells were mainly developed to measure bulk material properties like yield stress, elasticity and viscosity. They were built in different geometries, all with their own advantages and disadvantages. The parallel plate and the cone-plate geometry are the simplest ones in the sense that in these geometries both the shear rate and the shear strain are at a certain radial position uniform throughout the cell. With a parallel plate shear cell that has a short travel one can only apply an oscillatory shear [17]. When the travel is long enough the shear can be regarded as continuous. The cone-plate shear cell used by Derks *et al.* is suitable to apply a continuous shear, but the moving components of that shear cell are too heavy to apply an oscillatory shear with it. For determining the influence of the shear rate on a given system, the parallel rotating disk shear cell is a good choice. In this geometry both the shear rate and shear strain increase in radial direction. The Couette cell is widely used for continuous shear measurements. [65]

Material properties like elasticity are useful to know, but it is difficult to relate them to the materials microstructure and structural changes under shear. Therefore, shear cells have been designed that can examine samples under shear. At first, they were mostly combined with scattering techniques like SAXS [66–70], SANS [71, 72] and SALS [73–75]. More recently the combination of optical microscopy with shear cells has been made [30, 72, 76–79].

Another important step forward in the ability to locally investigate complex fluids quantitatively in 3D was the development of confocal scanning laser microscopy (CSLM) [31]. This technique enables one to reveal structures in 3D by examining samples slice by slice [32, 80–82]. When one wants to examine in such a slice the structural changes of a system under shear, one has to prevent that layer from moving out of the field of view. This can be done by creating a zero-velocity plane (zvp). This concept was first introduced by Taylor [35] and has been applied in several shear cells with different designs [36–38]. These cells cannot, however, be used in combination with confocal microscopy using high numerical aperture objectives.

Therefore, we developed a new parallel plate shear cell with a zvp [76]. We call it the High Precision Parallel Plate Oscillating Shear Cell, HIPPOS in

short. The shear cell can be mounted on top of an inverted confocal microscope; the sample cell is optically accessed through the bottom glass plate. To make optimal use of the resolution of the confocal microscope and to image individual colloidal particles high numerical aperture oil immersion objective lenses are used. These objectives have a working distance of  $100\ \mu\text{m}$ , assuming that imaging is done through a no. 1 microscopy glass slide of  $160\ \mu\text{m}$ . So, even when the bottom glass plate is as thin as  $160\ \mu\text{m}$ , only the lower  $100\ \mu\text{m}$  of a sample can be examined. Because complex flow profiles may occur in a complex fluid under shear, we want to be able to view the complete gap. The gap width should thus be small. We chose a gap width that is adjustable from  $20 - 200\ \mu\text{m}$ . With a gap width of the order of one hundred micrometer and micron-sized particles a variation in the position of the plates of even a few micrometers is significant. The cell was, however, made to be very stable and the motion of the plates was made accurately parallel. As we use small sample volumes a vapor barrier was included to limit evaporation. This shear cell can apply shear rates in the range of  $0.01 - 10^3\ \text{s}^{-1}$ , which is the useful range for most complex fluids. The amplitude of the oscillatory shear is variable and reaches up to  $1\ \text{cm}$ , which is large enough to regard it as a continuous shear for the systems that we study. Furthermore, a transparent window is made in the top plate to allow for light scattering experiments. Finally, we chose for a modular design. The glass plates that are in contact with the sample are attached to cassettes that are placed in translation stages moved by piezo motors. The glass plates are exchangeable, which simplifies cleaning and makes it possible to examine, for example, the influence of wetting properties or surface patterning of the plates. New cassettes can also be designed for specific experiments, e.g. to apply an electric field or to measure forces during shearing.

Limitations of our shear cell are that it is not temperature controlled. The cell must also remain horizontal making it difficult to perform SAXS or SANS measurements.

## 2.2 Shear cell construction

### 2.2.1 Layout of the shear cell

Samples are sheared between two microscopy glass slides that are attached to two cassettes. The bottom translation stage contains the removable bottom cassette with the bottom glass slide. The top translation stage has a similar cassette for holding the top glass slide. When the stages are in center position, first the bottom and then the top cassette can be inserted. The main frame supports both translation stages and their guiding rods. Attached to the sides are two independently mounted motors that separately drive the top and bottom stage via connecting rods. Both the translation stages and the

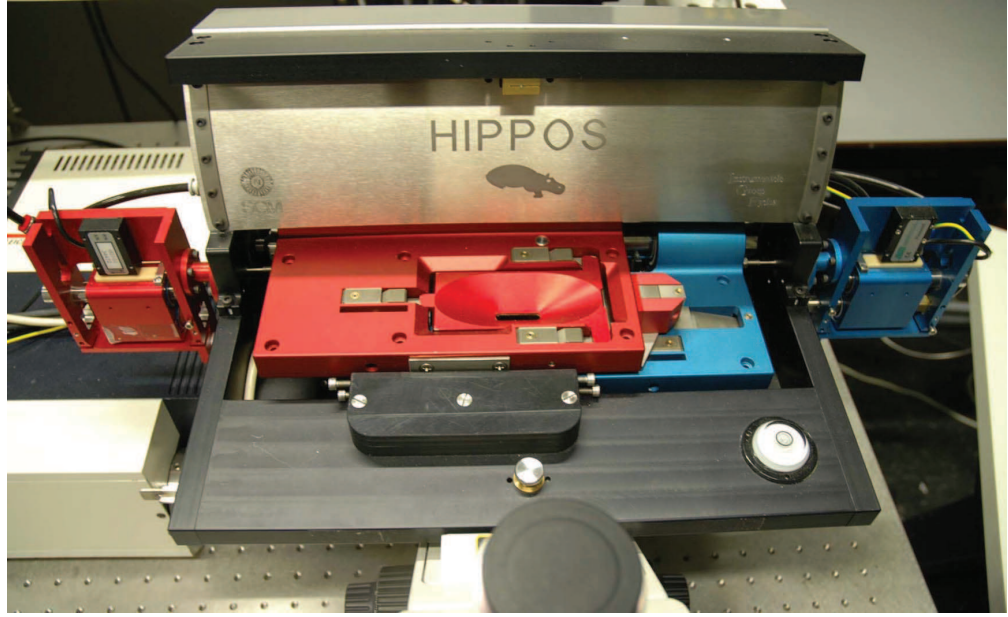


**Figure 2.1:** Photograph of the parallel plate shear cell placed on top of an inverted confocal microscope.

motor stages are borne by air bearings. Figure 2.1 shows the shear cell as placed on top of an inverted confocal microscope. Figure 2.2 is a schematic representation in which all components are indicated.

The glass plates need to be exactly parallel to the axis of motion and the gap width has to be adjustable. Each cassette is therefore supported by three bearing balls that can be adjusted individually or in combination for the tilt or the height of the glass plates.

With a cross adjustment lever the pair of stages can be shifted a few millimeters perpendicular to the translation axis. This is useful for finding a suitable area for imaging.

### 2.2.2 Design of a high precision shear cell

Creating a shear cell with a high precision and a steady zero-velocity plane requires a solid mechanical design of the stages and the cassettes, a proper alignment of the glass plates, a constant gap and a well-designed velocity control loop. At the high precision required no stick-slip or play can be tolerated, neither in the driving system nor in the linear guides. Any force or other effect that is not constant will cause a noticeable effect on the stages. All these effects have to be mapped in advance. By a consequent application of design rules for high precision equipment the effects cannot be eliminated but their effect in the imaging volume can be reduced as much as possible to achieve stable imaging of samples under shear.

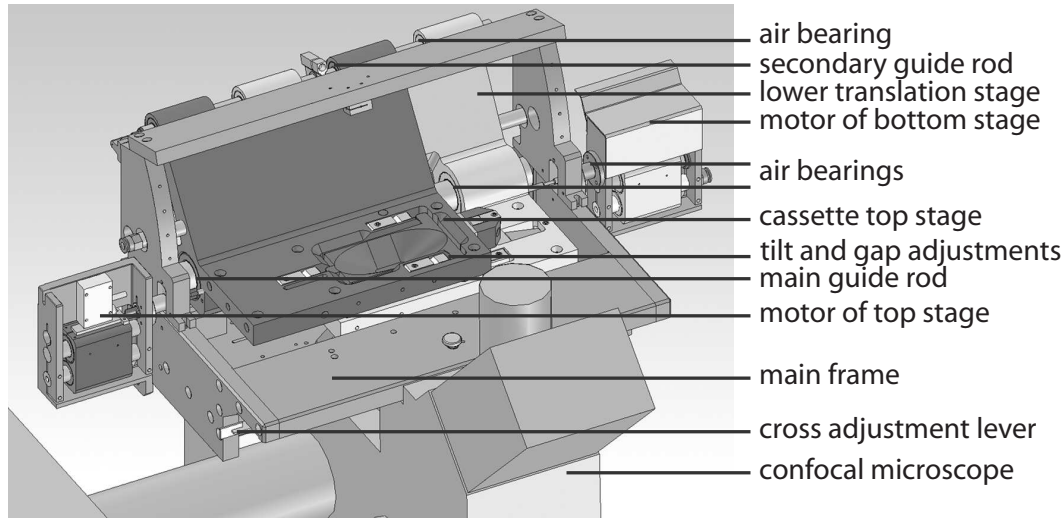


**Figure 2.2:** Schematic representation of the shear cell as placed on top of an inverted confocal scanning laser microscope.

### 2.2.3 Design of the stages

One of the requirements of the shear cell is that it has a steady zero-velocity plane. The microscope on which this cell is used, has a resolution of  $0.2 \mu\text{m}$  in the  $xy$ -plane, i.e. in the plane perpendicular to the optical axis of the microscope. To make optimal use of the resolution of the microscope the linearity of the shear cell and its controller has to be within  $0.05 \mu\text{m}$ .

To eliminate displacements of the shear cell relative to the microscope, which would lead to a disturbance of the images, we chose to place the shear cell on top of the microscope. Therefore, the shear cell has to be relatively lightweight and a compact construction with high stiffness is needed.

An inventory of all the disturbing forces that are exerted on the frame and the stages shows that the largest disturbance is caused by the “cg-shift”, i.e. by the moving of the center of gravity of each stage. A stage like this can be guided along a round main guide rod, but it needs a second parallel guidance to prevent a rotation around the main guide rod.

A frame that has the required parallelism of both guiding rods and that remains parallel under the forces exerted during the application of a shear stress would get too large and heavy to stand on a microscope. As a consequence the stiffness of the frame is limited. The maximum achievable stiffness in this lightweight setup makes it impossible to achieve nanometer precision along the whole stage. Warp and deflections occur, but by careful design the precision is at its maximum where it is needed: in the focus of the microscope.

This setup has been developed such that:

- Both stages are guided by the same set of parallel guide rods. This

ensures maximum parallel movement of the two stages.

- By giving the stages an angled design, the center of gravity of the stages is very close to the vertical plane containing the main guide rod. This reduces the bending forces on the secondary guide rod to nearly zero.
- By over-constraining the secondary guide rod it has become self-aligning with the main guide rod.
- The air bearings of the secondary guide rod are mounted in the plane normal to the backplane of the stages. Production tolerances on this mounting plane result in stresses within the plane and give minimal displacement errors.
- The main frame of the shear cell has a limited stiffness to keep the two guide rods parallel. The stages provide the required stiffness.
- The shear gap is at the same height as the center of the main guide rod to reduce Abbe errors.
- By giving the secondary guide rod a lower stiffness than the main guide rod extra stress reduction is obtained in the stages.
- The use of porous air bearings (New Way) evens out production inaccuracies of the guide rods over a relatively large area. The bearings are self-aligning.
- The centers of mass of the stages lie closely adjacent to the main guide rod so that the motor rods can be mounted there, causing minimal Abbe errors.
- The position measurement of both stages happens with an optical pickup unit. These units are placed directly under the center of mass of the stages and as close as possible to the focus of the microscope.
- Adjustments to the above rules have intentionally been made with some offset to avoid cycling of forces through zero. For example the centers of gravity of the stages lie slightly aside the axis of the main guide rod so that the secondary guide rod always remains slightly loaded in one direction.

All stages are supported on air bearings. Porous bushing bearings have been chosen for their compactness. Undesired over-constraintment has been avoided by constraining the secondary guide rod only in the single direction needed.

### 2.2.4 The motor stages

Piezo stepper motors (Nanomotion) were chosen for their wide dynamic range, infinite stroke and high precision. In addition to the driving force these motors exert a force normal to the axis of motion. To avoid deformation of the translation stages separate motor mounts have been designed. These mounts have two additional functions: 1) To supply air to the translation stage via a special passage through one of the air bearing so that undesired stresses caused by the bending of air hoses are avoided. A chamber in the modified bearing transmits the air from the hollow supply axis to the motor mount and translation stage. 2) Modular function separation: optimizations in the actuate and control loop can be done without having to modify the whole shear cell.

### 2.2.5 Cassette design

Both stages have a cassette to which microscopy glass slides are attached. The glass slides between which a sample is sheared need to be attached to the cassette with an extreme flatness on the sample side. For every experiment new slips are glued onto the cassettes. Between the glass and cassette a soft paper mask is applied soaked with an epoxy glue. The soft paper is a hygienic way of applying glue where it is needed and it functions as a bed of tiny springs for the flexible glass slides. During curing of the glue an optical flat is pressed on the glass slide, functioning as a flatness reference. An interference pattern appears and the shape of this pattern is an instantaneous check to see whether a high flatness is obtained.

To minimize evaporation a vapor barrier is made consisting of a rectangular metal ring hanging in a channel filled with water (see Figure 2.3). Inside the thus sealed sample cell there are two additional gullies to fill with the solvent of the sample. The solvent creates a vapor pressure that prevents the sample from drying out.

To test the parallelism of the two translation stages, a second set of cassettes has been designed. Instead of microscopy glass slides they each carry an optical flat. It is then possible to separate possible height deviations in contributions from 1) deviations in the movement of the stages and 2) unevenness of the glass slides.

### 2.2.6 Cassette alignment

To align the glasses with the axis of motion the cassettes have to be aligned one by one. Each cassette is supported by three bearing balls. In order to align a cassette the height of each ball has to be separately adjustable. To set the desired gap width the height of the three balls of the upper cassette has to be adjusted all by the same amount. A universal compact module has been developed that can combine an individual and a grouped adjustment



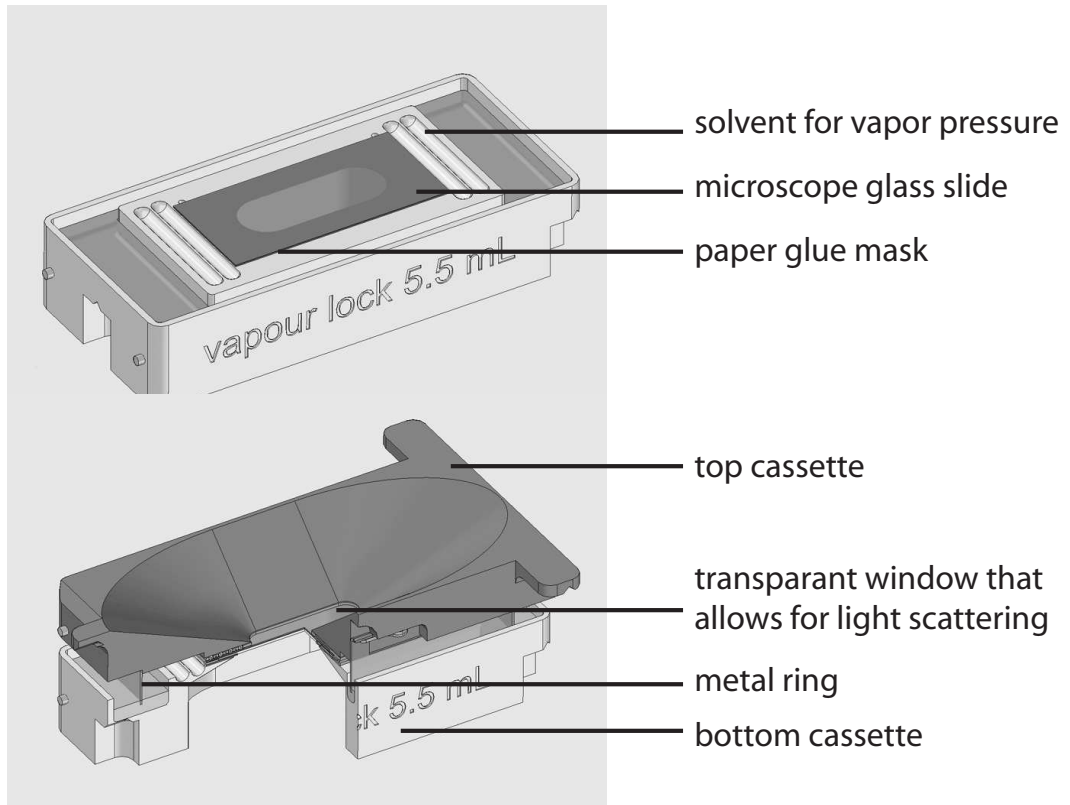


**Figure 2.3:** The bottom and top cassette. The bottom cassette has a gap to fill with water. The top cassette carries a metal ring that hangs in the water to seal the sample cell. A transparent window in the top cassette allows for light scattering measurements.

(Figure 2.4).

A lightweight and stiff construction to allow for a grouped adjustment is by coupling the three modules of one cassette by a horizontal plate. The three modules for one cassette have been mounted in this single plate to couple the movements. A rocker converts the horizontal plate movement to the vertical ball movement. The hinge of this rocker is mounted on a lever that applies the individual adjustment. By doing so, both movements are added up to one ball lift. Only little space is available for the mechanism. High stiffness and relatively large deflections are therefore needed in the leaf spring hinges. A normal leaf spring has limited stiffness normal to its plane. Cross leaf hinges cannot be made in one step by wire electrical discharge machining (wire-edm). The configuration as used here, referred to as “star leaf hinges”, gives relatively large deflections and a high stiffness within a simple to produce geometry. The mechanism is free of stick-slip and play. It is also rigid enough to withstand the acceleration and shear forces encountered in typical experiments.

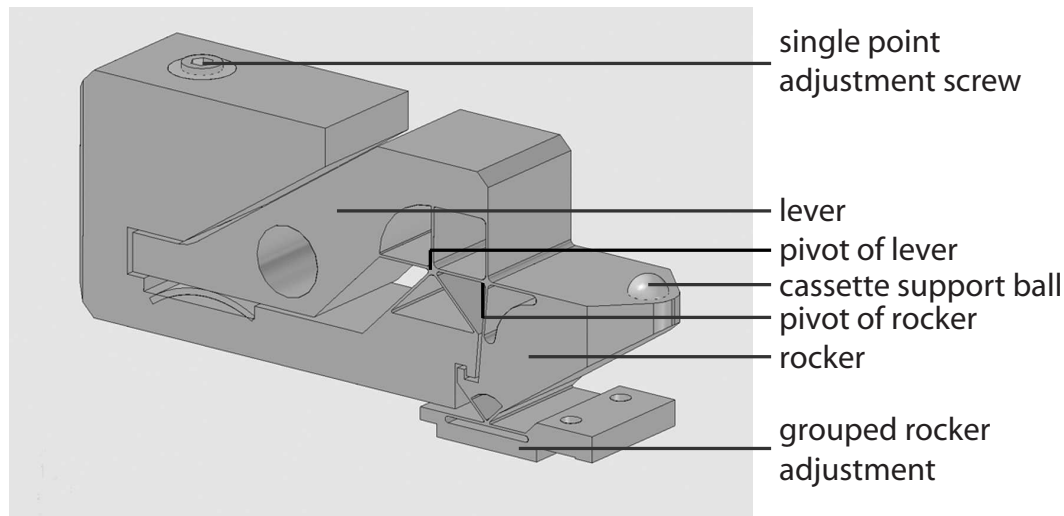


**Figure 2.4:** Mechanism to adjust the height of the balls that support the cassettes.

### 2.2.7 The control loop

The total travel of both stages is 10 mm. This is so large that capacitive position sensors cannot be used. To cover a for complex fluids relevant range of shear rates, the velocity of each stage has to range from  $2.5 \mu\text{m/s}$  to  $10 \text{ mm/s}$ , with a maximum deviation from the desired speed of 2%. Linear tachogenerators for this wide speed range are hard to find so two LIP372 linear position encoders (Heidenhain) are used to obtain a position signal with a sufficiently high signal frequency at the lowest speed to avoid dither. A Galil DMC2040 controller is used to control the Nanomotion HR2 piezo stepper motors. The controller is fast enough to handle the quadrature signal from the position encoders also at maximum speed.

The HR2 piezo steppers use two resonating ceramic fingers to step over a matching ceramic strip. A spring pushes the fingers against the strip. On one half of the electronic signal, the finger will push the stage in one direction. On the other half of the signal the finger moves back. Moving backwards the finger moves so fast that inertia of the stage and a limited friction make the finger break free from the strip. Depending on the shape of the signal, the stage is pushed in forward or backward direction. These motors have a very high positioning resolution. Yet, at speeds as low as a few  $\mu\text{m/s}$  most piezo stepper motors do not provide a smooth and constant speed behavior. The Nanomotion AB5 motor controller can add a subtle hammer function to the standard elliptical movement of the finger. This ensures that even at the smallest amplitude the stepper-finger can break free from the strip and that a step is made. The measure and control loop as created for this shear cell has proven to work well over the whole speed range.



A graphical user interface has been made in which the user can control the shear settings. The speed of the plates, the velocity ratio with which the top and bottom plate move and thus the height of the zero-velocity plane, amplitude, starting position along the velocity axis and motion functions such as saw-tooth or sinusoidal can be set. For alignment the stages can be moved by slider controls in the interface, whereas for an experiment a continuous oscillation function can be set.

### 2.3 Operation

The bottom glass plate is a standard microscopy no. 1 (thickness of 0.13 – 0.16 mm) glass slide of 24 mm  $\times$  50 mm. The top plate is a no. 5 (thickness of 0.5 – 0.6 mm) glass slide cut to 15 mm  $\times$  30 mm (Menzel). The slides have to be attached to the cassette in such a way that fluctuations in height and thus in the gap width are minimal. The glass slides and cassettes are first thoroughly cleaned with ethanol giving special attention to removing dust particles. Then, one sheet of double-sheeted tissue (Kleenex hand towels code 6762, cut to size) is drained in mixed two-component glue (Bison epoxy rapid) and placed on a cleaned glass slide. The glass slide and sticking tissue are together stuck on the accompanying cassette. The tissue is used to absorb height fluctuations that unremoved dust particles can otherwise induce. During the couple of hours needed for the glue to harden an optical flat is placed on top of the glass slide. This is done to obtain highly flat glass plates. The optical flat has a surface roughness of  $\lambda/20$  and this flatness is passed on to the glass slide.

Before filling the sample cell the plates are aligned one by one. The  $z$ -position is determined with the microscope in reflection mode, using the reflection of the 488 nm line of the Argon laser. Whereas we use oil immersion objectives during experiments, we use an air objective ( $63\times 0.7$  NA, Leica) for alignment to avoid immersion oil on the bottom side of the top plate, which is the inside of the sample cell. The relative  $z$ -position of the glass-air interface is calculated from an  $yz$ -image, i.e. in the vorticity-gradient plane. An example of such an image is given in Figure 2.5. The intensity of the reflection was summed over each horizontal line and the maximum was taken as the position of the interface. This does not necessarily coincide with the glass-air interface, but because only the difference between the interface at different lateral positions is of importance, this possible deviation can be disregarded. The accuracy of the position determination is about 100 nm. Each plate is then moved over its total travel of 1 cm and the  $z$ -position at the two ends is compared. If necessary the tilt is adjusted with the adjustment screws. After exchanging the objective for an oil immersion objective used for imaging in the experiments, the bottom cassette is loaded into the corresponding stage. The vapor barrier is then filled with 5.5 ml water and a few droplets of the solvent are dropped into the vapor gully to bring the liquid in equilibrium

**Table 2.1:** Achieved range of various parameters of HIPPOS.

gap width	20 – 200 $\mu\text{m}$
cell size	15 mm $\times$ 30 mm $\times$ gap width
cell volume	9 – 90 $\mu\text{l}$
speed per plate	2.5 $\mu\text{m/s}$ – 10 mm/s
shear rate	0.02 – $10^3 \text{s}^{-1}$
maximum travel of each plate	10 mm

with its vapor. This minimizes evaporation and thus a possible change in the concentration of the sample. Next, a few drops of the dispersion are put on the bottom plate. The volume of the dispersion has to be larger than the volume of the cell to avoid high capillary forces that could influence the flow behavior of the sample. Finally, the top cassette is slowly lowered on top of the dispersion and the desired gap width is set.

In the graphical user interface the amplitude of the oscillation ( $A$ ), the summed speed ( $v$ ) of the plates and the ratio of the speed of bottom ( $v_B$ ) and top plate ( $v_T$ ) are set. The gap width ( $d$ ) connects these parameters to the shear rate, maximum strain and height of the zero-velocity plane ( $z_{zvp}$ ) as described below. Table 2.1 summarizes the range of all settings.

The shear rate,  $\dot{\gamma}$ , is given by

$$\dot{\gamma} = \frac{v_T + v_B}{d}, \quad (2.1)$$

and the maximum strain,  $\gamma_{max}$ , by

$$\gamma_{max} = \frac{A_T + A_B}{d}. \quad (2.2)$$

The height of the zvp is determined by the ratio

$$r = \frac{v_B}{v_T} \quad (2.3)$$

as follows:

$$z_{zvp} = \frac{d}{\frac{1}{r} + 1}. \quad (2.4)$$

After the experiment the glass plates can be detached by heating them to approximately 100°C on a heating plate. The glue then becomes soft and the glass plates can easily be removed.

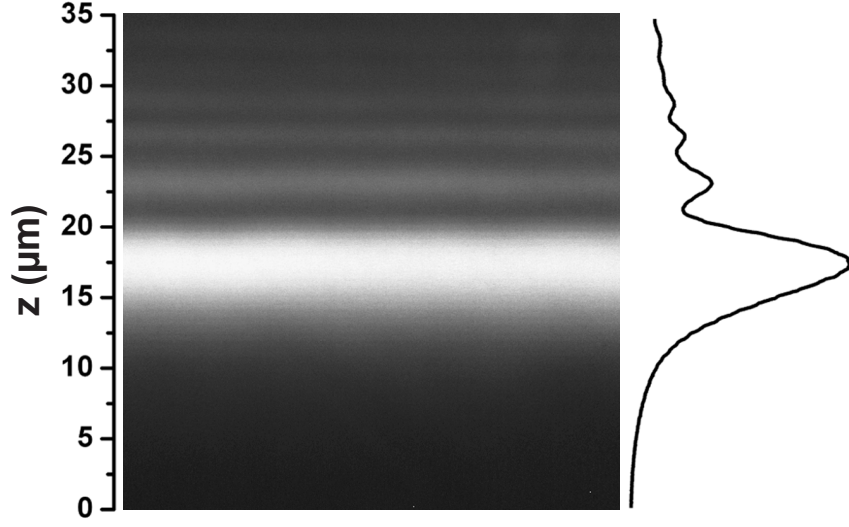


**Figure 2.5:** a) Example of the glass-air interface at the top side of the bottom plate imaged in reflection mode with a confocal microscope. From such an image the relative position of the interface is determined by summing the intensities horizontally and determining the maximum. The most intense peak is taken as the glass-air interface. This might not be the absolute position of the interface, but this deviation can be neglected since we only need the height relative to the height at a different spot of the glass plate. The less intense peaks are caused by interference.

## 2.4 Experimental

The shear cell was placed on top of an inverted Leica TCS-SP2 confocal scanning laser microscope. The 488 nm laser line of an Argon laser was used for imaging. Scanning along the  $z$ -axis was done using a piezo focusing drive (Physik Instrumente). This direction coincides with the gradient direction of the shear flow field. The velocity direction is along the  $x$ -axis (see Figure 2.6). All measurements were done in a room that was temperature controlled at  $21 \pm 1^\circ\text{C}$ .

### 2.4.1 Determination of the alignment and motion of the plates

To create a steady flow profile the plates have to be parallel to each other in the velocity direction. A roll around the  $x$ -(velocity) direction does not influence the flow profile. It does influence the local shear rate though. To show that the plates are highly parallel the  $z$ -position of each plate was measured every 0.5 mm of the total lateral travel of 1 cm. With a  $63\times 0.7$  NA Leica air objective the reflection of the 488 nm laser line was measured and the position of maximum intensity was taken as the glass-air interface.

Possible fluctuations in height may have two origins: 1) fluctuations in the

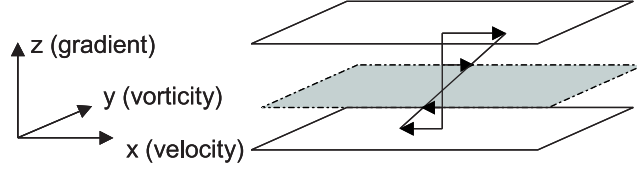


**Figure 2.6:** Illustration defining our coordinate system. The optical axis of the microscope is along the vertical  $z$ -axis. The zero-velocity plane (grey) is perpendicular to this axis and lies in the  $xy$ -plane. Its vertical position can be set at any height. The velocity direction is along the  $x$ -axis of the microscope. The vorticity direction is along the  $y$ -axis and the gradient direction along the  $z$ -axis.

$z$ -position of the stages and 2) a lack of flatness of the glass plates themselves. To distinguish between the two the alignment measurements were performed both with a cassette containing an optical flat and with a (measurement) cassette with a no. 1 or a no. 5 microscopy glass slide attached to it.

To show that the plates keep their parallelism when the cell is filled with a fluid, we measured the  $z$ -position of the plates again after filling the shear cell. The fluids used were three silicone oils of different viscosities: 10 mPa·s, 50 mPa·s and 1000 mPa·s. All were obtained from Sigma Aldrich and used as received. A 63 $\times$  Leica oil immersion objective with 1.4 NA was used for imaging.

Another condition needed to obtain a steady and uniform shear flow is an accurate movement of the plates in the velocity-vorticity plane. To monitor this movement 1.2  $\mu\text{m}$  diameter silica particles were adsorbed on the glass plates. While the plates were moving  $xy$ -images were taken with fixed time intervals. The 2D cross-correlation functions of consecutive images were then calculated. The maximum of this function corresponds to the displacement of the plate. The accuracy of the displacement thus obtained is better than 0.1  $\mu\text{m}$ . The cell was empty during this measurement.

### 2.4.2 Characterization of the flow profile

Flow profiles were measured using a dispersion of 1.2  $\mu\text{m}$  diameter silica particles ( $\phi = 0.22$ ) in ethoxylated trimethylolpropane triacrylate (ETPTA, Aldrich, MW. 428, viscosity  $\approx 0.07$  Pa·s, used as received). The particles were synthesized via a Stöber growth [83]. A 0.4  $\mu\text{m}$  diameter core of the particles was labeled with fluorescein isothiocyanate (FITC), using the method of Van Blaaderen and Vrij [84].

There are different methods to determine the flow profile. Probably the most direct way is to take  $xz$ -images with fixed time-intervals. From the displacement of each particle the average velocity at each height can be determined. A disadvantage of this method is that it can only be used when the

velocity of the particles is low compared to the scan rate, because each particle has to be followed in time. A second method is to image particles in the  $xy$ -plane. By cross-correlating consecutive images the average displacement of the particles and thus the average velocity of that plane can be determined. Besides it only being applicable for low speeds, it has the disadvantage of being time-consuming because it has to be done at several heights to obtain the complete flow profile.

Therefore, we used the quicker and easier method that Derks *et al.* [34] introduced to determine flow profiles. They took images at a slow scan rate in the velocity-gradient ( $xz$ )-plane. Images are built up by scanning horizontal lines, i.e. along the  $x$ -(velocity) direction. During a scan the particles move. When a following line is scanned the particles are displaced, which leads to an image in which the particles appear deformed. The degree of deformation depends on the local velocity of the dispersion. For a linear flow profile the deformation becomes parabolic:

$$x(z) = \frac{\dot{\gamma}z}{\alpha} \left( \frac{1}{2}z - z_{zvp} \right) \quad (2.5)$$

where  $\alpha$  is the scan rate in  $\mu\text{m/s}$  and  $\dot{\gamma}$  is the shear rate.

### 2.4.3 Observation of shear induced crystallization and melting of colloidal dispersions

To illustrate the performance of this shear cell, we describe an experiment showing shear induced crystallization and melting of a colloidal suspension. The suspension consisted of fluorescently labeled  $1.2 \mu\text{m}$  diameter silica particles in ethoxylated trimethylolpropane triacrylate. The volume fraction was above the bulk crystallization volume fraction, which was around  $\phi = 0.50$  for this system. To induce crystallization a shear rate of  $0.45 \text{ s}^{-1}$  was applied. To melt the crystal afterwards a shear rate of  $2 \text{ s}^{-1}$  was applied. The zero-velocity plane was set at  $1/6^{\text{th}}$  of the gap; with the used gap of  $45 \mu\text{m}$  this is at  $7.5 \mu\text{m}$  from the bottom upwards.

## 2.5 Results and discussion

### 2.5.1 Determination of the alignment and motion of the plates

We performed a series of stringent tests to check the performance of the shear cell. First, the parallelism of only the stages was measured by monitoring the movement of the cassettes containing an optical flat. Figure 2.7 shows that the bottom and top stage can be aligned such that over their total travel of  $1 \text{ cm}$  they only vary  $1 \mu\text{m}$  (0.01%) and  $1.5 \mu\text{m}$  (0.02%) in  $z$  respectively.

Next, the optical flat was replaced by the glass slides that are used in a normal experiment. Fluctuations in the glass plates can be caused by stress

built up when they are fixed to the cassettes, or by variations in their thickness. Figure 2.8 shows, however, that these contributions are small and that the total variation in  $z$  stays within  $1.5 \mu\text{m}$ . For our experiments these small deviations are acceptable. Note that there was hardly any difference in the flatness of the bottom and the top plate although the bottom plate is approximately four times as thin as the top one.

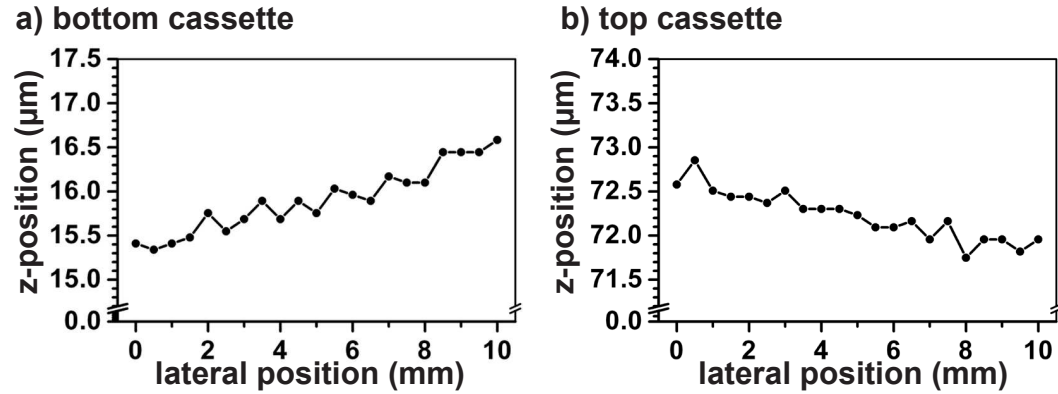


**Figure 2.7:** Vertical position of an optical flat a) inside the bottom and b) inside the top cassette when traversing laterally over a distance of 1 cm. The change in  $z$  is only a few micrometers.

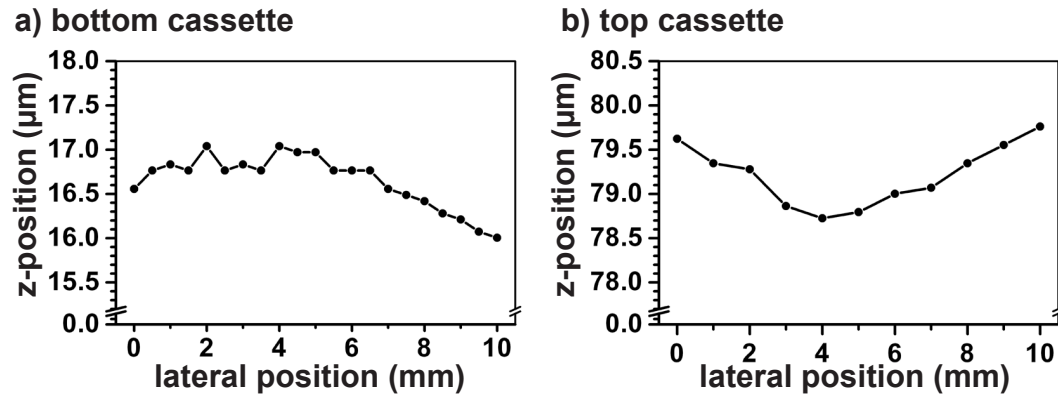


**Figure 2.8:** Vertical position of a no. 1 and a no. 5 glass slide a) on the bottom and b) on the top cassette when traversing laterally over a distance of 1 cm. Fluctuations in  $z$  were only of the order of a micrometer.

The plates must move in parallel also with a fluid in between over a wide and relevant range of fluid viscosities. To test this, silicone oils with viscosities of 10 mPa·s, 50 mPa·s and 1000 mPa·s were chosen. Both plates traversed back and forth with an amplitude of  $A_T = A_B = 3 \text{ mm}$  at a speed of  $v_T = v_B$

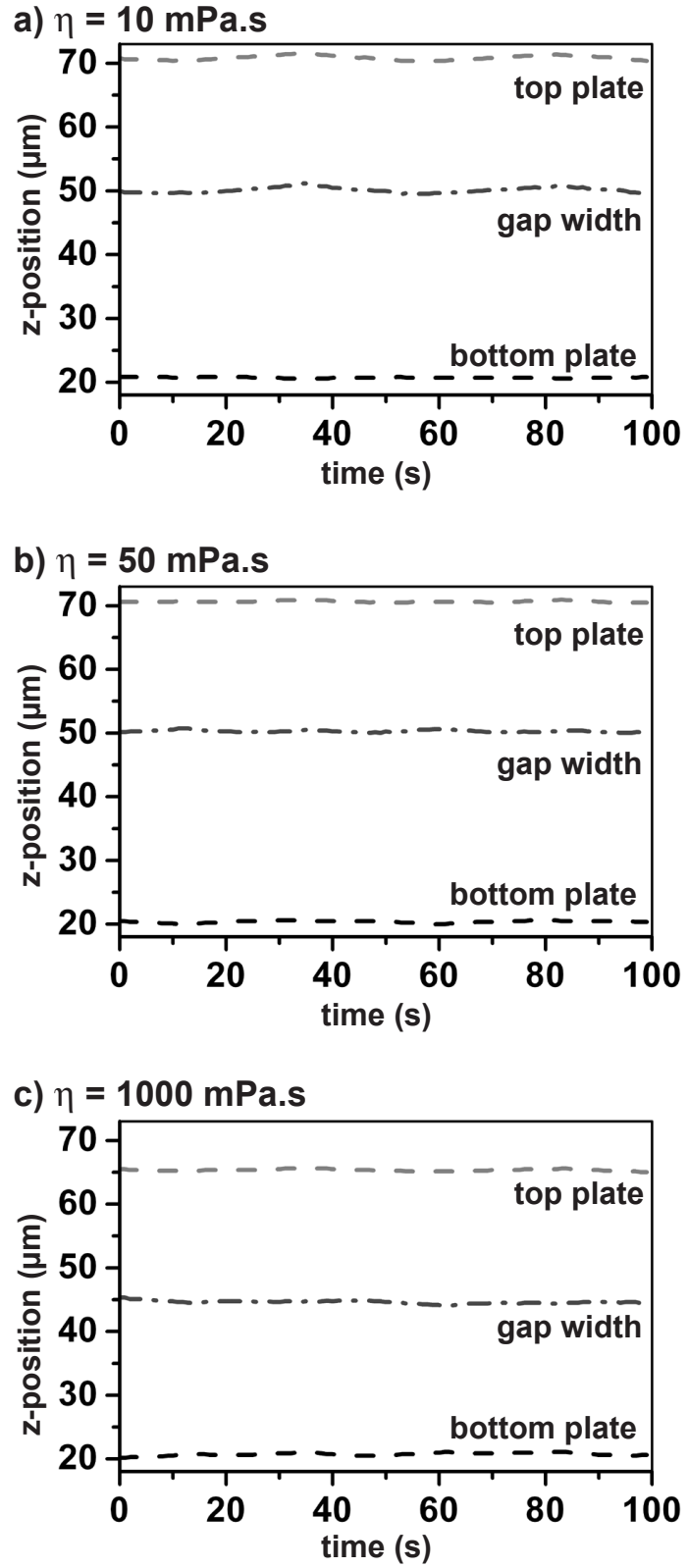


**Figure 2.9:** Stability of the plates in  $z$  when the cell was filled with silicone oils with viscosities of a) 10 mPa.s, b) 50 mPa.s or c) 1000 mPa.s. The change in  $z$  is only of the order of a micrometer while the lateral displacement of the plates is 6 mm.

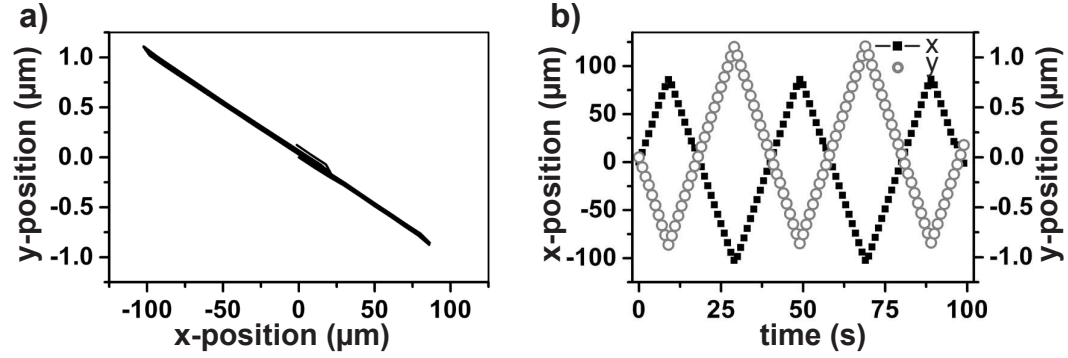


**Figure 2.10:** The relative position of the top plate in the velocity-vorticity plane during an oscillatory movement ( $v_{top} = 10 \mu\text{m/s}$ ,  $A_{top} = 100 \mu\text{m}$ ). The axis of motion was found to be rotated  $0.6^\circ$  with respect to the  $x$ -axis of the microscope. The plate made no noticeable irregular movements in the vorticity direction.

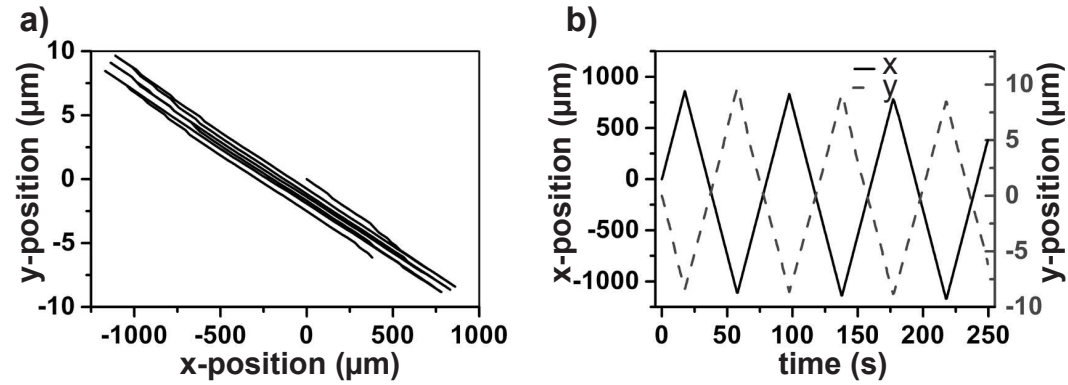


**Figure 2.11:** The relative position of the top plate in the velocity-vorticity plane during an oscillatory movement ( $v_{top} = 50 \mu\text{m/s}$ ,  $A_{top} = 1 \text{ mm}$ ). At a relative high speed and a large amplitude undesired movements in the vorticity direction were noted, but the effective error remained small.



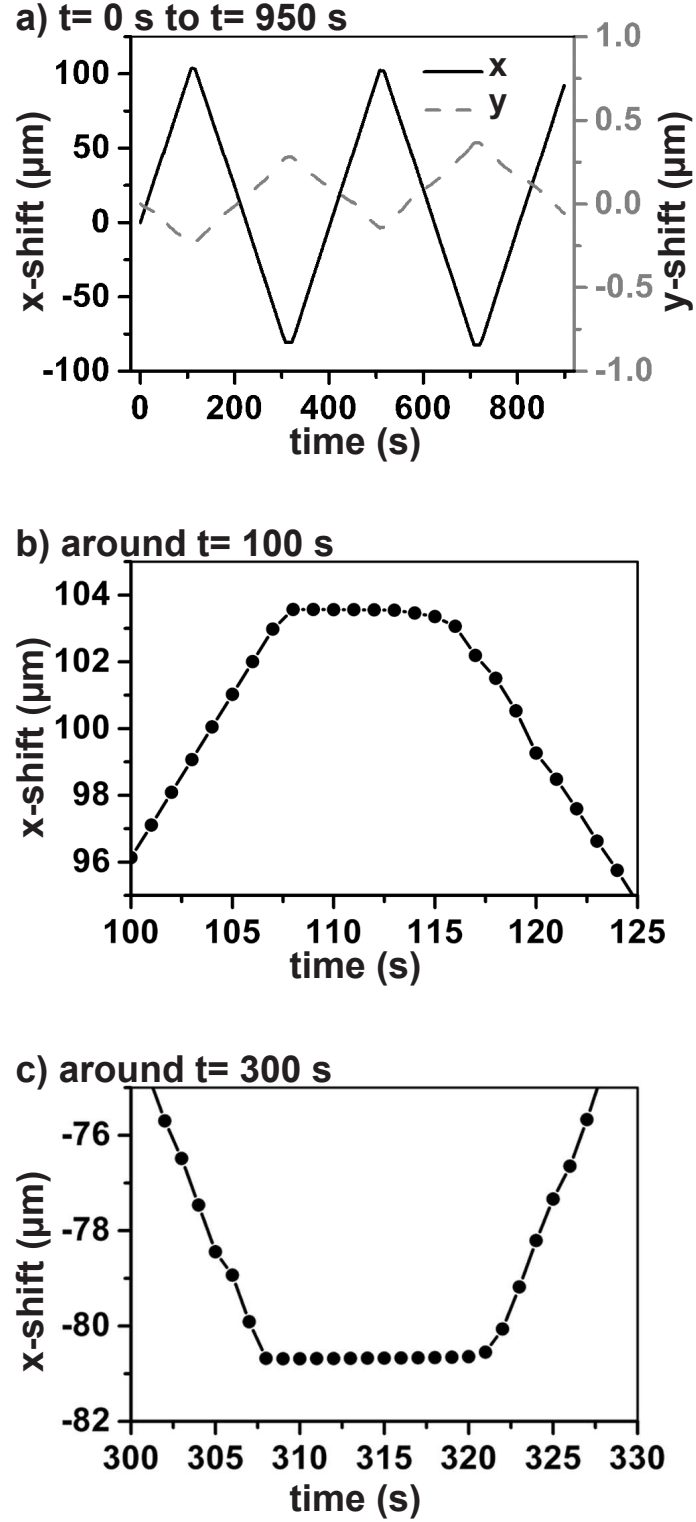


**Figure 2.12:** The relative position of the top plate in the velocity-vorticity plane during an oscillatory movement ( $v_{top} = 1 \mu\text{m/s}$ ,  $A_{top} = 100 \mu\text{m}$ ). Panel (b) and (c) are close-ups of the turning points. At speeds as low as  $1 \mu\text{m/s}$ , which is lower than the minimum speed for which the shear cell was designed, the top plate did not reverse instantly at the turning points. The period that the stage paused at the turning points was sometimes as long 12 s.

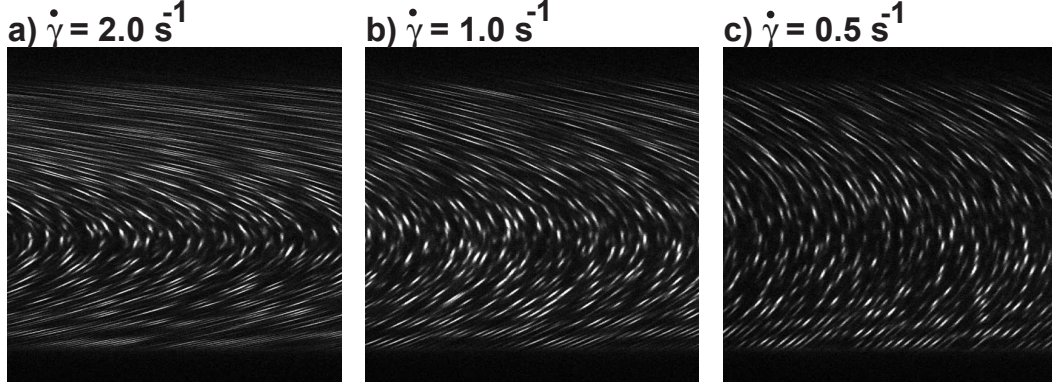


**Figure 2.13:** Slowly scanned confocal microscopy images of the velocity-gradient plane of a colloidal dispersion sheared at shear rates of:  $2.0 \text{ s}^{-1}$ ,  $1.0 \text{ s}^{-1}$  and  $0.5 \text{ s}^{-1}$ . The applied ratio  $v_{\text{bottom}}/v_{\text{top}}$  was 0.5. The gap width was approximately  $45 \text{ }\mu\text{m}$ . The scan rate was  $\alpha = 5.8 \text{ }\mu\text{m/s}$ .

$= 250 \text{ }\mu\text{m/s}$ . The gap was about  $50 \text{ }\mu\text{m}$ . Figure 2.9 shows that the plates hardly fluctuated in  $z$ . They moved over  $1\text{--}2 \text{ }\mu\text{m}$  in  $z$  which equals to only  $0.02 - 0.03\%$  of the travel. It corresponds to  $2 - 4\%$  of the gap width, though. The largest  $z$ -fluctuations were measured when the plates changed direction. Problems arise when the sample volume is smaller than or equal to the volume of the cell so that a liquid meniscus forms. Then, capillary forces become so large that the two plates are pulled towards each other until a stationary gap width is reached. When the top plate is then lifted, the bottom plate raises over the same distance. The sample fluid should therefore always overfill the cell.

Next, the movement in the velocity-vorticity plane must be well-defined: 1) there should be no drift in the velocity-direction meaning that after one oscillation the plates should return to their starting position, 2) the speed of the plates should be the same as or at least be proportional to the set speed and 3) there should be no movement in the vorticity-direction. To measure the movement silica particles were adsorbed on the glass plates and their position was followed during an oscillatory motion of the plates. The cell was empty during this experiment.

Figure 2.10 shows the position of the top plate during an oscillatory movement. The plate was set to move with a speed of  $v_T = 10 \text{ }\mu\text{m/s}$  with an amplitude of  $A_T = 100 \text{ }\mu\text{m}$ . The actual speed was determined by measuring the time needed to travel from a position just after one turning point to a position just before the next turning point. The actual speed was  $3\%$  lower than the set speed. After each oscillation the plate returned to very nearly its original position. Deviations were only minor and of the order of, or smaller than the resolution of the microscope, which is  $0.2 \text{ }\mu\text{m}$  in the  $xy$ -plane. It appeared

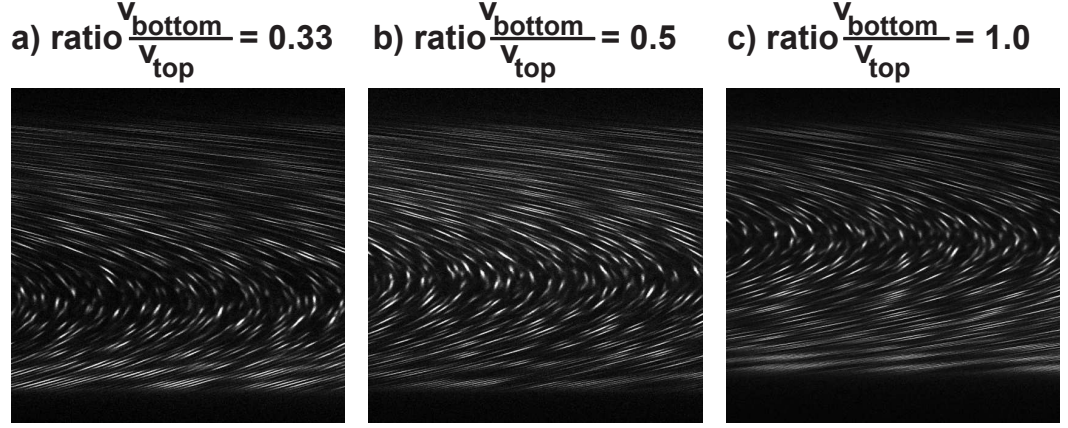


**Figure 2.14:** Slowly scanned confocal microscopy images of the velocity-gradient plane of a colloidal dispersion sheared at a shear rate of  $2 \text{ s}^{-1}$ , but with different velocity ratios. From left to right  $v_{\text{bottom}}/v_{\text{top}} = 0.33, 0.5, 1.0$ . The gap width was approximately  $45 \text{ }\mu\text{m}$ . The scan rate was  $\alpha = 5.8 \text{ }\mu\text{m/s}$ .

that the axis of motion of the top plate and the  $x$ -axis of the microscope make an angle of  $0.6^\circ$ .

At higher speeds and larger amplitudes the top plate still moved with only minor errors as Figure 2.11 shows for a set speed of  $v_T = 100 \text{ }\mu\text{m/s}$  and an amplitude of  $A_T = 1 \text{ mm}$ . Although the plate no longer returned to its exact starting position after one oscillation the error remained small. The actual speed was 2% lower than the set speed. Even at a speed of  $v_T = 1 \text{ }\mu\text{m/s}$ , which is lower than the minimum speed for which the shear cell was designed, the difference between the set and actual speed was only 3% with the actual speed being lower than the set speed. However, at  $v_T = 1 \text{ }\mu\text{m/s}$  the movement showed a delay at the turning points (Figure 2.12). Instead of immediately changing direction at the maximum displacement the stage stopped moving and started to move again after a certain time lag. Magnifications of the turning points (Figure 2.12b and c) show that this time lag can be as long as 12 s. Such a lag might also occur at high speeds, but if so, the delay occurring at a speed of  $100 \text{ }\mu\text{m/s}$  is smaller than the speed of our position detection which was 0.5 s.

The motion of the bottom plate showed a performance similar to that of the top plate. Again the actual speed was slightly lower than the set speed: 3% at  $v_B = 1 \text{ }\mu\text{m/s}$ , 3% at  $v_B = 10 \text{ }\mu\text{m/s}$  and 1% at  $v_B = 100 \text{ }\mu\text{m/s}$ . At  $v_B = 1 \text{ }\mu\text{m/s}$ , which lies outside the speed range for which this shear cell was designed, a time lag was again observed. The axis of motion of the bottom plate makes an angle of  $0.7^\circ$  with the  $x$ -axis of the microscope. Thus, the axis of motion of the top and bottom plate are practically parallel, as they should.

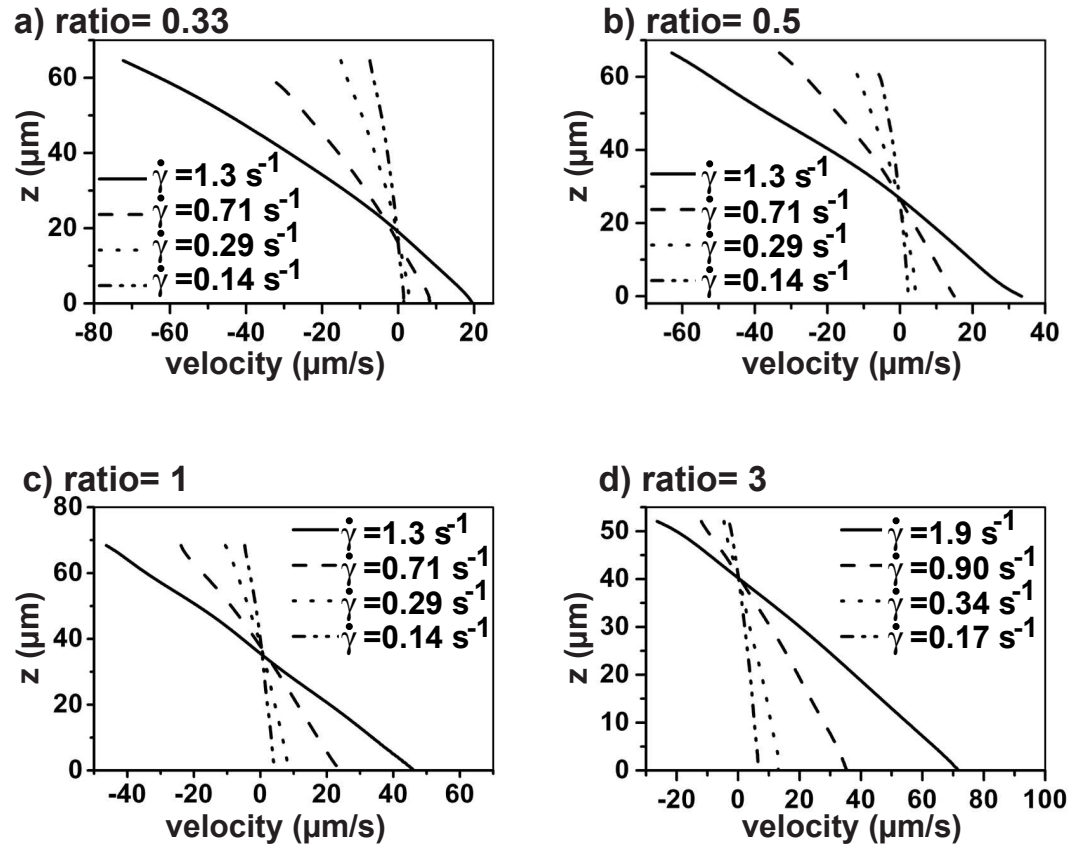


**Figure 2.15:** Measured velocity versus height. The different curves represent different shear rates. The curves cross at the position of the zero-velocity plane.

### 2.5.2 Characterization of the flow profile

The sample for determining the flow profile was a dispersion of  $1.2 \mu\text{m}$  diameter silica particles in ethoxylated trimethylolpropane triacrylate  $\phi = 0.22$ . Images were taken in the velocity-gradient plane. Figure 2.13 shows the velocity-gradient plane of the dispersion sheared at different shear rates. During scanning of the image the particles moved and therefore they appear deformed in the image. The degree of deformation depended on the local velocity. The zero-velocity plane is easily recognized at the top of the parabolas. From this deformation the velocity at each height is determined using the method of Derks *et al.* [34]. Because the ratio of the speeds of the bottom and top plate was fixed, the position of the zero-velocity plane did not change. The apparent deformation of the particles is larger at higher shear rates. Figure 2.14 shows the velocity-gradient plane of the colloidal dispersion sheared at a fixed shear rate of  $1.5 \text{ s}^{-1}$  but with different ratios:  $v_B/v_T = 0.33, 0.5$  and  $1.0$ .

Figure 2.15c shows the flow profiles for the case that the bottom and top plate moved with a ratio of 1. The flow profile was nicely linear, as expected.

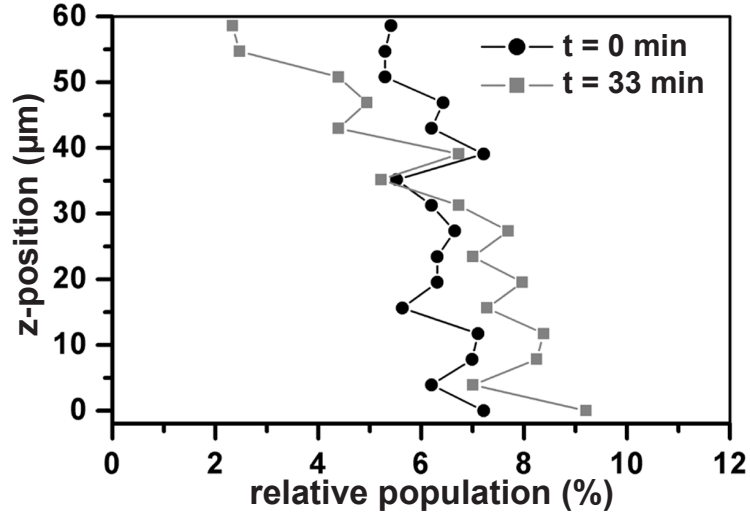


**Figure 2.16:** In time, sedimentation of the particles caused the particle density near the bottom to increase.

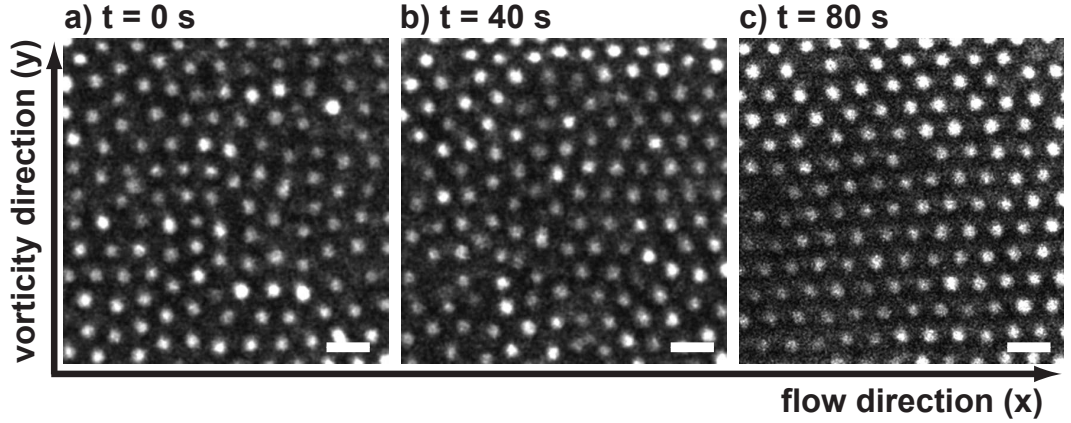


**Figure 2.17:** Confocal micrographs of a dispersion of  $1.2 \mu\text{m}$  diameter silica particles dispersed in ETPTA at  $\phi \approx 0.50$  during the application of a shear with  $\dot{\gamma} = 0.45 \text{ s}^{-1}$ . Initially the particles were not ordered, but they gradually crystallized in time. The scale bars are  $2 \mu\text{m}$ .

The profiles measured when the plates moved with a ratio of 0.33, 0.5 or 3 (see Figure 2.15a, 2.15b and 2.15d) were, however, slightly concave. Apparently the shear rate at the bottom was slightly lower than at the top part of the sample. The zero-velocity plane was also located slightly lower than calculated from the set ratio (Equation 2.4). Determining the particle density as a function of height, we concluded that this deviation from linearity is due to sedimentation. Over time the particles sediment (Figure 2.16) leading to a locally higher viscosity which leads to a local decrease of the shear rate.



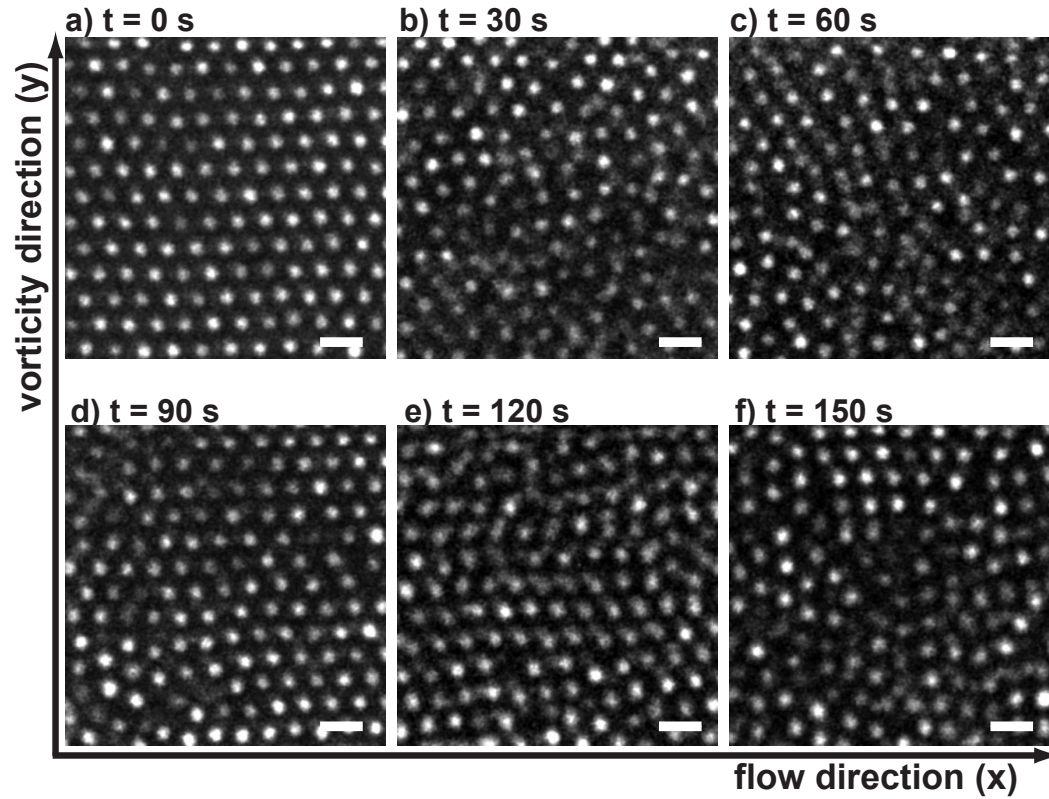


**Figure 2.18:** Confocal micrographs of an initially crystalline dispersion of  $1.2 \mu\text{m}$  diameter silica particles dispersed in ETPTA. At a shear rate of  $\dot{\gamma} = 2 \text{ s}^{-1}$  the average order of a dispersion decreased, but locally the order increased temporarily. The scale bars are  $2 \mu\text{m}$ .

### 2.5.3 Observation of shear induced crystallization and melting of colloidal dispersions

Before applying a shear flow the particles were randomly distributed. After application of a shear with shear rate  $\dot{\gamma} = 0.45 \text{ s}^{-1}$  the particles were seen to order and a close-packed line oriented parallel to the flow direction. Figure 2.17 shows the evolution of the order in the zero-velocity plane. The sample was found to have crystallized throughout the cell with rows of particles aligned parallel with the velocity direction.

When a high shear rate was applied ( $\dot{\gamma} = 2 \text{ s}^{-1}$ ) the sample slowly melted. Although the average order decreased continuously, the local order sometimes increased temporarily as Figure 2.18 shows. In these experiments the zero-velocity plane makes it possible to track individual particles for as long as they reside in the zero-velocity plane. A detailed analysis of the experiments will be presented in Chapter 3.

## 2.6 Conclusion

We have demonstrated a new parallel plate shear cell that enables microscopic observations of complex fluids using high NA objectives. The plates move in opposite direction creating a plane of zero-velocity. It is possible to apply shear rates up to  $10^2 \text{ s}^{-1}$ . The plates only fluctuate 0.01% in height over a travel of 1 cm which is more than sufficient for creating a stable zero-velocity plane (zvp) for imaging under shear flow. Even the bottom no. 1 glass plate was found to be stiff enough not to add any extra fluctuations in  $z$ -position. Also when the cell was filled with silicone oil the plates deviated less than 0.02% in  $z$ . The axis of motion was slightly rotated with respect to  $x$ -axis of the microscope, but apart from that there was no significant movement along the  $y$ -axis. Flow profiles measured with dispersions of silica particles dispersed in a viscous medium were almost linear. A small deviation that is probably caused by sedimentation of the particles was noticeable.

An experiment of shear induced crystallization and shear induced melting observed in the zvp illustrates the performance of the shear cell. The particles ordered continuously and collectively. Melting was, however, more of a localized process. The average order decreased continuously, but locally the order could also temporarily increase.

## Acknowledgements

We would like to thank everyone of the Instrumentele Groep Fysica (IGF, Utrecht University), who was involved in the design and construction of the parallel plate oscillating shear cell, and especially Joost Brand for his effort in designing and optimizing the shear cell. The section about the shear cell construction was based on reports written by Joost Brand. We also like to thank Hans Wisman who made the electronics of the shear cell and Didi Derks, for useful discussions about the measurements.

# Colloidal suspensions above their bulk crystallization volume fraction under shear

## Abstract

We examined colloidal suspensions above their bulk crystallization volume fraction under shear. A steady shear flow was applied by a parallel plate shear cell. By moving the two plates of the shear cell in opposite direction a zero-velocity plane was created in which we could follow particles over a long period of time. The gap width of the shear cell was smaller than  $100\text{ }\mu\text{m}$  so that it was possible to image particles in the complete gap. From images of the velocity-gradient plane it was deduced that the flow profile was not linear. Both close to the top and bottom plate the particles arranged themselves in hexagonal layers that slid over each other. This decreased the local viscosity, which was 1.5 times smaller in the sliding-layer structure than in a liquid-like region of the dispersion. When a low shear rate was applied to a crystalline suspension its hexagonal planes that were parallel to the velocity-vorticity plane showed a collective zigzag motion. The planes follow a zigzag path because the layers move inside “valleys” formed by particles of the underlying layer. The period of this motion was measured to be  $1.17/\dot{\gamma}$ . This is, indeed, very close to the value of  $\frac{3}{\sqrt{6}}/\dot{\gamma}$  expected for a zigzag motion of layers that move inside the “valleys” of the underlying layer. When the shear rate exceeded  $\dot{\gamma} = 2\text{ s}^{-1}$  the crystal melted. A shear rate below this threshold induced crystallization of an initially disordered suspension. Whereas during shear induced crystallization all particles ordered collectively, shear melting was a local process. Overall the order decreased, but locally the order fluctuated and sometimes temporarily increased in time. This scenario of melting and crystallization induced by shear is roughly opposite to that without shear.



### 3.1 Introduction

The majority of complex fluids are non-Newtonian liquids. When they are subjected to a shear flow they can exhibit shear thinning or shear thickening behavior. It has long been established that the macroscopic properties of a material are coupled to its microstructure. To understand the macroscopic behavior of flowing complex fluids much research is therefore done on revealing the microstructure under shear.

Apart from shear thinning and shear thickening, shear banding, which is characterized by a discontinuous jump in the flow profile, is also observed for many complex fluids [85]. For worm-like micellar systems this has been extensively studied [86–89], but it is only rarely studied in colloidal suspensions [63, 90]. Shear-banding has also been observed in suspensions of rod-like colloids [91]. Zukoski and co-workers [25, 92, 93] found with rheology and SANS that colloidal crystals shear thin discontinuously and that this is associated with a transition from a polycrystalline structure to a sliding layer structure. For not too soft potentials these sliding layers have a hexagonal symmetry [94, 95]. Imhof *et al.* [90] have shown that this transition also leads to a shear banded flow.

When taking a closer look at the motion of these hexagonal layers under shear it appears that they do not move in a straight line along the velocity direction. Scattering experiments suggested that the hexagonal layers remain registered necessitating a zigzag motion instead [94, 95]. Figure 3.1 illustrates the zigzag path. In equilibrium the position of a hexagonal layer is such that the particles in that layer fall in one of the two possible sets (black and open circles) of interstices formed by the particles in the underlying layer (grey circles). The zigzag motion is from one set of interstices to the next. This trajectory is the path of minimum energy [59, 96].

Shear has a dual role on the order. At high shear rates it can melt a colloidal crystal [24, 97], but at low shear rates it can induce order [9]. Shear changes the growth kinetics, i.e. the induction time, density of nuclei and crystal growth rate [27]. This has been studied both with experiments [26, 98] and simulations [99–101]. The main difference reported with crystallization without flow is that the crystals align in one direction. Crystals with a different orientation are destroyed after which they recrystallize in the preferred direction. Furthermore, shear influences the chemical potential difference between the liquid and the solid states. The nucleation and growth rate depend on the chemical potential difference. Because that is altered by the shear, the nucleation and growth rate are different from those in a steady state situation [99].

Most of the studies of complex fluids under shear have been done with light scattering [9, 26, 56], X-ray scattering [102] or neutron scattering [103]. Scattering techniques have the disadvantage that the data are averages over the sampled volume, information about local processes cannot be obtained.

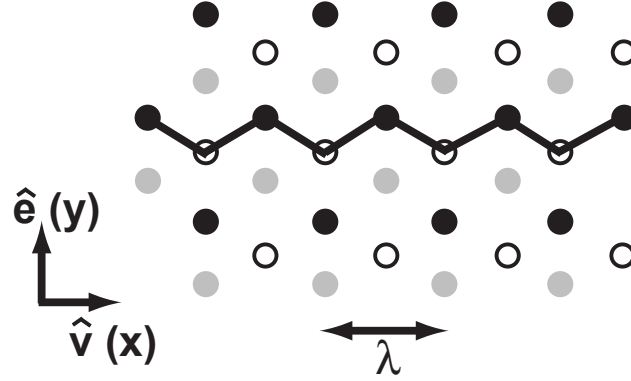


**Figure 3.1:** Illustration of the zigzag motion performed by hexagonal layers under shear. The zigzag path is through the “valleys” formed by the particles of the underlying layer (grey circles). First, the particles are at one position of interstices (black circles) formed by the underlying layer. Then, they move to the other set of interstices (open circles).  $\lambda$  is the in-plane nearest-neighbor distance.

Fuller and co-workers [28, 29] examined colloidal crystals under shear in real-space. Their systems were, however, only two-dimensional. Derks *et al.* [34] examine colloidal suspensions under shear in 3D using confocal microscopy. This technique enables one to determine structures on a single-particle level. Their shear cell was a cone-plate shear cell. Their set-up had the disadvantage that they were not able to observe particles in the complete gap. Here, we also used confocal microscopy, but we used a parallel plate shear cell with such a small gap width that we were able to observe particles in the complete gap. This enabled us to obtain local information about the complete structure. As we will show, local information is valuable in characterizing the sliding layer structure and the observation of shear banding. Moreover, it reveals interesting differences between shear induced melting and crystallization.

### 3.2 Experimental details

The colloidal suspension used in our experiments consisted of  $1.2 \mu\text{m}$  diameter silica particles dispersed in ethoxylated trimethylolpropane triacrylate (ETPTA, Aldrich, MW. 428, viscosity  $\approx 0.07 \text{ Pa}\cdot\text{s}$ , density  $= 1.1 \times 10^3 \text{ kg/m}^3$ ). We used this solvent to have the possibility to polymerize and fix the samples, but in the experiments described in this chapter we did not make use of this possibility. The particle volume fraction was  $\phi \approx 0.5$ , which is in the fluid-crystal coexistence region. A  $0.4 \mu\text{m}$  diameter core of the particles was labeled with fluorescein isothiocyanate (FITC) by the method described in Reference [84]. This made it possible to image the particles with a confocal microscope after excitation of the dye with the 488 nm line of the Ar laser of the microscope. Imaging was done with a  $63\times$  Leica objective with 1.4

numerical aperture. The positions of the particles were determined by using algorithms similar to those of Crocker and Grier [104].

The experiments were performed in the shear cell described and characterized in Chapter 2. It was a parallel plate shear cell mounted on top of an inverted confocal microscope (TCS-SP2, Leica). The dimensions of the top glass plate were 30 mm in the  $x$ (velocity)-direction and 15 mm in the  $y$ (vorticity)-direction. The bottom glass plate was a standard no. 1 (thickness 0.13 – 0.16 mm) microscopy glass slide of 50 mm  $\times$  24 mm. We wanted to be able to image particles over the complete width of the cell. Because the working distance of the objective lens was 100  $\mu$ m, when one images through a no. 1 glass slide, the gap width was set smaller than 100  $\mu$ m. For each experiment we used as much as 100  $\mu$ l dispersion to be sure to overfill the cell preventing unwanted capillary forces to disturb the flow of the suspension.

Immediately after filling the shear cell the complete suspension was disordered although its volume fraction was higher than the bulk freezing volume fraction. The nucleation time in this viscous medium is expected to be much longer as the viscosity of ethoxylated trimethylolpropane triacrylate is 0.07 Pa·s (70  $\times$  that of water). An additional possible cause for disorder is a shear that was applied during filling of the cell. After placing a drop of the dispersion onto the bottom glass slide, the top cassette was placed into the top translation stage. This made the suspension drop to spread out resulting in a shear. We estimated the shear rate that was applied in this way, to determine whether this flow brought the suspension into the shear melting regime.

To estimate the shear rate we assumed that when the plates were brought together, the fluid flowed radially outwards with a Poiseuille flow. In a cylindrical coordinate system, as shown in Figure 3.2, the Poiseuille flow can be written as:

$$u(z, r) = C \left( \frac{h^2}{4} - z^2 \right), \quad (3.1)$$

where  $u(z, r)$  is the radial velocity,  $C$  a constant and  $h$  the gap width. The velocity depends both on the vertical position,  $z$ , and the radial position,  $r$ . The total radius of the droplet is much larger than the height. The relative change in radius is much smaller than the relative change in height and therefore, we can neglect the dependence of  $u$  on  $r$ . The volumetric flow rate at a distance  $R$  from the center is:

$$\frac{dV}{dt} = \int_{-h/2}^{h/2} 2\pi R u(z) dz = \frac{\pi C R}{3} h^3. \quad (3.2)$$

Because of incompressibility, this flow rate must equal the rate of change of the volume of a vertical cylinder with radius  $R$ :

$$\frac{dV}{dt} = \pi R^2 \frac{dh}{dt}, \quad (3.3)$$

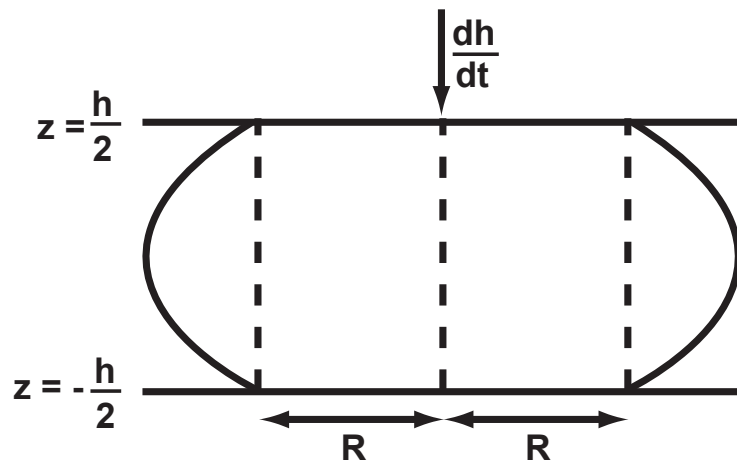


**Figure 3.2:** Schematic representation of a droplet that is sheared when the top plate of the shear cell is lowered into the top translation stage. The flow is assumed to be of the Poiseuille type.

where  $\frac{dh}{dt}$  is the speed with which the plates are brought together. This leads to the following expression for the constant  $C$ :

$$C = \frac{3R}{h^3} \frac{dh}{dt}. \quad (3.4)$$

The Poiseuille flow is thus equal to:

$$u(z) = \frac{3R}{h} \left( \frac{1}{4} - \frac{z^2}{h^2} \right) \frac{dh}{dt}. \quad (3.5)$$

Taking the derivative to  $z$  gives the shear rate:

$$\dot{\gamma}(z) = -\frac{6Rz}{h^3} \frac{dh}{dt}. \quad (3.6)$$

The maximum shear rate is found at the plates and equals:

$$\dot{\gamma}_{max}(z = \pm \frac{h}{2}) = \pm \frac{3R}{h^2} \frac{dh}{dt}. \quad (3.7)$$

At the edge of a 1 cm radius droplet with a thickness of 100  $\mu\text{m}$  that is compressed by a plate that is lowered with  $\frac{dh}{dt} = 0.1 \text{ mm/s}$ , the maximum shear rate is on the order of  $10^2 \text{ s}^{-1}$ . As will be shown later in this chapter, this is in the shear melting regime. Lowering the top plate onto the droplet could thus indeed shear melt a significant part of a crystalline suspension.

### 3.3 Results and discussion

#### 3.3.1 Flow profile of crystallizing suspensions

In Chapter 2 we showed that in this parallel plate shear cell the flow profile of a dilute colloidal suspension with a volume fraction of  $\phi = 0.22$  was linear.

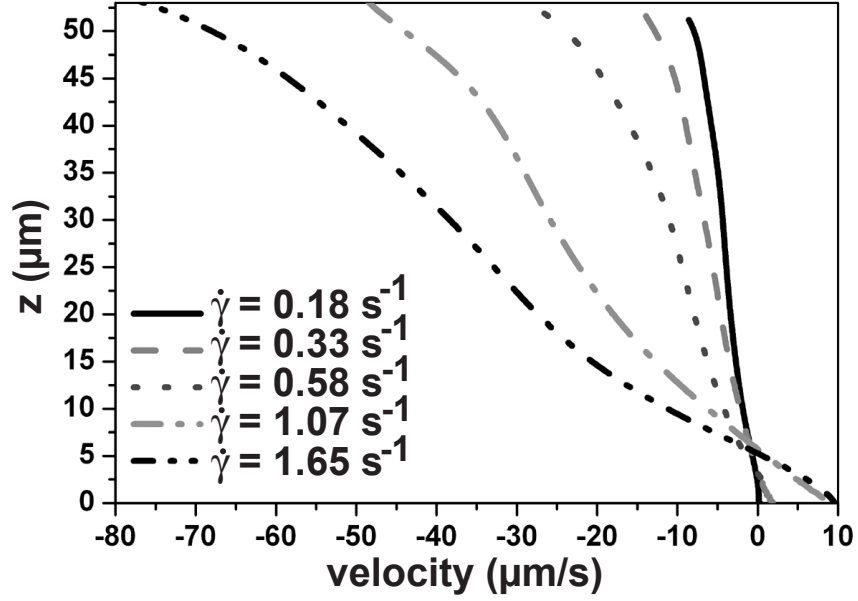


**Figure 3.3:** Flow profiles of a  $\phi = 0.5$  dispersion of  $1.2 \mu\text{m}$  diameter silica particles in ETPTA measured at several overall applied shear rates. The profiles were not linear; the local shear rate was significantly higher at both the top and bottom plate. The gap width was  $53 \mu\text{m}$ .

The flow profile of a partially crystallized suspension was completely different. From the velocity difference between two neighboring layers we determined that when the plates moved at a velocity ratio  $v_{\text{bottom}}/v_{\text{top}} = 0.16$ , the local shear rate around the zero-velocity plane was twice as large as the overall applied shear rate. The particles at this height were arranged in hexagonal layers. Derks *et al.* already observed that the shear rate in a crystal can be much higher than the overall applied shear rate [105]. In the cone-plate shear cell that they used, it was only possible to image particles in the bottom  $100 \mu\text{m}$  of the cell, whereas the gap width at the point of imaging was either  $0.4$  or  $1.7 \text{ mm}$ , depending on the cone used. The shear rate in the top part of that shear cell could thus not be measured. We set the gap width of our parallel plate shear cell at less than  $100 \mu\text{m}$ . This enabled us to measure the complete flow profile. To do so, we took images at a slow scan rate in the  $xz$ (velocity-gradient)-plane. The particles moved during the scan and therefore they appeared deformed in the image. From the deformation the local velocity can be determined accurately. This method was previously described by Derks *et al.* [34] and is explained in more detail in Chapter 2 of this thesis.

Figure 3.3 shows the flow profiles of a  $\phi = 0.5$  dispersion of  $1.2 \mu\text{m}$  diameter silica particles in ETPTA. The profile shows three regions: two close to the plates where the shear rate was significantly higher than the overall applied shear rate and one in the middle of the cell where the shear rate was lower. If a higher shear had only been measured at the top, it could have been explained

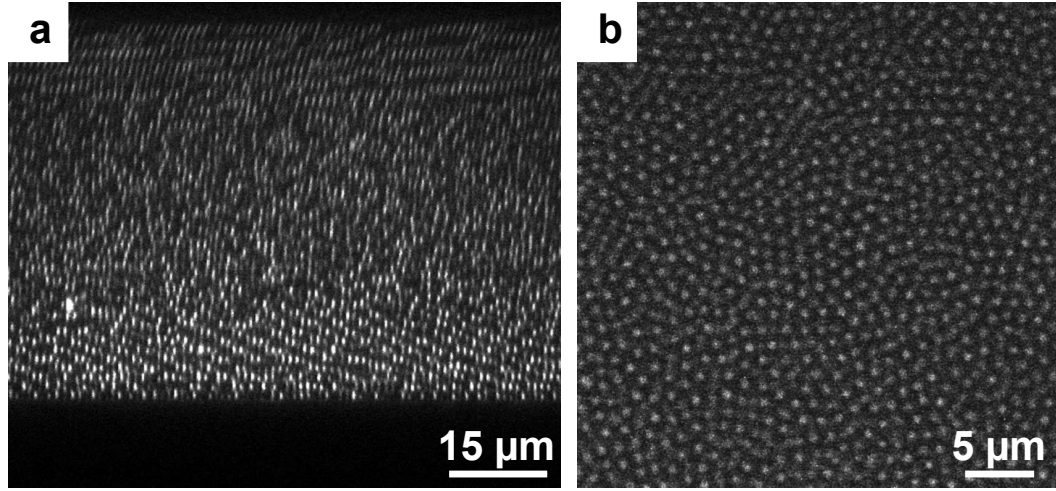


**Figure 3.4:** Confocal microscopy images taken right after cessation of the shear a) in the velocity-gradient plane and b) in the velocity-vorticity plane halfway the gap width. At both walls the particles arranged in layers. In the middle the structure contained liquid-like and small crystalline regions.

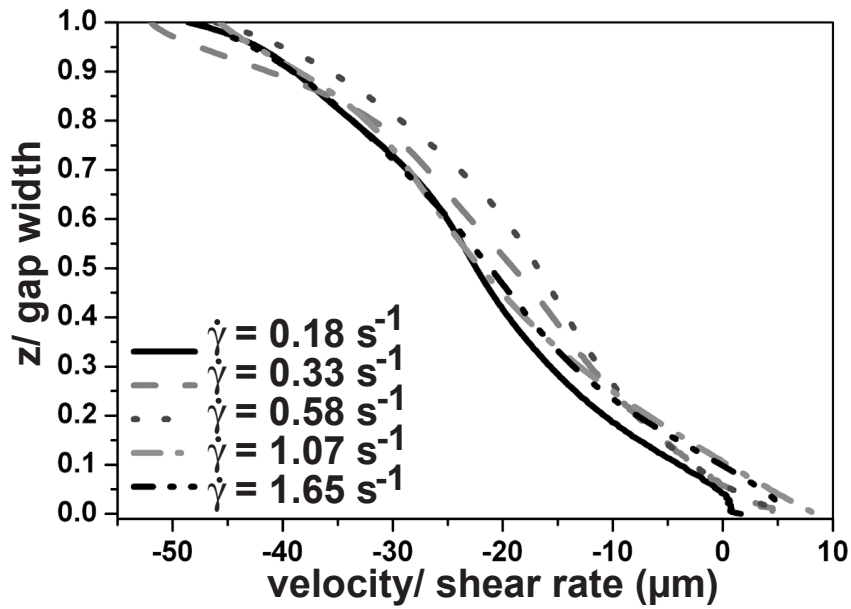


**Figure 3.5:** Flow profiles measured at different shear rates scaled with the shear rate and gap width. The scaled curves overlap showing that the profiles have a similar shape.

by sedimentation of the silica particles (density 2 g/ml) in its medium (density 1.1 g/ml). This would decrease the local volume fraction and thus the viscosity. However, the flow profile was more or less antisymmetric and a higher shear rate was also observed at the bottom wall where one would expect an even higher concentration in case of sedimentation. Therefore, we concluded that the local higher measured shear rates were caused by the walls. An  $xz$ -image taken right after cessation of the shear in Figure 3.4a shows that at the walls aligned layers were present. An  $xy$ -image (Figure 3.4b) taken halfway the gap shows that in the middle of the cell the particles were disordered or formed small crystalline domains. Most likely, the hexagonal layers parallel to the walls slid over each other, which decreased the local viscosity. This was earlier also suggested by rheological measurements [92, 93, 106].

Note that the flow profiles almost intersected in one point. The height of this point was at the same height as the zero-velocity plane in the case of a dilute suspension with a linear flow profile measured under the same shear conditions. In the case of a linear flow profile, it is obvious that the curves intersect at the zero-velocity plane. It is not straightforward that bent flow profiles also cross in one point. They only do so, when they have the same shape. Figure 3.5 shows that the flow profiles collapse when they are scaled with the overall applied shear rate and gap width. The profiles all had a similar shape. This observation indicates that the number of sliding layers at the walls was independent of the shear rate.

From the flow profile in Figure 3.3 the relative viscosity of the three regions can be deduced from the inverse of the slopes. We fitted the flow profile that was measured when applying an overall shear rate of  $\dot{\gamma} = 1.65 \text{ s}^{-1}$ , with a third order polynomial. Then, we calculated the inverse average slope of the curve in the three regions, each of  $5 \text{ }\mu\text{m}$  interval. Relative to the inverse slope in the middle, the inverse slope was 1.4 times and 1.6 times as steep at the top and bottom respectively. This means that on average the viscosity of the sliding layer structure was 1.5 times lower than that of the liquid-like structure.

### 3.3.2 Motion of crystalline layers

Under shear, colloidal suspensions above their bulk crystallization volume fraction form hexagonal layers in the velocity-vorticity plane with a close-packed line oriented in the flow direction [10, 61]. When we applied a continuous shear at a low shear rate to such a crystal, the sample stayed crystalline and the hexagonal layers moved over each other. As was previously suggested by Ackerson from scattering experiments [95] and observed in real-space by Derks *et al.* [34], the particles showed a collective zigzag motion. We analyzed this motion by taking time-series of a layer located in the zero-velocity plane. In each frame the particle coordinates were determined. From the displacement of the average position of the particles the trajectory of the center of mass of that hexagonal layer was calculated. In this calculation only the particles that



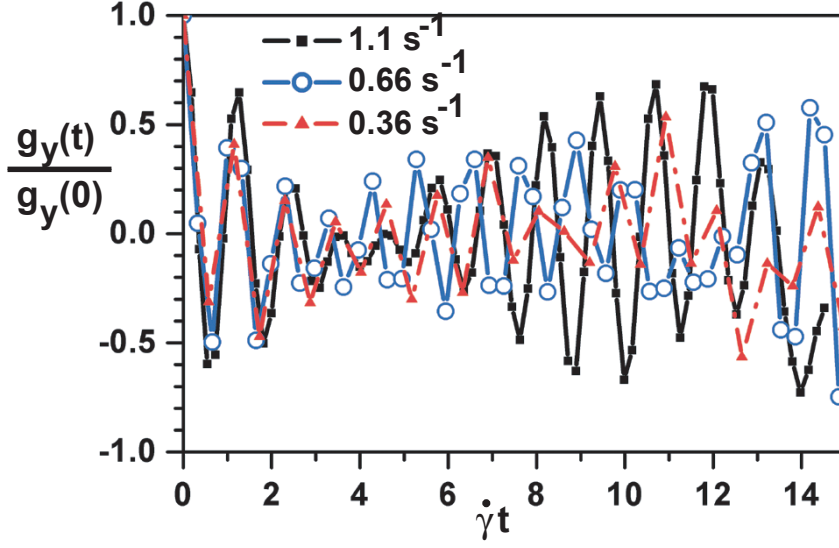


**Figure 3.6:** Autocorrelation function of the displacement of the center of mass in the vorticity direction of a hexagonal layer under shear versus the delay-time scaled by the shear rate. The period of the zigzag motion was equal to  $\tau = 1.17/\dot{\gamma}$ .

were observed in both frames were taken into account.

$$\vec{r}_{CM}(t) = \sum_{t'=\Delta t}^t \frac{1}{N_{t'}} \sum_{i=1}^{N_{t'}} (\vec{r}_i(t') - \vec{r}_i(t' - \Delta t)), \quad (3.8)$$

where  $\vec{r}_i(t')$  is the position of particle  $i$  at time  $t'$ .  $N_{t'}$  is the number of particles observed both in frame  $t'$  and frame  $(t' - \Delta t)$  and  $\Delta t$  is the time between two frames. We are interested in the collective movement in the vorticity( $y$ )-direction and therefore we calculated the autocorrelation function of  $\vec{y}_{CM}$ :

$$g_y(j\Delta t) = \frac{1}{N-j} \sum_{i=0}^N y_{CM}(t_i) y_{CM}(t_i + j\Delta t), \quad (3.9)$$

where  $N$  is the total number of frames of the time series,  $\Delta t$  is the time between two consecutive frames. The correlation of the zigzag motion is visible for more than 10 oscillations. In Figure 3.6 we scaled time with the local shear rate. Because of a slightly different period the zigzag motions measured at the three different shear rates run slowly out of phase after several oscillations. This difference is, however, small and during the first few periods the curves overlap nicely indicating that, in this range of shear rates, the frequency of the zigzag motion scaled with the shear rate.

The hexagonal layers move along a zigzag path because each layer slides in the “valleys” formed by the underlying layer. The trajectory is illustrated in Figure 3.1. In equilibrium the particles of a hexagonal layer reside in the interstices formed by the particles of the next layer. The period,  $\tau$ , of the



zigzag motion observed in a shear flow is thus expected to be equal to the time needed to move from one set of interstices to the next:  $\tau = \frac{\lambda}{\Delta v}$ , where  $\lambda$  is the in-plane interparticle distance and  $\Delta v$  the velocity difference between two neighboring layers. The velocity difference between two layers is  $\Delta v = \dot{\gamma}\Delta z$ , where  $\Delta z$  is the distance between the layers. This distance in equilibrium equals to  $\Delta z = \frac{\sqrt{6}}{3}\lambda$ . The period of the zigzag motion is thus expected to be equal to  $\tau = \frac{3}{\dot{\gamma}\sqrt{6}} \approx 1.22/\dot{\gamma}$ .

To compare this with the experimental period of the zigzag motion, we first had to determine the local shear rate. As discussed above the local shear rate was not equal to the overall applied shear rate. Therefore, we determined the local shear rate by taking the ratio of the velocity difference of two layers and the distance between these layers. Because our dispersion has a different refractive index ( $n \approx 1.47$ ) than the glass slides and immersion oil ( $n = 1.52$ ), actual distances along  $z$  are different from measured distances. There are models to calculate the factor to correct for this difference (see e.g. [107]), but here, we assume the layer separation to be equal to the separation in equilibrium. Scaling the correlation functions with this local shear rate, shown in Figure 3.6, revealed that the zigzag motion had a period of  $1.17/\dot{\gamma}$ . This is nearly equal to the expected period and we can conclude that the layers indeed perform a zigzag motion because they move through the “valleys” formed by the particles of the underlying layer. That the observed frequency of the zigzag motion is slightly higher than the expected frequency, may be caused by an increase in the separation between the layers compared to a crystal in equilibrium. The difference is, however, small.

### 3.3.3 Shear induced melting and crystallization

As mentioned above, the flow profile after crystallization was not linear any more due to the formation of a sliding layer structure. Therefore, the flow profile and thus the local shear rate in the zero-velocity plane are expected to change during melting and crystallization. The local shear rate can in principle be determined by measuring the velocity of the layer just above and below the zero-velocity plane or by taking  $xz$ -images at a slow scan rate. The observations in this section about crystallization and melting under shear were done by taking time-series in the zero-velocity plane. Because it was not possible to take  $xz$ -images at the same time, the local shear rates were not exactly known. Therefore, the shear rates mentioned in this section are the overall applied shear rates.

When a sufficiently high shear rate was applied to a crystallized system, the particles became disordered. The overall applied shear rate needed to induce shear melting was  $2 \text{ s}^{-1}$ . The snapshots of particles in the zero-velocity plane in Figure 3.7 show how the shear induced melting evolved in time. The state of the system remained highly dynamic: overall the order decreased, but the local order now and then increased strongly after which it decreased again.

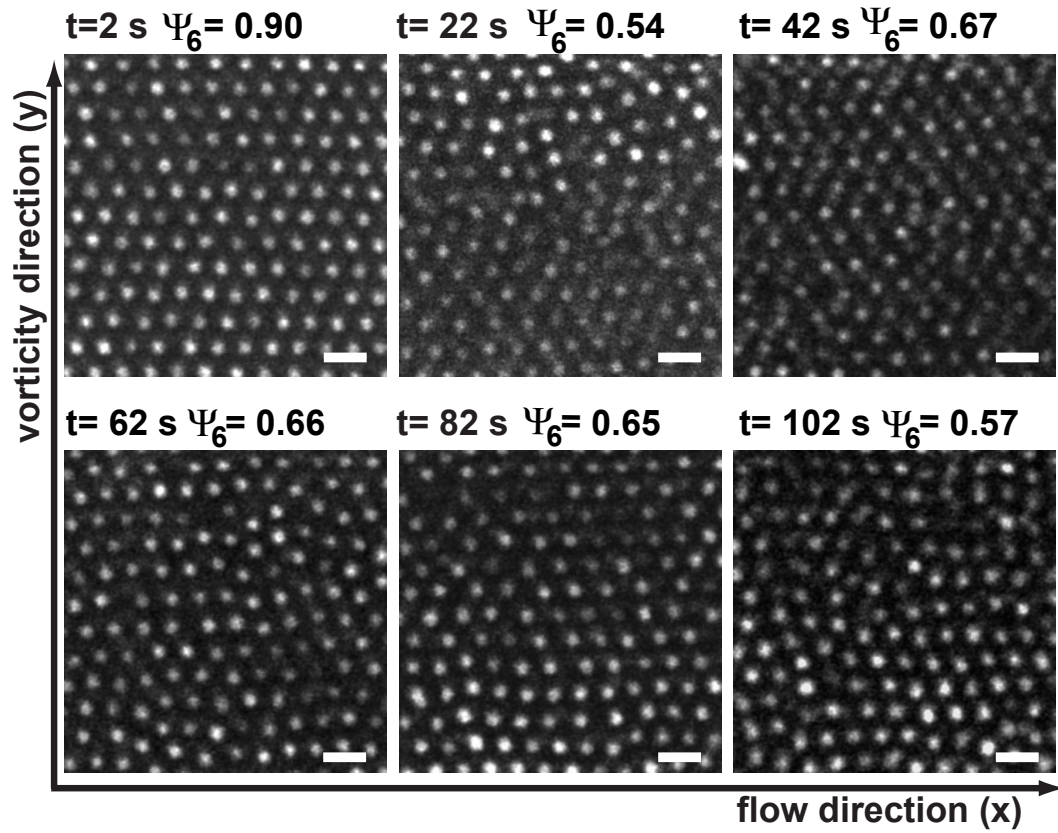


**Figure 3.7:** Confocal microscopy images taken in the velocity-vorticity plane of an initially crystalline suspension of  $1.2 \mu\text{m}$  diameter silica particles in ETPTA sheared with  $\dot{\gamma} = 2 \text{ s}^{-1}$ . Initially the structure was crystalline, but it became largely disordered, although ordered regions temporarily formed. The scale bars are  $2 \mu\text{m}$ .

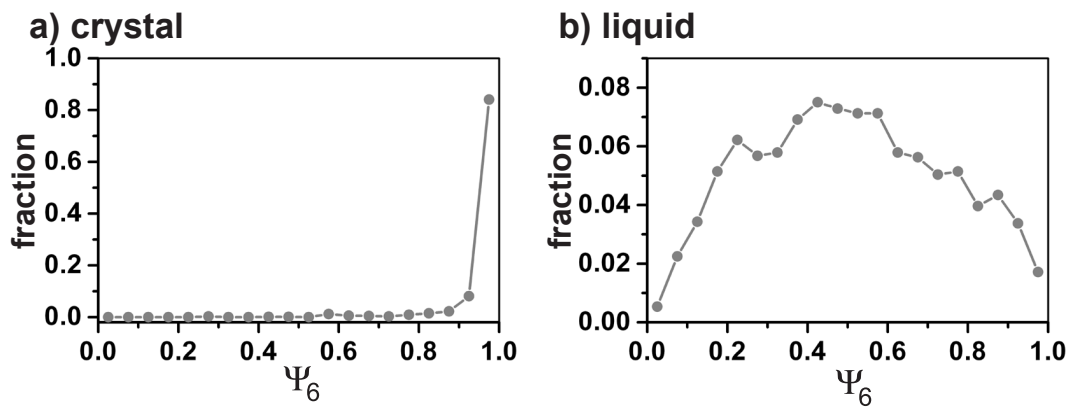


**Figure 3.8:** a) Histogram of  $\psi_6$  values of particles crystallized in an unsheared hexagonal lattice. b) Histogram of the calculated  $\psi_6$  values of particles in a pure liquid. The data were collected on a suspension at the same volume fraction as in the shear melting and crystallization experiments.

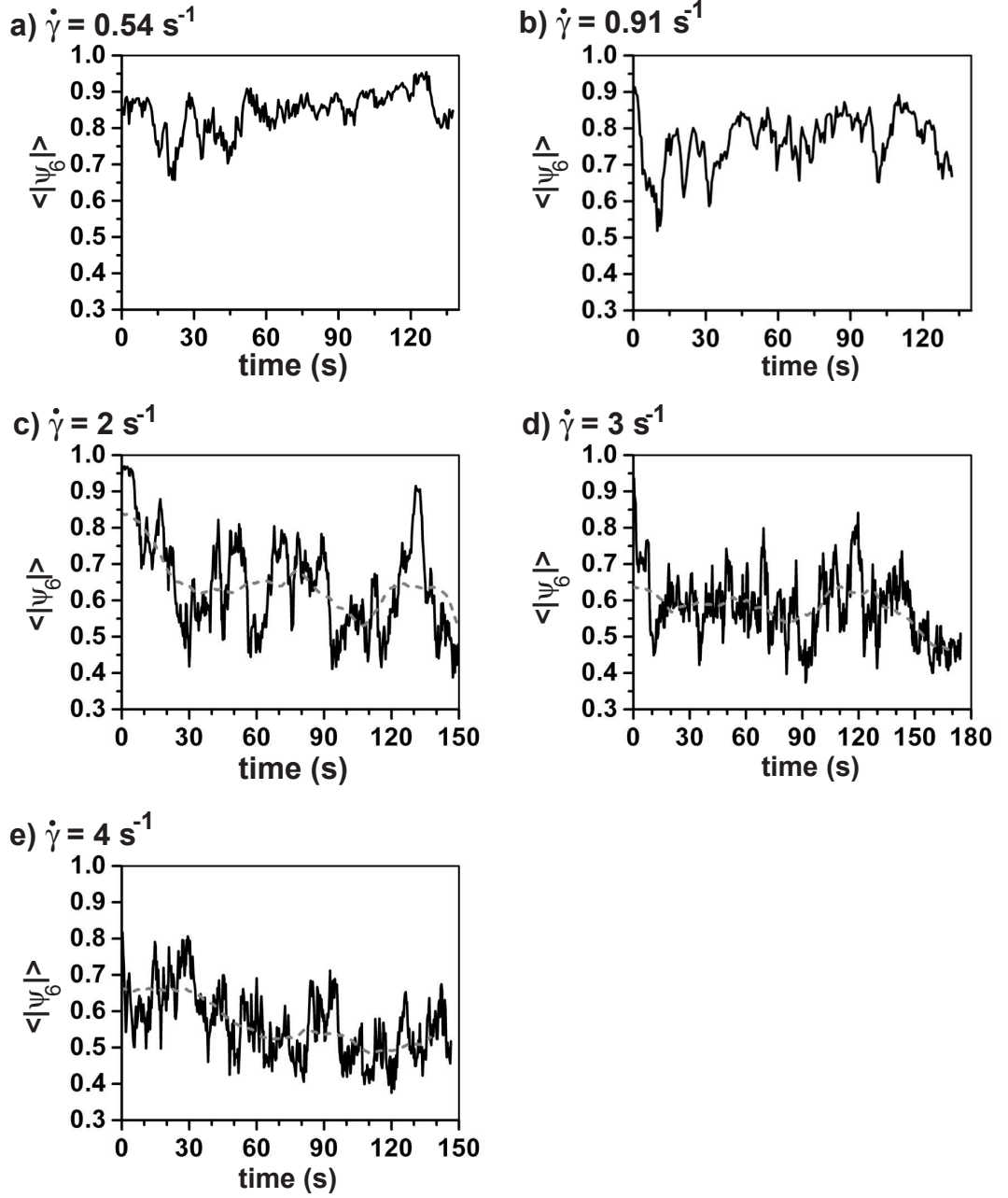


**Figure 3.9:** Initially crystalline suspensions of 1.2  $\mu\text{m}$  diameter silica particles in ETPTA sheared at shear rates of a)  $\dot{\gamma} = 0.54 \text{ s}^{-1}$ , b)  $\dot{\gamma} = 0.91$ , c)  $\dot{\gamma} = 2 \text{ s}^{-1}$ , d)  $\dot{\gamma} = 3 \text{ s}^{-1}$  and e)  $\dot{\gamma} = 4 \text{ s}^{-1}$ . The average order, quantified by  $\psi_6$ , is plotted as a function of time. The dashed line is after smoothing the curve by averaging each point over a time interval of 40 s.

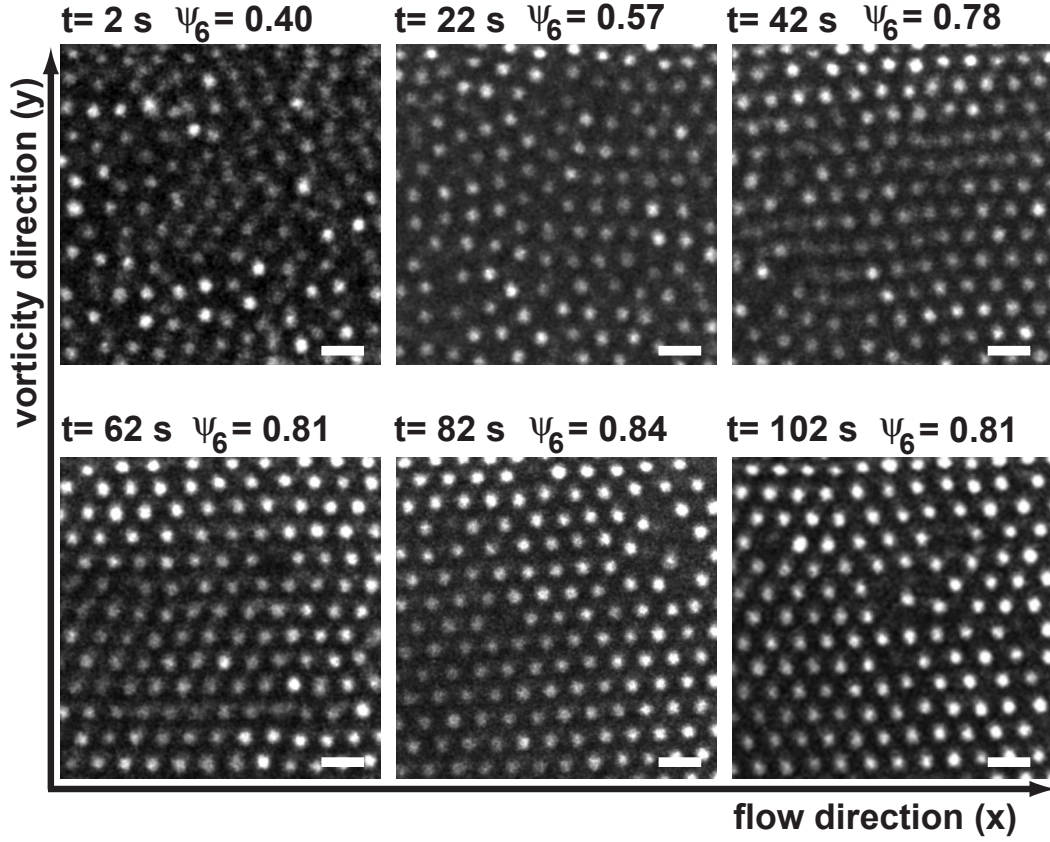


**Figure 3.10:** Confocal microscopy snapshots of a concentrated suspension of 1.2  $\mu\text{m}$  diameter silica particles in ETPTA sheared with  $\dot{\gamma} = 0.45 \text{ s}^{-1}$  starting as a disordered suspension. The scale bars are 2  $\mu\text{m}$ .

To quantify the degree of order we calculated for each particle the local bond-orientational order parameter  $\psi_6$ .

$$\psi_6(r_{ij}) = \frac{1}{n_c} \sum_{j=1}^{n_c} e^{i6\theta(r_{ij})}. \quad (3.10)$$

The order parameter  $\psi_6$  of particle  $i$  is a summation over all its  $n_c$  nearest neighbors.  $\theta(r_{ij})$  is the angle between the vector connecting particle  $i$  to  $j$  and an arbitrary fixed reference axis. In a perfect hexagonal layer the angles between the six nearest neighbors are multiples of  $60^\circ$  and  $\psi_6 = 1$ . Figure 3.8a shows a histogram of the  $\psi_6$  values of the particles in a perfect hexagonal layer. Almost all particles have a  $\psi_6$ -value larger than 0.8.

Figure 3.9 shows the evolution of the average value of  $\psi_6$  over time when different shear rates were applied. At low shear rates of  $\dot{\gamma} = 0.54 \text{ s}^{-1}$  (Figure 3.9a) the value of  $\psi_6$  fluctuated, but stayed around 0.8. These fluctuations were larger when a shear rate of  $\dot{\gamma} = 0.91 \text{ s}^{-1}$  (Figure 3.9b) was applied, but  $\psi_6$  stayed between 0.7 and 0.8. The transition to a liquid was not complete.

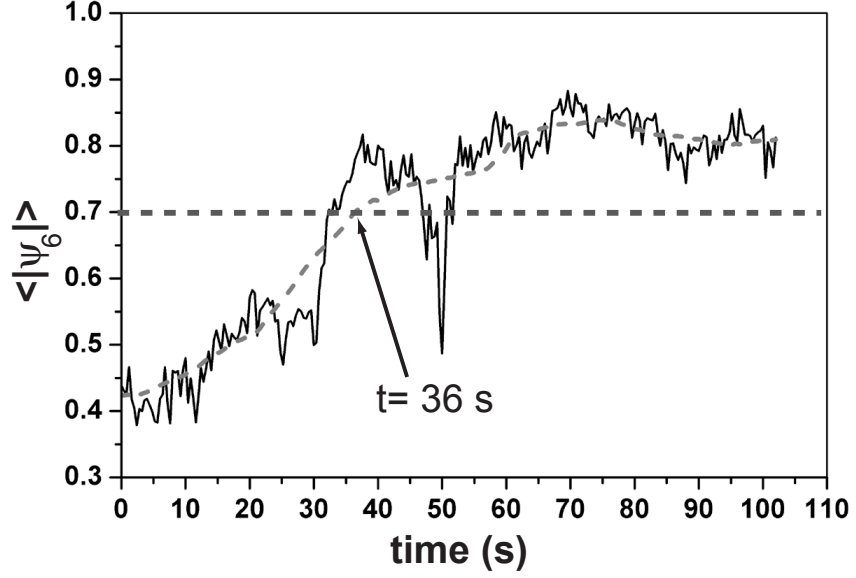


**Figure 3.11:** Average order, quantified by  $\psi_6$ , of a concentrated suspension of 1.2  $\mu\text{m}$  diameter silica particles in ETPTA, when it was sheared with a shear rate of  $0.45\text{ s}^{-1}$ . The dashed line is the curve smoothed by averaging each point over a time interval of 20 s. After 36 s this curve crossed the boundary value of 0.7 and the structure was assumed to have crystallized.

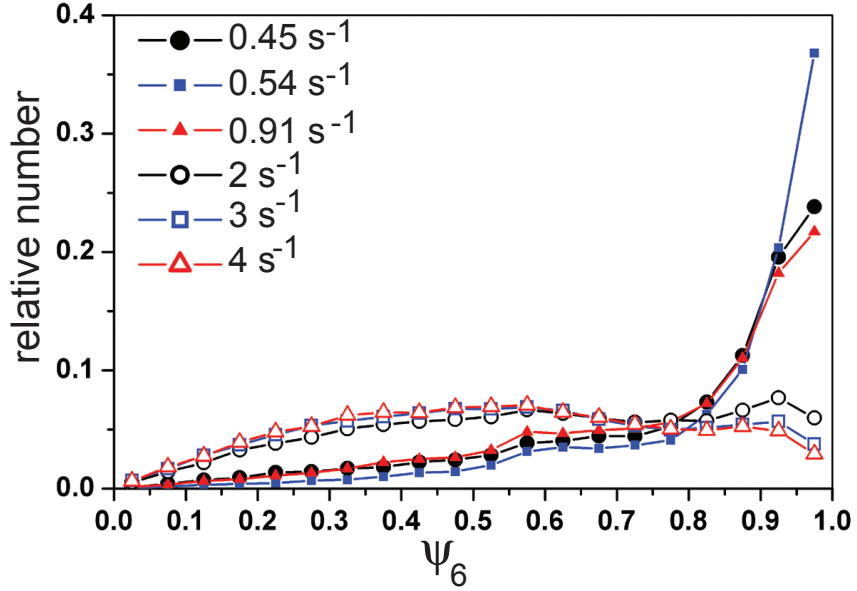


**Figure 3.12:** Histograms of the individual  $\psi_6$  values of particles during shear induced melting ( $\dot{\gamma} \geq 2\text{ s}^{-1}$ , open symbols) and crystallization ( $\dot{\gamma} = 0.45\text{ s}^{-1}$ ) after the transition to a liquid or a crystal respectively. A crystal did not melt under intermediate shear rates ( $\dot{\gamma} = 0.54\text{ s}^{-1}$  or  $0.91\text{ s}^{-1}$ ).

Only when a shear rate of at least  $\dot{\gamma} = 2 \text{ s}^{-1}$  (Figure 3.9c) was applied, the value of  $\psi_6$  dropped below 0.7 and we set  $\psi_6 = 0.7$  as the boundary value below which we assumed the hexagonal layer to have melted. For an indication about the time needed for the hexagonal layer to melt, we smoothed the graph by taking for each point at  $t = t$ , the average of  $\langle |\psi_6| \rangle$  from  $(t-20 \text{ s})$  to  $(t+20 \text{ s})$ . This is the dashed line in Figure 3.9c. After 19 seconds the smoothed curve dropped below the chosen boundary value of 0.7 and the crystalline layer was said to have melted. At higher shear rates the crystal melted much faster: when a shear rate of  $\dot{\gamma} = 3 \text{ s}^{-1}$  or  $4 \text{ s}^{-1}$  was applied a crystal melted almost instantaneously (Figure 3.9d and e).

Conversely, when we applied a low shear rate to an initially disordered suspension the particles started to order. We used suspensions with a concentration in the fluid-crystal coexistence region that were made disordered by applying a shear with high shear rate to it. Then, we applied a shear rate of  $\dot{\gamma} = 0.45 \text{ s}^{-1}$  and monitored the local ordering of the particles in the zero-velocity plane. Snapshots of a time-series are shown in Figure 3.10. In the beginning the suspension was disordered. Then, the order increased until a hexagonal layer was formed of which the order did not change significantly in time. The orientation of the hexagonal layer was such that a close-packed line was always parallel to the flow direction.

This is also visible in the average absolute value of  $\psi_6$  (Figure 3.11). The average  $\psi_6$  fluctuated somewhat, but in general it showed a clear increasing trend. We smoothed the curve by taking the average of  $\langle |\psi_6| \rangle$  from  $(t-10 \text{ s})$  to  $(t+10 \text{ s})$  (dashed line in Figure 3.11). After 36 seconds the smoothed curve exceeded the boundary value of 0.7 and the layer had crystallized.  $\langle |\psi_6| \rangle$  kept fluctuating, but except for one sharp dip it stayed at a value around 0.8.

It is remarkable that the  $\langle |\psi_6| \rangle$  fluctuations were very much larger during shear melting than during shear crystallization. Both the snapshots and the graphs of  $\langle |\psi_6| \rangle$  versus time point to a clear difference between shear induced melting and crystallization. Shear induced melting is apparently a local process during which small disordered domains form that now and then order again. During shear induced crystallization the particles collectively ordered, without much local fluctuation.

To further analyze the difference between shear induced melting and crystallization, we looked more closely at the distribution of  $\psi_6$  values of the individual particles. We determined  $\psi_6$  for each individual particle from the transition to a crystal (in the case of shear crystallization) or to a liquid (shear melting) to the end of the time-series. Then, we made a histogram of these values (Figure 3.12). In the experiment of shear induced melting both disordered and ordered domains were present, which is shown by the almost bimodal distribution. The broadness of the peak of  $\psi_6$  values of the disordered particles is similar to that of a histogram of  $\psi_6$  values of particles of a pure liquid (Figure 3.8b). This distribution of  $\psi_6$  values was not unique for melting at a shear rate



of  $\dot{\gamma} = 2 \text{ s}^{-1}$ . When a crystal was melted by applying a shear rate of  $\dot{\gamma} = 3 \text{ s}^{-1}$  or  $\dot{\gamma} = 4 \text{ s}^{-1}$ , a histogram of  $\psi_6$  was similar to the one at  $\dot{\gamma} = 2 \text{ s}^{-1}$  (Figure 3.12).

A histogram of the  $\psi_6$  values of the individual particles after shear crystallization was completely different. Except from one dip, the order hardly changed after the crystallization time of 36 s and the majority of the particles stayed ordered (closed circles in Figure 3.12). Compared to a pure crystalline hexagonal lattice (Figure 3.8a), this fraction was larger. When the layers move along a zigzag path the particles undergo more collisions. Together with the hydrodynamics under shear this leads to a larger mean square displacement and thus larger deviations from a hexagonal symmetry within the layers.

### 3.4 Conclusions and outlook

We studied colloidal suspensions in the fluid-crystal coexistence region under shear. We examined them with confocal microscopy, which allowed us to observe individual particles as well as local and temporal behavior of crystalline order. In these crystallizing colloidal suspensions the flow profile was not linear. Three regions were discerned. Both at the bottom and at the top plate the shear rate was higher than that halfway the gap width. A scan in the velocity-gradient plane taken right after cessation of the shear showed that the particles formed layers at the two walls. The sliding of layers reduced the viscosity. From the slope of the flow profile it was deduced that the effective viscosity of the sliding layer structure was a factor of 1.5 smaller than halfway the gap, where the structure was liquid-like. The shape of the flow profiles of these concentrated suspensions did not change when the shear rate was varied. This suggested that the width of the three regions, i.e. the number of layers at the walls, was independent of the shear rate.

When a crystalline colloidal suspension consisting of hexagonal layers parallel to the velocity-vorticity plane was sheared at a low shear rate the particles in the hexagonal layer showed a periodic collective motion in the vorticity direction. The measured period of this zigzag motion was  $\tau_{exp} = 1.17/\dot{\gamma}$ . This is very close to the theoretical period of  $\tau = 1.22/\dot{\gamma}$ , of particles that collectively zigzag through the “valleys” formed by the underlying layer.

When a high shear rate of  $\dot{\gamma} \geq 2 \text{ s}^{-1}$  was applied to a crystalline suspension shear induced melting occurred. This was a highly local process: the average order decreased in time, but locally small domains could nucleate after which they melted again. This was also reflected by the change in the bond-orientational order parameter  $\psi_6$ , which showed a decreasing trend but kept fluctuating between 0.4 and 0.8. A histogram of the  $\psi_6$ -values of the individual particles had an almost bimodal distribution. Conversely, the application of a shear with an overall shear rate lower than  $\dot{\gamma} = 2 \text{ s}^{-1}$  to an initially disordered suspension above its bulk crystallization volume fraction induced crystalliza-

tion. Whereas shear induced melting was a local process crystallization was a gradual process taking place uniformly throughout the suspension. The order increased monotonously. After reaching crystallinity the order remained, without large fluctuations. Remarkably, this scenario of melting and crystallization induced by shear is roughly opposite to that without shear. In the latter case, it is crystallization that takes place through nucleation and growth, whereas melting proceeds uniformly from the surface of a crystal inward.

## Acknowledgements

First of all, we would like to thank Joost Brand and all others from the Instrumentele Groep Fysica (IGF, Utrecht University), who participated in the design and construction of the parallel plate shear cell. Furthermore, we thank Didi Derks for useful discussions about the analysis of the flow profiles and the zigzag motion. Roel Dullens is thanked for his help with the analysis of the change of the order parameter.





# 4

## Formation of colloidal crystals by spin coating

### Abstract

Spin coating is widely used to make thin polymer films. Here, we used spin coating to fabricate films of colloidal crystals. Just like polymer films, the thickness of the resulting colloidal crystals was found to be inversely proportional to the spin speed and the square root of the spin time. With confocal microscopy the 3D structure was revealed. The crystals consisted of randomly stacked hexagonal layers parallel to the substrate with a line with the highest density of particles pointing radially outwards. This orientation is similar to that generally obtained in shear flow. The particles were either practically touching with a nearest-neighbor distance of 1.1 times their diameter or non-touching with a nearest-neighbor distance of 1.4 times their diameter. In both cases, the separation between the layers was 0.8 times the in-plane interparticle distance. The symmetry was thus the same as that of a structure of close-packed hexagonal layers. Whether a crystal of touching or of non-touching particles formed did not depend on the initial volume fraction, spin time or spin speed, substrate pretreatment or substrate size. It probably depended subtly on a combination of the ionic strength of the medium and the surface charge of the particles. The transition from structures of touching to non-touching particles was thus located at different values for particles of different sizes.

## 4.1 Introduction

Spin coating is widely used in industry. It is an ideal process for making thin films over large (hundreds of  $\text{cm}^2$ ) areas, because it is fast, simple and uses only little material. With this technique it is possible to make thin films of uniform thickness of various polymers such as photoresists or protective coatings. A polymer is dissolved in a volatile solvent, which evaporates during spin coating, leaving a uniform film of the nonvolatile polymer behind [108]. Spin coating is also used to deposit inorganic colloidal particles for instance as anti-reflective coatings on optical components [109, 110].

In these cases mainly the thickness and the uniformity of the films are important. These properties can be tuned by the spin time and spin speed. The dependence as given by the model for Newtonian fluids of Emslie *et al.* [111] is derived in the next section. Further discussions about spin coating of Newtonian liquids can e.g. be found in References [112–116]. For models for non-Newtonian liquids that exhibit a “power-law” behavior we refer to Ref. [117, 118] and for Bingham fluids to Ref. [119].

More recently, spin coating has been used in colloid science to fabricate materials with regularly ordered particles. Research has been done on spin coating monolayers of particles in the nanometer size range that arrange in a hexagonal lattice [120]. Recently, Mihi *et al.* made 3D colloidal crystalline structures by spin coating [121]. By tuning the experimental parameters they were able to control the thickness of the crystals and their orientation. Wang and Möhwald fabricated binary crystals by stepwise spin coating [122]. Their method is a spin coating equivalent of the fabrication method of Velikov *et al.* [123] for making binary crystals. Instead of applying layers of differently sized particles layer-by-layer by controlled drying, Wang and Möhwald grew binary crystals by consecutively spin coating layers of large or small particles. In combination with lithography spin coating can be used to direct the position of particles [124–126]. First, a template is made on a substrate by lithography. Then, particles dispersed in a volatile medium are spin coated slowly to fill the grooves, and lastly the spin speed is increased to remove the excess of particles. By carefully choosing the dimensions of the grooves, the particles can be forced to adopt a specific crystal structure. After removing the template, colloidal crystals with a certain crystal structure and with a certain orientation are obtained.

In all these cases the medium is a volatile solvent that evaporates during or immediately after spin coating. Jiang and McFarland fabricated crystals by spin coating dispersions of colloidal particles dispersed in a much less volatile medium [21]. The medium consisted of a monomer that could be polymerized by illumination with UV light. Interestingly, the structures consisted of hexagonal layers in which the particles did not touch each other. The spacing between the layers was such that the particles were in contact with particles

in the neighboring layers. They made the structures permanent by polymerization of the medium, an approach that allows to make structures permanent even if the particles are non-touching in all directions. The symmetry of the structures that Jiang and McFarland fabricated was different from that of a face centered cubic (FCC) or a random hexagonal close packed structure, which we will refer to as an FCC-like structure. The structures that Jiang and McFarland found can be regarded as an FCC-like structure that is compressed perpendicular to the hexagonal layers and thus non-close packed. They used scanning electron microscopy to examine the structure. They were thus only able to examine the outer layers.

We performed similar experiments, but by using micron-sized, fluorescently labeled particles we were able to examine the structures with confocal microscopy. This enabled us to determine the 3D structure both before and after polymerizing the medium.

## 4.2 Theory of spin coating

The formation of films by spin coating can be divided in four stages: 1) The deposition of fluid on the substrate; 2) The spin-up stage in which the entire substrate becomes covered with the liquid. This is usually done by spinning the substrate slowly. A film of almost uniform thickness forms. 3) The spin-off stage in which excess of fluid is removed from the substrate by spinning the disk at a high speed. The film becomes thinner in this stage. 4) Evaporation of the solvent. Most models only consider the third stage. For us, this is the most interesting one, because, in this case, solvent evaporation is slow. In this paragraph we briefly discuss the thinning of the film in a simplified model.

We make the following assumptions:

- The fluid is Newtonian.
- The spin coating process is cylindrically symmetric.
- There is net flow in radial direction only, i.e.  $v_z \approx 0$ ,  $v_\theta \approx r\omega$ , where  $v_z$  is the velocity in vertical direction,  $v_\theta$  the azimuthal velocity,  $r$  the radial position and  $\omega$  the angular velocity or spin speed.
- There is no evaporation and the density of the fluid stays constant during the process.
- In stage 2 the film has become uniform in thickness.

We write the equation of motion in cylindrical coordinates and with the given assumptions the  $r$ -component of the velocity,  $v_r$ , is the only non-vanishing component. The force balance is:

$$-\rho r \omega^2 = \eta \frac{\partial^2 v_r}{\partial z^2}, \quad (4.1)$$

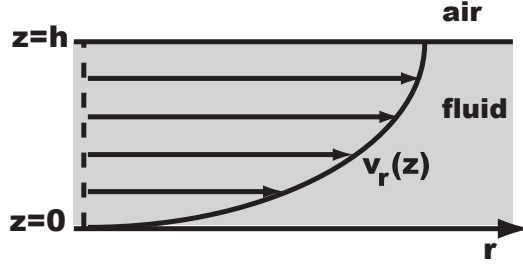


**Figure 4.1:** The flow profile during spin coating is half of a parabola.

where  $\rho$  is the density,  $\eta$  the viscosity of the dispersion,  $v_r$  the velocity in radial direction and  $z$  the height.

Assuming no-slip at the substrate and zero stress at the free interface, the boundary conditions are:

$$\begin{aligned} \text{at } z = 0: & \quad v_r = 0 \\ \text{at } z = h: & \quad \frac{\partial v_r}{\partial z} = 0, \end{aligned}$$

where  $h$  is the local film thickness.

Integration gives the maximum shear rate and the radial velocity as a function of height. The flow profile is half of a parabola as depicted in Figure 4.1.

$$\left(\frac{\partial v_r}{\partial z}\right)_{max} = \frac{\rho\omega^2 h}{\eta} \quad (4.2)$$

$$v_r(z) = \frac{\rho\omega^2 h^2}{\eta} \left(\frac{z}{h} - \frac{1}{2}\left(\frac{z^2}{h^2}\right)\right). \quad (4.3)$$

Integration of the radial velocity over all  $z$ ,  $r$  and  $\theta$  divided by  $2\pi rh$  gives the average radial velocity,  $\langle v_r \rangle$ . Multiplication of  $\langle v_r \rangle$  by  $h$  gives the volumetric flow rate per unit circumference:

$$q = \frac{\rho\omega^2 r h^3}{3\eta}. \quad (4.4)$$

During spin coating the volume change of the film in time is inversely proportional to this volumetric flow rate. Quantitatively, this is expressed by the equation of continuity as:

$$\frac{\partial h}{\partial t} = -\frac{1}{r} \frac{\partial r q}{\partial r} = -\frac{\rho\omega^2}{3\eta r} \frac{\partial}{\partial r} (r^2 h^3). \quad (4.5)$$

We have assumed that after the spin-up stage the film is uniform in thickness, i.e.  $h(r, t) = h(t)$ . The solution of Equation 4.5 then becomes:

$$\frac{dh}{dt} = -\frac{2\rho\omega^2 h^3}{3\eta}, \quad (4.6)$$

which after integration gives the thickness as a function of time:

$$h(t) = \frac{h_0}{\left(\frac{4\rho\omega^2 h_0^2 t}{3\eta} + 1\right)^{1/2}}. \quad (4.7)$$

When the first term in the denominator is much larger than 1, the film thickness is inversely proportional to  $\omega t^{1/2}$ .

$$h = \sqrt{\frac{3\eta}{4\rho\omega^2 t}}. \quad (4.8)$$

Furthermore, Walker and Thompson experimentally found that the thickness is independent of the initial volume as long as it is sufficient to cover the entire substrate [127].

Especially at high volume fractions the flow behavior of a colloidal dispersion is not expected to obey Newton's law of viscosity. Still, we use this model to understand the general effects of spin coating on the ordering of the colloids in the fluid. In fact, spin coating brings the suspension in a shear flow, with the maximum shear rate at the substrate and a zero shear rate at the top surface. Based on our studies in Chapter 3 depending on the shear rate, crystallization or melting can be expected to be induced. Moreover, a parabolic flow profile is also to occur in dispersions flowing through rectangular capillaries [11, 13, 90].

## 4.3 Experimental details

### 4.3.1 Dispersions

The dispersions consisted of silica particles dispersed in ethoxylated trimethylpropane triacrylate (ETPTA, Aldrich, MW. 428, boiling point = 157°C, viscosity  $\approx 0.07$  Pa·s, density =  $1.1 \times 10^3$  kg/m<sup>3</sup>). 1 wt% of the photoinitiator 2-hydroxy-2-methyl-propiophenone (Darocur 1173, 97%, Aldrich) was added to allow initiation of the polymerization reaction by illumination with short wave UV light of 254 nm (UVGL-58, UVP).

Microscopy requires the objects to be of the order of a micrometer or larger. Therefore, we originally only used 1.2  $\mu\text{m}$  diameter sized silica particles synthesized via a Stöber growth [83]. A 0.4  $\mu\text{m}$  diameter core of the particles was fluorescently labeled with fluorescein isothiocyanate (FITC) using the method of Van Blaaderen and Vrij [84]. Two other types of particles were used later on: 0.79  $\mu\text{m}$  diameter silica particles of which a 0.4  $\mu\text{m}$  core was labeled with FITC, and 0.4  $\mu\text{m}$  diameter unlabeled silica particles.

The solvent used in all stock suspensions was ethanol. The dispersions for spin coating were made by taking a known volume of the stock dispersion of known concentration. After centrifugation the ethanol was removed with a pipet and ETPTA was added until the desired particle volume fraction was

reached. The resulting dispersion was kept overnight in an open vial to remove possible traces of ethanol by evaporation.

The conductivity of these suspensions was varied by adding salt or by deionization of the medium. The conductivity was measured using a 627 conductivity meter (Scientifica). To increase the conductivity, 1 mM LiCl (pro analyse, Merck) was added. Two methods were used to deionize the system. One method was to add an ion exchange resin (Biorad AG 501-X8 resin, 20-50 mesh, biotechnology grade) to a vial with the monomer. After mixing this for a week in the vial on a roller band, the ion exchange resin was removed. The deionized monomer was then used to make dispersion as described above. The second method was to bring ETPTA into contact with glycerol, which is more polar than ETPTA and does not mix with it. Ions are expected to partition preferentially to the glycerol phase [128]. As ETPTA has a slightly lower density, it could easily be taken off after allowing the solvents to phase separate. In one week both methods made the conductivity drop by one order of magnitude to  $\sim 2.5 \times 10^4$  pS/cm. It is possible that traces of ammonia from the reaction mixture stay behind in the slightly porous silica particles. To remove these traces, part of the stock solutions of silica particles was dried from ethanol by heating it to 120°C for 24 hours so that all the ethanol, water and ammonia evaporated. After redispersing the particles by adding ETPTA the dispersion was immediately used to make films by spin coating.

#### 4.3.2 Spin coating of films

The substrates on which the films were spin coated were standard microscopy round 22 mm diameter no.1 glass slides. They were cleaned with chromosulfuric acid. To improve the wetting and possibly induce a chemical attachment, some substrates were coated with 3-(trimethoxysilyl)propyl acrylate. This was done by placing them for 2 hours in a mixture of 210 ml technical ethanol, 6 ml ammonia (25%) and 10  $\mu$ l 3-(trimethoxysilyl)propyl acrylate (92%, Aldrich).

A droplet of 15–20  $\mu$ l of the dispersion was spread on a 22 mm diameter circular substrate and then spin coated. The spin coater (model P6700, Specialty Coating Systems, USA) first rotated slowly (200–800 rpm) for one or two minutes to obtain a more or less uniform layer and then fast (1000–4000 rpm) for a few minutes to reach the desired film thickness.

The samples were polymerized by placing them in a glass sample chamber under a continuous nitrogen flow and illuminating them through the glass with short wave UV-light of 254 nm (UVGL-58, UVP). The glass transmitted 55% of 254 nm light. The samples polymerized in about one minute. The samples could be locally polymerized by illuminating a small spot with a mercury lamp focused by an objective lens of the microscope. To deflect the light towards the sample a no. 513824 filter cube (excitation filter BP340-380, dichromatic mirror 400, suppression filter LP 425 [129]) was used. This filter cube only transmits light in the range of 340–380 nm. Using this combination of light

source and filter cube only the 365 nm line of Hg was guided to the sample. The major absorption peak of the photoinitiator lies at 240–250 nm and it has a minor absorption around 325 nm [130]. The 365 nm line of Hg is far from these absorption peaks, but apparently the light was so intense that sufficient energy was absorbed to form radicals that initiated the polymerization reaction.

### 4.3.3 Microscopy

The 3D structure was determined before and after polymerization with a confocal scanning laser microscope (Leica type NT or SP2). The fluorescent dye was excited with the 488 nm line of the Ar laser of the confocal microscope. The coordinates of the particles were determined using algorithms similar to those of Crocker and Grier [104], but extended to 3D as described by Dassanayake *et al.* [43].

Images of the unlabeled particles were taken with a digital camera mounted on top of the microscope. Distances in these images were calibrated by comparing them with images of a calibration grid (Ted Pella, crossed micrometer scale, 1 mm in 0.01 mm divisions) taken with the same settings.

### 4.3.4 Refractive index measurements

The refractive index of the monomer was measured with an Abbe refractometer (NAR-3T, Atago Co., Japan). Variable angle spectroscopic ellipsometry was used to determine the refractive index after polymerization. For that purpose a thin layer was spun onto a silicon wafer that was coated with 3-(trimethoxysilyl)propyl acrylate. It was then polymerized by illumination with short wave UV light under a nitrogen flow. Under three angles (20°, 40° and 60°) the change in polarization, i.e. the phase shift  $\Delta$  and the amplitude change  $\Psi$ , were measured over the wavelength range of 300–1700 nm. With a surface profiler (Alpha-Step 500) the thickness of the film was roughly measured. Both the thickness and the refractive index were then fitted taking the measured thickness and the refractive index of the monomer as the starting values.

## 4.4 Results and discussion

### 4.4.1 Refractive index

Before polymerization the refractive index of ethoxylated trimethylolpropane triacrylate (ETPTA) was 1.47. Silica particles grown via a Stöber growth have a refractive index of  $n \approx 1.45$  [84]. The refractive index difference was small enough to ensure only little scattering of light and to be able to look deep into a sample with a confocal microscope.



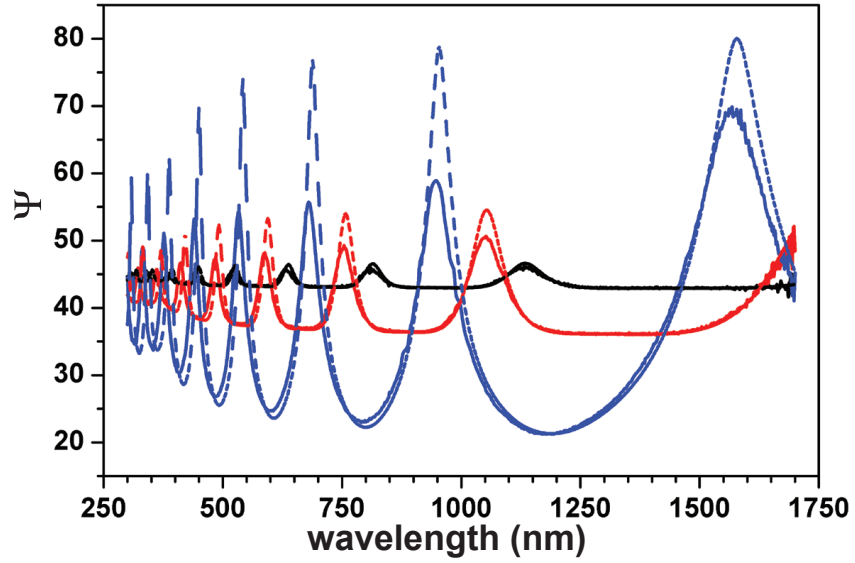


**Figure 4.2:** Spectroscopic ellipsometry revealed that the refractive index of ETPTA after polymerization is 1.49. The full lines are the amplitude change,  $\Psi$ , measured at angles of  $20^\circ$ ,  $40^\circ$  and  $60^\circ$ . The dashed lines are fits.

With spectroscopic ellipsometry the refractive index of a layer of polymerized ETPTA was determined. Figure 4.2 shows the amplitude change  $\Psi$  as a function of wavelength measured at angles of  $20^\circ$ ,  $40^\circ$  and  $60^\circ$ . A measurement with a surface profiler gave an approximate film thickness of  $1 \mu\text{m}$ . Fitting both the refractive index and the local thickness gave for this measurement a refractive index of  $1.49 \pm 0.01$  and a thickness of  $0.97 \mu\text{m} \pm 0.01$ . Also at two other positions on the sample that same refractive index was obtained. The refractive index difference between silica and the polymer is thus 0.04. Although this is a significant difference, it appeared small enough to be able to image particles in the whole film. That the medium becomes optically denser, may indicate that it contracts, but the difference is only small.

#### 4.4.2 Film thickness

Starting with an initially uniform film, the thickness,  $h$ , is theoretically expected to be inversely proportional to the spin speed and the square root of spin time:  $h \propto 1/(\omega\sqrt{t})$  [111,112]. Measurements showed that this relationship also holds for colloid dispersions. Films were spin coated from a 50-vol% dispersion of  $1.2 \mu\text{m}$  diameter silica particles in ethoxylated trimethylolpropane triacrylate. The thickness of each film was determined by taking the average of measurements at six positions with a confocal microscope. All films were first spun for 60 s at 800 rpm to cover the substrate evenly. Then, the films were spun for 30 s at various spin speeds or at 2000 rpm for different spin times. Figure 4.3 shows that the thickness,  $h$ , was proportional to  $1/\omega$  and  $1/\sqrt{t}$ .

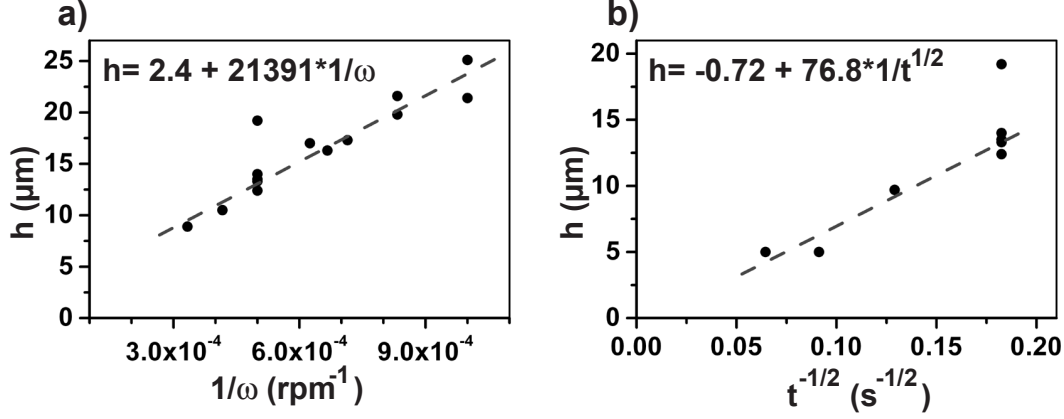


**Figure 4.3:** The thickness of films formed by spin coating a suspension of  $1.2 \mu\text{m}$  particles in ETPTA with  $\phi = 0.50$ , was determined to be inversely proportional to the spin speed,  $\omega$ . The spin time was fixed at 30 s (a). The film thickness was also found to be inversely proportional to the square root of the spin time,  $t$ . The spin speed was fixed at 2000 rpm (b). The dashed lines are fits to the data neglecting the point at  $1/\omega = 5 \times 10^{-4} \text{ rpm}^{-1}$ ,  $h = 19.2 \mu\text{m}$  in panel (a) and  $\sqrt{1/t} = 0.18 \text{ s}^{-1/2}$ ,  $h = 19.2 \mu\text{m}$  in panel (b).

From the slope of these lines we can obtain the viscosity of the dispersion via Equation 4.8. For the calculation we assume that the density of the dispersion is equal to the volume average of the density of the dispersing medium ( $\rho_m = 1.1 \times 10^3 \text{ kg/m}^3$ ) and the density of the particles ( $\rho_p = 2 \times 10^3 \text{ kg/m}^3$ ). With a particle volume fraction of  $\phi = 0.47$  (see page 63) the average density is  $\rho_{\text{average}} = 1.5 \times 10^3 \text{ kg/m}^3$ . Equating  $\sqrt{\frac{3\eta}{4\rho t}}$  to  $21391 \text{ rpm} \cdot \mu\text{m}$  with  $t = 30 \text{ s}$  gives a viscosity  $\eta = 0.301 \text{ Pa}\cdot\text{s}$ . From the graph of film thickness versus inverse square-root of time, we obtain with  $\omega = 2000 \text{ rpm}$  a viscosity  $\eta = 0.517 \text{ Pa}\cdot\text{s}$ . These two outcomes are less than a factor of 2 apart. For an estimate of the shear rate we use their average of  $\eta = 0.41 \text{ Pa}\cdot\text{s}$ . To make a film of approximately  $15 \mu\text{m}$  in thickness by spinning for 30 s, a spin speed of 1700 rpm is required. At  $0.5 \text{ cm}$  from the center the maximum shear rate, given by Equation 4.2, is  $\dot{\gamma} = 9 \text{ s}^{-1}$ . Directly after spin coating also the bottom layers, where the shear rate is at its maximum, were crystalline. According to our findings described in Chapter 3, shear induced melting occurs in this system at shear rates equal to or higher than  $2 \text{ s}^{-1}$ . Our estimated maximum shear rate during spin coating is above this boundary. The difference is, however, less than one order of magnitude.

#### 4.4.3 White light illumination

Under white light illumination the spin coated samples showed a colorful six-armed star (see Figure 4.4). Both the first order diffraction (red star) and the second order diffraction (green star) were observed. Whereas colloidal crystals

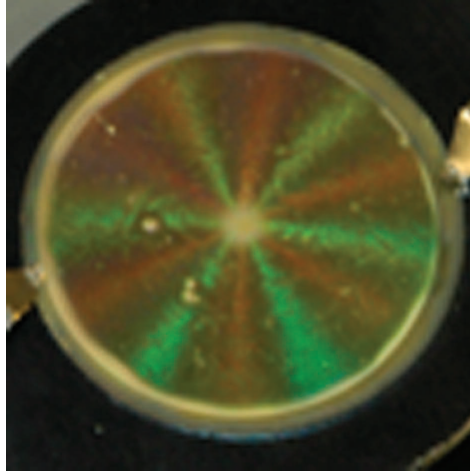


**Figure 4.4:** Under white light illumination spin coated colloidal crystalline films showed a six-armed star. This star remained during the polymerization process. The film shown had a diameter of 22 mm.

under white light illumination are usually brightly colored over the complete area, the areas between the arms of the star were not brightly colored when the angle of incidence of the light and the detection angle were fixed. This indicates that the particles order in a hexagonally symmetric lattice that changes its orientation to match the radial symmetry of the spin coating process.

Already a long time ago Hoffman [131] observed such a six-armed star for a colloidal dispersion in a cone-plate shear cell. Hexagonal layers formed in the velocity-vorticity plane with a close packed line oriented along the flow direction. More recently, Ruhl *et al.* observed a similar diffraction star when they ordered particles by melt compression between parallel plates by which hexagonal layers parallel to the substrate formed [18–20]. They ascribed the appearance of this star to diffraction from the (220)-family planes.

Another indication that the film consisted of particles arranged in hexagonal layers was a Bertrand image of a small area of such a crystal (see Figure 4.5). Not a diffuse ring, but sharp diffraction spots were observed. This indicates that the crystalline domains in the observed area of about  $150\ \mu\text{m} \times 150\ \mu\text{m}$  were all oriented in the same direction.

#### 4.4.4 3D structure determination with confocal microscopy

##### Influence of polymerization on the crystal structure

All structures formed by spin coating were in their unpolymerized state stable for at least 30 minutes, which made it possible to determine the structure before polymerization. This high stability is a direct consequence of the high viscosity of the monomer, which leads to a slow diffusion. The diffusion coefficient can be expressed by  $D = \frac{k_B T}{6\pi\eta R}$ , where  $k_B$  is the Boltzmann constant,

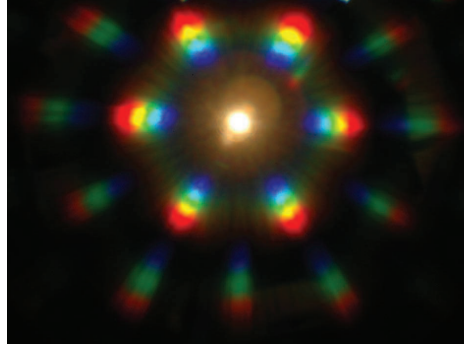


**Figure 4.5:** Bertrand image of a colloidal crystal film made by spin coating. Both the first and second order diffraction are visible.

$T$  the temperature, and  $R$  the particle radius. The monomer has a viscosity of  $\eta = 0.07$  Pa·s. The diffusion coefficient of a  $1.2 \mu\text{m}$  diameter particle at room temperature is in this medium  $D = 5.2 \times 10^{-15} \text{ m}^2 \cdot \text{s}^{-1}$ . The mean square displacement,  $\langle \Delta r^2 \rangle = 6Dt$ , of a  $1.2 \mu\text{m}$  diameter sphere in 30 minutes is in this medium only  $0.56 \mu\text{m}$ . Also sedimentation in this medium is slow. The sedimentation velocity of a sphere is:  $v = \frac{2\Delta\rho g R^2}{9\eta}$ , where  $g$  is the standard acceleration of free fall.  $\Delta\rho$  is the density difference between medium and sphere, which is in this case:  $\Delta\rho = \rho_{\text{sphere}} - \rho_{\text{medium}} = 2 \times 10^3 \text{ kg/m}^3 - 1.1 \times 10^3 \text{ kg/m}^3 = 0.9 \times 10^3 \text{ kg/m}^3$ . The sedimentation velocity of a  $1.2 \mu\text{m}$  diameter silica particle in this medium is only  $10 \text{ nm/s}$ .

Not only the refractive index of the monomer, but also that of the polymer is close enough to the refractive index of silica to be able to image particles in the whole sample. We could therefore not only determine the structure during, but also after polymerization.

It is imaginable that polymerization would lead to anisotropic shrinkage, which would change the symmetry of the crystals. However, neither local polymerization with the mercury lamp on the microscope nor polymerization of the complete sample as described in the experimental section altered the position of the particles. When the intensity of the UV lamp was, however, not attenuated by the glass container, i.e. when both the sample and the lamp were placed in a nitrogen bag, the structure became disordered during polymerization. Apparently the polymerization rate was then too high, inducing a flow in the dispersion that destroyed the crystal. Even when the crystalline film was polymerized slowly, i.e. through the glass container by which the intensity of the light was decreased, the bottom layers became disordered if the substrate was coated with 3-(trimethoxysilyl)propyl acrylate. After this finding, the substrates were only cleaned with chromosulfuric acid before use.

Because polymerization did not alter the position of the particles of spin coated films, for practical convenience all samples discussed below were polymerized before examination unless stated otherwise.

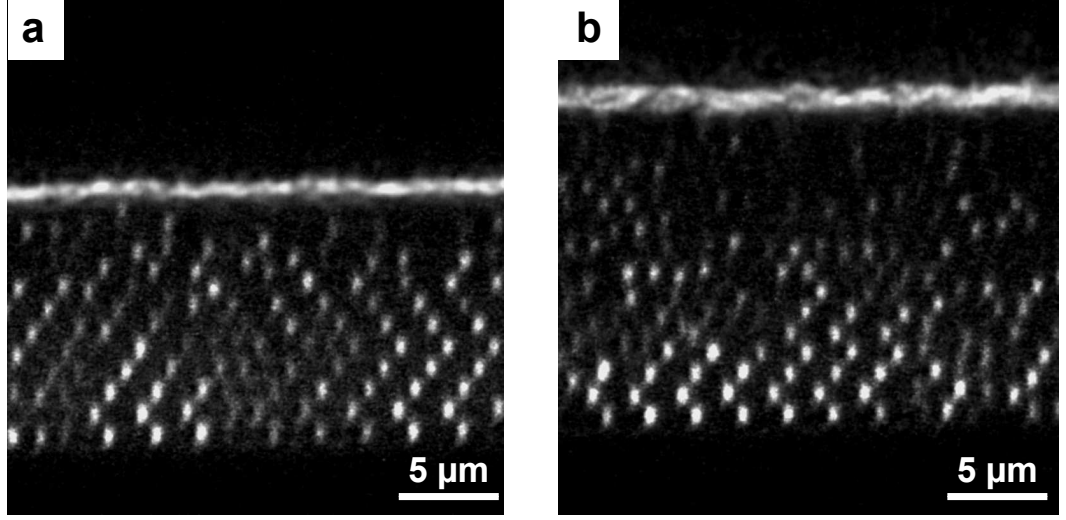


**Figure 4.6:** Cross-sections of colloidal crystalline films of  $1.2 \mu\text{m}$  diameter particles a) without and b) with a pure polymer layer on top.

### Crystal structure

The structures obtained by spin coating were always crystalline. Although in equilibrium the particles only crystallized spontaneously when their volume fraction was above  $\phi \approx 0.50$ , dispersions with an initial volume fraction as low as  $\phi = 0.18$  crystallized by spin coating! Apparently, the dispersing medium was selectively removed during spin coating, leaving the particles behind at a much higher local volume fraction.

In most films the whole film was occupied with particles, but sometimes a thin pure polymer layer without particles lay on top of the crystal. An example of a film with particles that fill the whole film and one of a film with a pure polymer layer on top are given in Figure 4.6.

We calculated the final local volume fraction by determining the number of particles in the film, multiplying this number with the known volume of one particle and dividing this through the total volume. For this determination we only used samples without a pure polymer layer on top of the crystal. To calculate the volume, the distances along the  $z$ -axis of the confocal microscope had to be corrected. The refractive index of the dispersion was lower than that of the immersion oil by which measured vertical distances became larger than the actual distances. The correction factor was calculated with a formula based on geometric optics [107]:

$$\frac{\Delta z_{\text{real}}}{\Delta z_{\text{measured}}} = \frac{n_{\text{disp}}}{n_{\text{oil}}} \sqrt{1 - \frac{1}{4} \left( \frac{L}{f} \right)^2 \left( \frac{n_{\text{oil}}}{n_{\text{disp}}} - 1 \right)}, \quad (4.9)$$

where  $\Delta z_{\text{real}}$  and  $\Delta z_{\text{measured}}$  are the real and measured distances along  $z$ .  $n_{\text{disp}}$  and  $n_{\text{oil}}$  are the refractive indices of the dispersion and the immersion oil

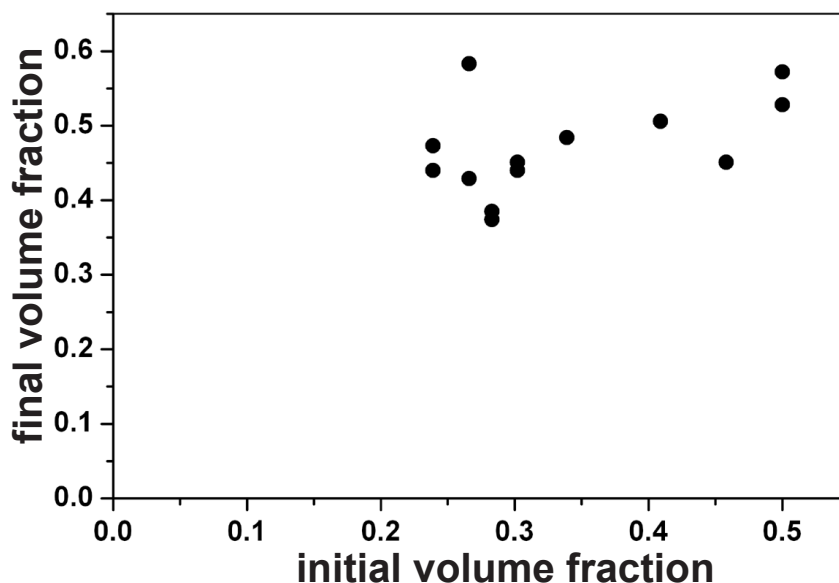


**Figure 4.7:** The volume fraction of particles in the spin coated films was higher than the initial volume fraction. The final volume fraction was independent of the initial volume fraction and always reached a value around  $\phi = 0.47$ .

respectively.  $L$  and  $f$  are the diameter and the focal length of the objective. For the objective lens we used, they were  $L = 5.6$  mm and  $f = 2$  mm. The refractive index of the dispersion was assumed to be the volume averaged refractive index of the silica particles ( $n = 1.45$ ) and the polymerized medium ( $n = 1.49$ ). So assuming that  $\phi = 0.5$  the refractive index of the dispersion,  $n_{disp}$ , was 1.47. The immersion oil (type B, Cargille) had a refractive index of  $n_{oil} = 1.515$ . The correction factor is then 0.909. Figure 4.7 shows that the final volume fraction was independent of the initial volume fraction and always reached a final value around  $\phi = 0.47$ .

In a purely gravitational field, only particles in the bottom part of a colloidal dispersion crystallize. Only at the bottom the osmotic pressure that the above lying particles exert on them, is high enough to induce crystallization. Particles at the top form a fluid layer [132, 133]. Crystals fabricated by spin coating differed from crystals formed by sedimentation: not only the bottom layers were crystalline, but also the top layer. This suggests that there is a pressure normal to the substrate that replaces the osmotic pressure present in sedimentation. As the particle positions did not change during the polymerization reaction, this pressure had to be present during the spin coating process. However, such a normal pressure is to our knowledge not theoretically described in models about spin coating of polymer solutions. It is also possible that it arises from the non-Newtonian nature of our suspensions.

Another possibility is that the formation of a crystalline film starts at the dispersion-air interface, which has been observed for silica particles in



water [134]. By surface tension forces and slow evaporation of the water a monolayer of particle formed at the water-air interface. The particles arranged in a crystalline layer. By a flow in the dispersion more particles were brought towards the surface and a 3D crystal formed. While more and more water evaporated, the surface with the 3D crystal moved downwards. When the downwards moving of the film due to evaporation is faster than sedimentation of the particles in the dispersion an even thicker 3D crystalline film forms. This might also happen during spin coating. Evaporation of the monomer that we used is slow, but due to its high viscosity sedimentation of the particles is also very slow. As calculated on page 61, the sedimentation velocity of a  $1.2 \mu\text{m}$  diameter silica particle in this medium is only  $10 \text{ nm/s}$ .

Confocal microscopy confirms the conclusion from white light illumination observations that the crystals consisted of hexagonal layers parallel to the substrate. The hexagonal layers were oriented such that a line with the highest density of particles pointed radially outwards (see Figure 4.8). This is similar to the order often seen under shear (Chapter 3), i.e. hexagonal layers in the velocity-vorticity plane with a close-packed line aligned along the flow direction.

In Reference [21] it is claimed that only face-centered cubic (FCC) crystals are formed. Domains of FCC stacked layers were found in our samples (Figure 4.9), but Figure 4.6 shows that also random stacking was found. There are different ways to quantify the stacking order. One is by calculating the overall stacking parameter  $\alpha$  [133, 135, 136]. This parameter reflects the probability of finding the particles in layer  $n - 1$  and layer  $n + 1$  at a different position than the particles in layer  $n$ . It can easily be calculated from an image of the (110)-plane of a crystal, with

$$\alpha = 1 - \frac{\kappa}{N - 2}, \quad (4.10)$$

where  $N$  is the total number of layers and  $\kappa$  the number of twinning planes as seen in Figure 4.9. For an FCC stacking  $\alpha = 1$  and for a hexagonal close packed (HCP) stacking the parameter  $\alpha = 0$ . The overall stacking parameter for crystals formed by spin coating was determined at 1–2 positions in thirteen crystals that had 5–13 layers. On average  $\alpha$  was 0.56, which indicates random stacking with a slight preference for FCC. This is different from the FCC crystals reported by Jiang and McFarland.

The stacking parameter  $\alpha$  gives an average of the whole sample. Local information about the symmetry can be obtained with the local bond order parameter [137, 138]

$$q_{lm}(i) = \frac{1}{n_c} \sum_{j=1}^{n_c} Y_{lm}(\hat{r}_{ij}), \quad (4.11)$$

where the sum is over the nearest neighbors  $j$  that are  $n_c$  in total.  $Y_{lm}$  are the spherical harmonics and  $\hat{r}_{ij}$  is the unit vector connecting particle  $i$  to  $j$ . As

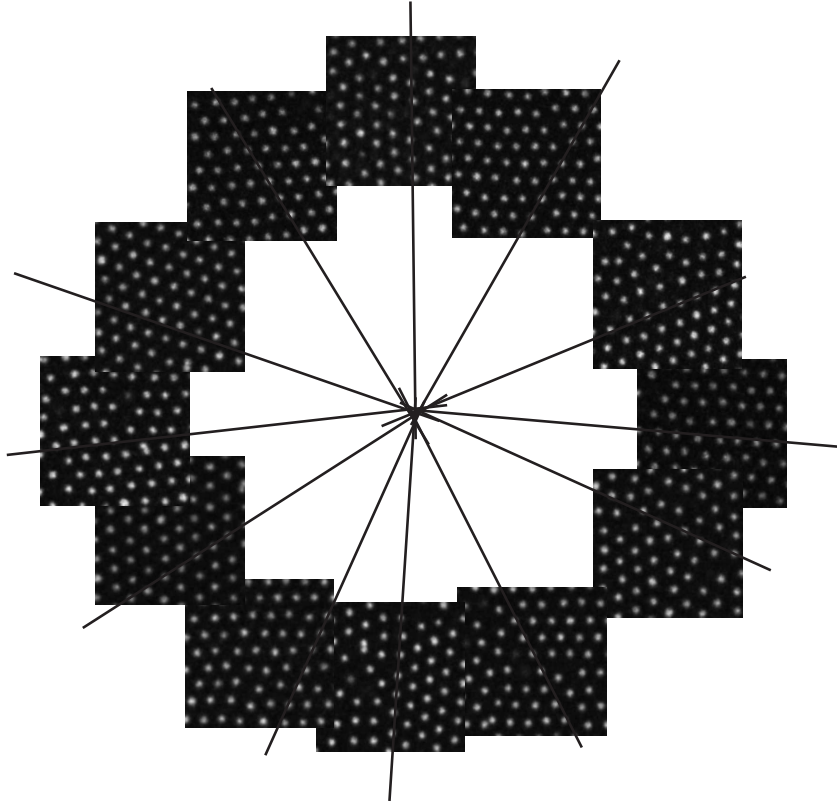


**Figure 4.8:** Confocal microscopy images of a colloidal crystalline film of  $1.2\ \mu\text{m}$  diameter particles made by spin coating, taken in a circle around the center of rotation. A line with the highest density of particles points radially outwards.

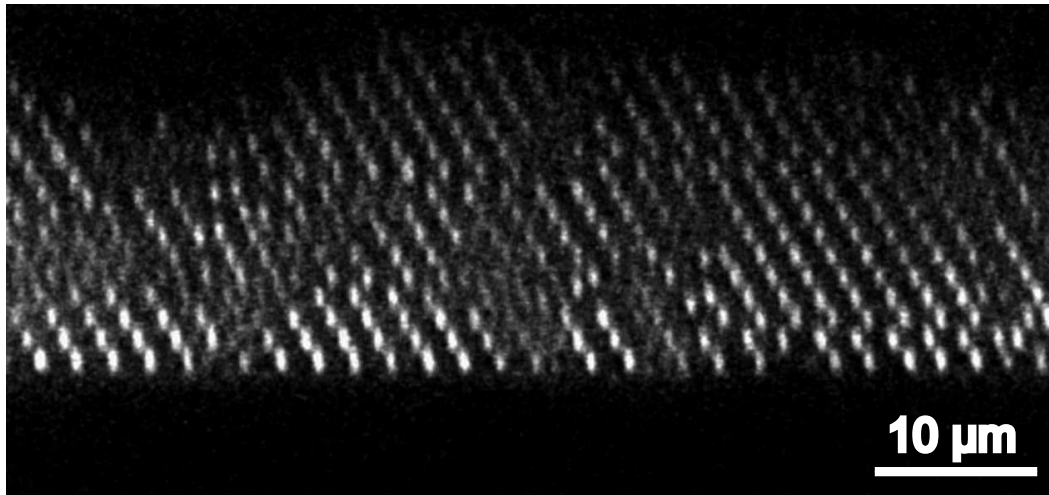


**Figure 4.9:** Cross-section of a crystal of  $1.2\ \mu\text{m}$  diameter particles fabricated by spin coating. The hexagonal layers of this film were stacked in a face-centered cubic fashion. The overall stacking parameter,  $\alpha$ , was 0.8.



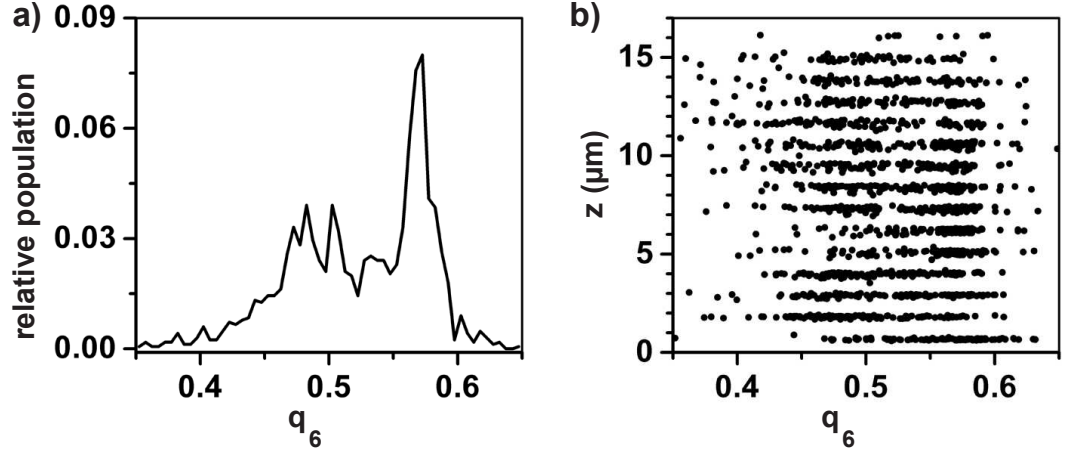


**Figure 4.10:** The values of  $q_6$  and thus the symmetry around the particles could be categorized into two groups: around the HCP value of  $q_6 = 0.485$  and around  $q_6 = 0.575$  for FCC. a) A plot of  $q_6$  as a function of height showing that the first few layers were more HCP-like than the above lying layers. b) The area under the peak from 0.55-0.60 for FCC was 1.4 times larger than the area under the peak from 0.46-0.51 for HCP.

$q_{lm}$  depends on the reference frame, it is convenient to use it in its rotationally invariant form:

$$q_l(i) = \left( \frac{4\pi}{2l+1} \sum_{m=-l}^l |q_{lm}(i)|^2 \right)^{1/2}. \quad (4.12)$$

We consider  $q_6$ , so for  $l = 6$ , which discriminates between FCC and HCP. This bond order parameter measures the degree to which the bonds between a particle and its twelve nearest neighbors make angles of  $60^\circ$ . For FCC  $q_6 = 0.575$  and for HCP  $q_6 = 0.485$  [137, 138]. The histogram in Figure 4.10a shows that  $q_6$  tends to cluster around the value for HCP or for FCC, but the surface area under the peak around 0.575 is 1.4 times larger than that under the peak around 0.485 indicating a tendency to an FCC stacking. The plot of the values of the individual particles shows that HCP stacked particles are mainly found at the bottom of the sample (Figure 4.10b). Before, Hoogenboom *et al.* observed that also colloidal crystals grown by sedimentation have more HCP stacked layers at the bottom than higher in the crystal [133]. By analyzing the crystallization process during sedimentation, they found that the osmotic pressure that makes the particles crystallize, was higher for the first layer than for successive layers. This decreased the equilibration time for the first few layers and increased the occurrence of HCP stacked layers, although an HCP structure is slightly higher in energy than FCC stacked layers [139–141]. More research needs to be done to find out whether a more frequent occurrence of HCP stacking at the bottom wall in spin coated crystals is related to its occurrence in crystals grown by sedimentation.

Some samples also contained many crystallites that were oriented with

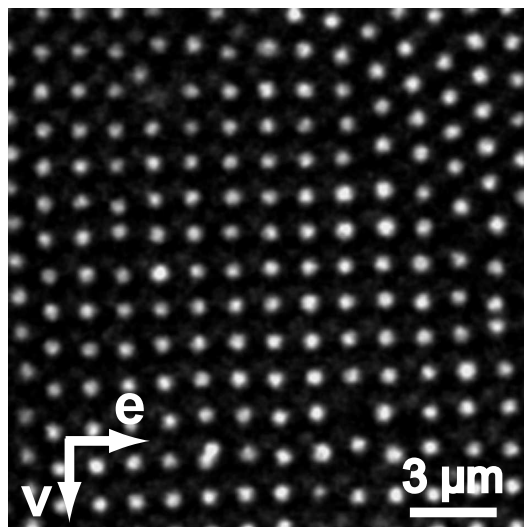


**Figure 4.11:** Confocal micrograph of a crystalline domain oriented with its (100) plane in the velocity-vorticity plane.

the (100) plane parallel to the substrate. These differently oriented domains were of the order of  $20\ \mu\text{m} \times 20\ \mu\text{m}$ . Figure 4.11 is a confocal microscopy image of such a sample. Mihi *et al.* [121] fabricated colloidal crystals by spin coating silica or polystyrene dispersed in a mixture of ethanol, distilled water and ethylene glycol. They also obtained domains oriented with the (100) plane parallel to the substrate. When they dispersed the particles in pure ethanol and finely tuned the experimental conditions, they were able to force the domains to orient only with a (111) or (100) plane parallel to the substrate. However, they did not specify these conditions nor did they give an explanation for it [121]. We suggest that the orientation depends on the exact thickness of the film. Experiments [142–146] and theoretical calculations [147] have shown that colloidal dispersions confined in a wedged cell form crystals with such an orientation that the packing density is maximized. Depending on the exact thickness of the sample square or triangular symmetric structures are found parallel to the substrate.

### Crystalline patches

In several other samples the particles formed crystalline patches with only pure monomer in between. The patches consisted of hexagonal layers parallel to the substrate. Figure 4.12 shows such patches. Note, that the edges of these patches are sharp. The particles formed isolated crystalline domains not only when the initial volume fraction was low (Figure 4.12a), but sometimes even when the initial volume fraction was as high as  $\phi = 0.46$  (Figure 4.12b). The volume in between the patches was smaller when the initial particle volume fraction of the dispersion was higher. Our first guess was that

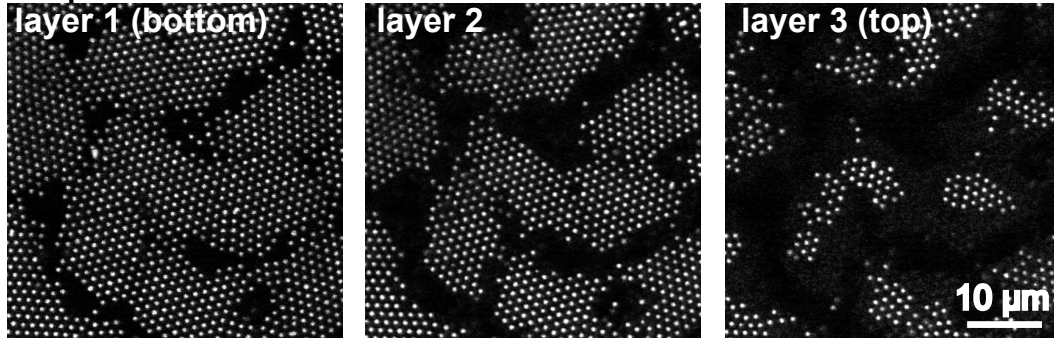
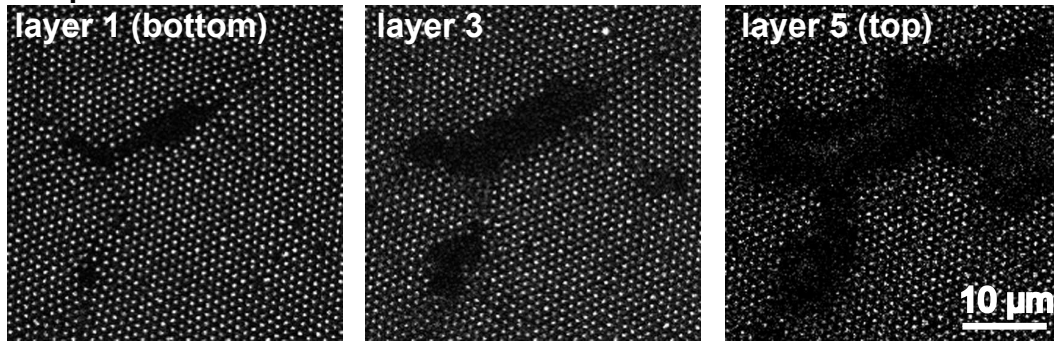
the formation of these patches was caused by problems with the wetting of the substrate. The wetting could be changed by pretreatment of the substrate. The contact angle of ETPTA in air on an uncleaned glass slide was  $40^\circ$ . When the substrate was cleaned with ethanol or chromosulfuric acid the contact angle decreased to  $25^\circ$ . A droplet of ETPTA on a substrate coated with 3-(trimethoxysilyl)propyl acrylate had a contact angle of only  $10^\circ$ . We prepared samples on these differently pretreated substrates. If wetting would be the cause of patch formation, the particles would not form patches on the cleaned or coated substrates. However, we did not only observe patches on substrates cleaned with chromosulfuric acid or ethanol, but also on substrates coated with 3-(trimethoxysilyl)propyl acrylate. Moreover, the observation that there was monomer between the patches contradicts the hypothesis that patch formation is caused by a poor wetting.

Even when the medium was not polymerized, the crystalline patches were stable for more than 30 minutes. As explained above, this high stability is due to the high viscosity of the medium. However, why these isolated domains formed in the first place is as yet unclear. It might be that films form at the air-interface as described on the pages 63–64 and in Ref. [134] and that they break up into smaller crystals under certain conditions. This would explain the sharp edges of the patches. The patches were broader at the bottom than at the top. This can be explained by a flow that destroyed the patches after they had sedimented and that removed particles from the patches, especially from the top part. More research is needed to reveal the mechanism of patch formation.

### Hexagonal layers of touching and non-touching particles

Jiang *et al.* [21] obtained with spin coating only colloidal crystalline structures in which the particles in the hexagonal layers were separated by  $1.4D$ , where  $D$  is the particle diameter. The particles within the hexagonal layer parallel to the substrate were non-touching. The particles touched particles of the layer above or below it though.

In our experiments the particles were practically touching each other. The nearest-neighbor distance measured in the hexagonal plane was  $1.1D$ . The separation between the layers was 0.8 times the in-plane nearest-neighbor distance; the particles formed an FCC-like structure with a lattice constant 1.1 times the physical diameter of the particles. Although all Jiang's images were of 325 nm diameter particles, they claimed that even silica particles with a diameter as large as  $2\text{ }\mu\text{m}$  formed structures of hexagonal layers of non-touching particles by spin coating. An in-plane nearest-neighbor distance of  $1.4D$ , which is very close to  $\sqrt{2}D$ , suggests that the crystal structure is simple cubic instead of face centered cubic-like. It would be very useful to have control over the packing. We also tried to make structures with such large interparticle spacings. Although the size should not matter, we took smaller particles with a diameter

a)  $\phi_i = 0.19$ b)  $\phi_i = 0.46$ 

**Figure 4.12:** Confocal microscopy images showing crystalline patches of  $1.2 \mu\text{m}$  diameter particles ordered in hexagonal layers. In panel (a) the initial volume fraction was  $\phi = 0.19$ . The initial volume fraction of the dispersion in panel (b) was much higher:  $\phi = 0.46$ .

of  $0.4 \mu\text{m}$  and  $0.79 \mu\text{m}$  diameter and repeated the experiments.

The  $0.4 \mu\text{m}$  diameter particles were not fluorescently labeled and too small to image individually with confocal microscopy. Therefore, we examined the crystals with conventional microscopy. Images were taken with a digital camera coupled to the microscope and distances in them were calibrated with a calibration grid. The in-plane nearest-neighbor distance of the particles with monomer or polymer in between was  $0.53 \mu\text{m} = 1.44D$ . Scanning electron microscopy (SEM) would be a good method to examine the structure of crystals formed with these small particles. However, it could not be used, because the polymer melts in the electron beam. In Chapter 5, we will describe how the polymer could be removed after which we were able to examine the crystals with SEM.

In our experiments, the  $0.4 \mu\text{m}$  diameter particles formed only non-touching structures and up to this moment the  $1.2 \mu\text{m}$  particles formed only structures in which the particles were touching each other. Particles with a diameter of



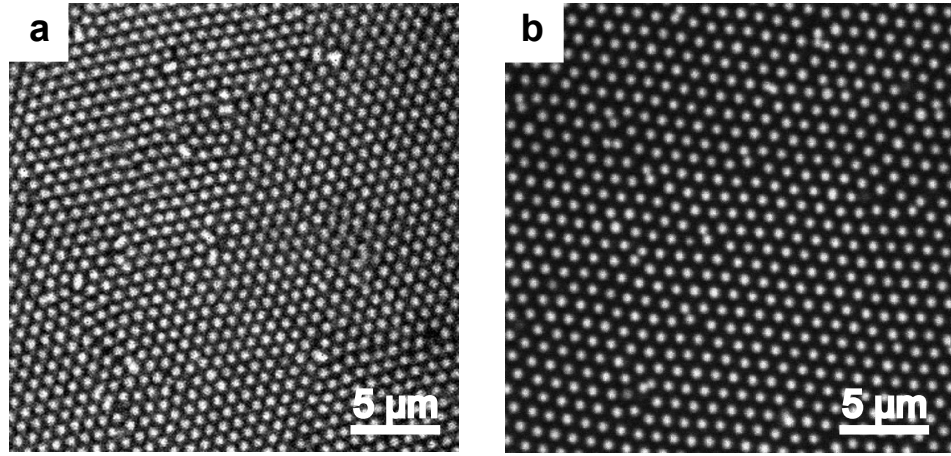


**Figure 4.13:** During spin coating  $0.79\ \mu\text{m}$  diameter silica particles in ETPTA formed both structures consisting of hexagonal layer of touching (a) and of non-touching (b) particles.

$0.79\ \mu\text{m}$  seemed to be in a transition region: they sometimes formed touching structures and sometimes non-touching structures, with interparticle distances of  $0.94\ \mu\text{m} = 1.2D$  and  $1.06\ \mu\text{m} = 1.4D$  respectively (see Figure 4.13). These observations suggest that the particle size is one of the parameters that determined whether the structures consisted of hexagonal layers of touching or of non-touching particles. To find the additional cause(s) we varied several other parameters of the spin coating procedure.

Experiments with various spin times, spin speeds, initial volume fractions or pretreatments of the substrate showed that these parameters did not influence the nearest-neighbor distance of  $1.2\ \mu\text{m}$  diameter particles in spin coated films. In all cases, crystals of nearly touching particles were formed. We performed similar experiments with  $0.79\ \mu\text{m}$  diameter particles that in previous experiments sometimes formed crystals of non-touching particles. These new experiments showed that spin time, spin speed, initial volume fraction or pretreatment of the substrate did not influence the nearest-neighbor distance of these  $0.79\ \mu\text{m}$  diameter particles either.

To check whether the substrate size influences the final structure, a 80 mm diameter glass slide was used. The volume of the dispersion was increased accordingly from  $20\ \mu\text{l}$  to 0.6 ml. There was no significant difference in nearest-neighbor distance or overall crystallinity. It is known that the central few centimeters of a film formed by spin coating is less uniform than the area further away from the center [148]. However, we did not observe this. The crystallinity was similar over the whole radial distance. Because of practical considerations, i.e. compatibility with the microscope and an economic usage of dispersions, we kept using 22 mm diameter substrates.

Most of the ethanol in which the particles were stored was removed by cen-

trifuging the dispersion once and subsequently removing the supernatant with a pipet. The last traces were removed by allowing the ethanol to evaporate. Vials were kept open for one day. Weighing showed that the dispersions after evaporation typically contained a few tens of  $\mu\text{l}$  of ethanol, corresponding to approximately 5 vol%. Of course, this concentration was not exactly the same for all dispersions. During spin coating these traces of ethanol most probably evaporate. However, varying the ethanol content on purpose showed that this difference did not significantly influence the interparticle spacing after spin coating.

In all above mentioned experiments the spacing between the particles seemed to be fixed for every vial. This raised the suspicion that the interparticle spacing was determined by a subtle difference in the composition of the dispersion. Minor contaminations can change the ionic strength, which determines the range over which particles interact. To test whether the interparticle spacing in spin coated samples is determined by the ionic strength, we intentionally varied the ionic strength.

The ionic strength and thus the conductivity of the monomer was changed by deionization or by the addition of salt. As received the monomer from Aldrich had a conductivity of  $\sigma = 2.6 \times 10^3$  pS/cm. After one week of deionization by mixing it with ion exchange resin, the conductivity decreased by one order of magnitude to  $\sigma = 0.26 \times 10^3$  pS/cm. Also when the monomer was deionized by mixing it with glycerol, its conductivity decreased by one order of magnitude. Such a decrease in ionic strength extends the thickness of electronic double layer that surrounds the colloids. Quantitatively, the relationship between the conductivity,  $\sigma$ , and the Debye screening length,  $\kappa^{-1}$ , can be calculated as described below.

The conductivity is related to the ionic concentration via the limiting molar conductance as:

$$\sigma = 10^9 c \Lambda^0, \quad (4.13)$$

with  $\sigma$  = conductivity in pS/cm,  $c$  = ionic concentration in mol/l,  $\Lambda^0$  = limiting molar conductance in  $\text{cm}^2 \cdot \text{S/mol}$ . The limiting molar conductance for ETPTA can be calculated using Walden's rule:

$$\Lambda_{\text{water}} \eta_{\text{water}} = \Lambda_{\text{ETPTA}} \eta_{\text{ETPTA}}, \quad (4.14)$$

with  $\eta$  = viscosity in Pa·s. The viscosity of the monomer is 0.07 Pa·s, i.e.  $70 \times$  as viscous as water. With  $\Lambda_{\text{Na/water}} = 50 \text{ cm}^2 \cdot \text{S/mol}$  [149], the limiting molar conductance of ETPTA is  $\Lambda_{\text{ETPTA}} = 0.71 \text{ cm}^2 \cdot \text{S/mol}$ .

The dielectric constant of the monomer is approximately 3 [23], which is comparable to other acrylates. With this information the inverse Debye screening length can be calculated using:

$$\kappa = \left( \frac{e^2 \sum z_i^2 n_i}{\epsilon \epsilon_0 k_B T} \right)^{1/2}, \quad (4.15)$$

where  $e$  is the elementary charge,  $z_i$  is the valency of the ions - we assume that only monovalent ions are present -  $n_i$  is the ionic concentration in  $\text{molecules}\cdot\text{m}^{-3}$ ,  $\epsilon$  is the dielectric constant,  $\epsilon_0$  the vacuum permittivity,  $k_B$  the Boltzmann constant and  $T$  the temperature.

This derivation shows that decreasing the conductivity with one order of magnitude to  $\sigma = 0.26 \times 10^3$  pS/cm corresponds to an increase of the Debye screening length,  $\kappa^{-1}$ , by a factor of three (see Table 4.1).

In a system with ETPTA deionized with ion exchange resin, the distance between the  $1.2 \mu\text{m}$  diameter particles was not different from that of an undeionized system. This despite that the dimensionless screening length,  $\kappa R$ , should now be very similar to that of the  $0.4 \mu\text{m}$  particles in the undeionized system. And that system formed structures of non-touching particles.

When ETPTA was first deionized with glycerol and was then added to silica particles, the particles aggregated. The particles within the aggregates still showed Brownian motion and vibrated. This indicates that the particles had not drawn that close to each other that they resided in the primary minimum of the potential, but that their aggregation had some other cause. The presence of glycerol might have induced the formation of small polymer chains. These polymer chains may cause aggregation via depletion interactions. A second possibility is that by decreasing the ionic strength of the medium, the double layer was extended so much that the interaction energy potential curve not only exhibited a primary minimum, but also a secondary minimum. The particles could have aggregated into this secondary minimum.

Removing ammonia and water from the particles by heating them in the oven did not influence the spacing between the particles either. After adding 1 mM LiCl the system was still stable. The particles did, however, no longer crystallize, neither after allowing it to sediment for a week nor by spin coating.

Changing the ionic strength by deionization or by the addition of salt did not provide a clue about the origin of the different interparticle distances found. Still, the difference in interparticle spacing might be caused by differences in the dispersing medium. It is possible that impurities or additives were present in the monomer or that the dispersing medium had a variable composition. Remember that the medium is in principle a monomer, but there might already be a certain degree of prepolymerization. Furthermore, the monomer is ethoxylated, the number of ethoxide groups might vary from batch to batch.

To test whether such minor differences in solvent composition made the difference, we ordered a second bottle of ethoxylated trimethylolpropane triacrylate from Aldrich. It was from a different batch. Sartomer also kindly provided us with a bottle. Both Aldrich and Sartomer claim an average molecular weight of 428. There is no indication given of the weight distribution. A molecular weight of 428 would correspond to one ethoxide group per molecule, i.e. only one of the three methylolpropane acrylate chains is ethoxylated. A higher degree of ethoxylation would increase the polarity of the medium.

**Table 4.1:** Conductivities, ion concentration and screening length of the monomer ethoxylated trimethylolpropane triacrylate before and after deionization.

	as received			deionized		
	$\sigma$	$c$	$\kappa^{-1}$	$\sigma$	$c$	$\kappa^{-1}$
supplier	(pS/cm)	(mol/l)	(nm)	(pS/cm)	(mol/l)	(nm)
Aldrich	$2.6 \times 10^3$	$3.6 \times 10^{-6}$	44	250	$0.35 \times 10^{-6}$	142
Sartomer	$4.4 \times 10^3$	$6.2 \times 10^{-6}$	34	465	$0.65 \times 10^{-6}$	104

The two batches obtained from Aldrich had the same conductivity. The conductivity of the batch from Sartomer was as received slightly higher (see Table 4.1). The difference in conductivity between the batches from the two suppliers was less than a factor 2. There was no significant difference in inter-particle spacing between samples made from dispersions containing monomer from the first batch of monomer obtained from Aldrich and the batch from Sartomer.

However, samples made with the second batch from Aldrich were different from the other ones. Six dispersions were made using this new batch: three with the  $0.79 \mu\text{m}$  diameter and three with the  $1.2 \mu\text{m}$  diameter silica particles. All dispersions gave rise to structures with non-touching particles. Structures with non-touching particles were earlier found for the  $0.79 \mu\text{m}$  diameter particles, but only now, also for the  $1.2 \mu\text{m}$  diameter particles (Figure 4.14). In-plane the nearest-neighbor distance of the  $1.2 \mu\text{m}$  diameter particles was  $1.68 \mu\text{m} = 1.4D$ . Because the  $1.2 \mu\text{m}$  diameter particles were large enough to be able to determine their position in  $z$ , we could also determine the distance between the layers. This layer separation was  $1.35 \mu\text{m}$  after correction for the refractive index mismatch between the immersion oil and the sample. The ratio between the layer separation and the nearest-neighbor distance was 0.8. This indicates that the particles were positioned on an FCC-like lattice of particles with a diameter of  $1.68 \mu\text{m}$ . In these samples the particles behaved as if they had an effective diameter of 1.4 times their physical diameter. Also the crystals of which the particles in a hexagonal layer were non-touching, were FCC-like and thus close-packed. This is different from the non-close packed structures that Jiang and McFarland found [21].

Despite our mapping a large section of the parameter space, the origin of the different spacings is yet unclear. We now suspect that it is a very subtle combination of surface charge and the ionic strength of the medium. This would explain why smaller particles more often formed structures consisting of non-touching particles. To obtain the same  $\kappa R$  for large particles as for



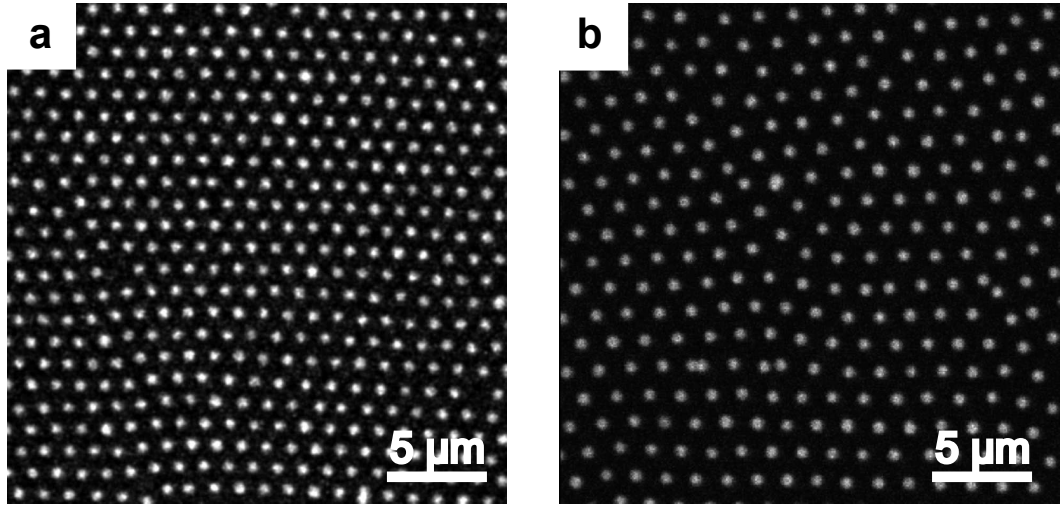


**Figure 4.14:** Dispersed in the first batch of ETPTA obtained from Aldrich or the batch obtained from Sartomer,  $1.2\ \mu\text{m}$  diameter silica particles formed crystals of touching particles (a). Dispersed in the second batch obtained from Aldrich, the same particles formed crystals in which the particles were non-touching (b).

small particles, the ionic strength has to be decreased. Only then, a relatively large in-plane interparticle distance is expected. However, it remains unclear why deionization did not influence the distance between the particles after spin coating or why a different batch with the same conductivity gave rise to a larger interparticle distance.

## 4.5 Conclusion

By spin coating we fabricated colloidal crystals of silica particles in a size range from  $0.4\ \mu\text{m}$  to  $1.2\ \mu\text{m}$ . They were dispersed in ethoxylated trimethylolpropane triacrylate that could be polymerized by illumination with UV light, making the structure permanent. Just as theoretically predicted for polymer films, the thickness of the colloidal crystals was inversely proportional to  $\omega t^{1/2}$ , where  $\omega$  is the spin speed and  $t$  the spin time.

Sometimes, a pure polymer film lay on top of the particles, but the structures were crystalline all the way to the top of the crystals. The crystals mainly consisted of hexagonal layers parallel to the substrate with a close-packed line pointing radially outwards. This orientation is induced by the flow. In some cases the crystals were rotated such that the (100) plane was parallel to the substrate, which might depend on the exact thickness of the film. Sometimes crystalline patches surrounded by pure polymer were observed. These patches were stable for more than 30 minutes. Both the observation that the top layer of particles was crystalline and the sharp edges of the formed patches suggest that the films start to form at the air-interface. By a slow evaporation of the

solvent the initially 2D layer moves downwards and grows into a 3D crystal, which break into pieces in some cases, leading to the formation of patches.

Especially the crystals consisting of the smaller particles were non-touching. Instead of  $1.1D$ , where  $D$  is the particle diameter, the nearest-neighbor distance was as large as  $1.4D$ , similar to the nearest-neighbor distance in simple cubic structures. The distance between the layers increased by the same factor. We can therefore conclude that the particles in the polymer matrix did not form a simple cubic structure, but close-packed FCC-like structures, with a lattice constant in the range of 1.1 to 1.4 times the particle's physical radius. This explains why the in-plane nearest-neighbor distance did not depend on the spin time, spin speed, initial volume fraction, substrate pretreatment or substrate size. Measurements suggested that this difference in interparticle spacing was caused by a subtle interplay between the surface charge of the particles and the ionic strength of the medium.

## Acknowledgements

We would like to thank the following persons: Joan Penninkhof for her help with the ellipsometry measurements, Roel Dullens for his assistance with the analysis of the local symmetry via  $q_6$ , Mirjam Leunissen for helping with the interpretation of the conductivity measurements and Job Thijssen for stimulating discussions. Christina Graf is acknowledged for synthesizing the  $0.4\text{ }\mu\text{m}$  diameter silica particles and Dannis 't Hart for synthesizing the  $0.79\text{ }\mu\text{m}$  diameter silica particles.



## Freestanding films of colloidal crystals

### Abstract

We prepared freestanding colloidal crystalline films of silica particles. The particles were made to order by spin coating a colloidal dispersion onto a substrate. The polymerized matrix was so elastic that it could be removed from the substrate without damage. From these freestanding films either the polymer matrix or the silica particles were removed. Removing the polymer matrix was done by heating or by plasma etching. A freestanding crystalline films of silica particles in air was then obtained. Alternatively, inverted crystals of air-spheres in a polymer matrix were made by wet etching with an HF solution or by plasma etching. In all cases the structures stayed crystalline and no cracks formed. Only the top layer of a colloidal crystalline film of non-touching particles (see Chapter 4) could be observed in SEM. Therefore, optical measurements were done. A freestanding film of crystalline  $0.79\text{ }\mu\text{m}$  diameter silica particles in air that did not touch particles in the same hexagonal layer, showed a dip in a transmission spectrum. The wavelength of this dip corresponded to the wavelength at which a Bragg diffraction peak was expected to appear in case the hexagonal layers are touching each other. However, before removal of the polymer matrix the particles in neighboring layers were not touching each other. The symmetry of the structure had, thus, changed. A change of symmetry was, however, not observed for a crystalline film of non-touching  $1.2\text{ }\mu\text{m}$  diameter particles. Freestanding films of silica particles could be deformed when they were irradiated with MeV high-energy ion beams. Despite the stress formed during irradiation, no cracks formed contrary to what was observed for crystalline films on a substrate before.

## 5.1 Introduction

A major drive for research on colloidal crystals is the fabrication of photonic crystals. Photonic crystals [150–152] have a periodically varying dielectric constant, which can for instance be realized by the self-organization of colloidal particles inside a matrix with a different dielectric constant. If the dielectric contrast between the constituents of a colloidal crystal and its surroundings is sufficiently high and if its symmetry is correct, it can have a photonic band gap (PBG). Photons of this frequency range cannot propagate inside the crystal. Photonic crystals have many applications for example as filters, optical switches and low-threshold lasers [6].

In literature, various methods to make colloidal crystals have been described, e.g. sedimentation [133], controlled drying [153], shear flow [9–11], physical confinement [12], colloidal epitaxy [154] and spin coating [21, 155]. Unfortunately, during many processes cracks form due to the shrinkage of the particles during drying. Cracks typically occur every  $50\text{--}300\text{ }\mu\text{m}$  [153, 156, 157], depending on the exact conditions. Just like other defects, cracks suppress possible band gaps and their formation should therefore be avoided. This can be done e.g. by sintering the particles before fabrication of the crystal [158]. By heating them up to  $950^\circ\text{C}$ , the particles can be preshrunk on the order of 10% in volume [159]. Recently, Pan *et al.* [160] described a method to make large defect free monolayers of polystyrene particles on flat surfaces. The technique involved two steps. First, polystyrene particles are assembled in a monolayer at a water-air surface after being driven to the surface by an induced flow of the water. After removing the superfluous particles in the water phase, a substrate was inserted vertically in the water. When the substrate was slowly withdrawn from the solution, on both sides a close-packed crystalline film formed. Reculusa *et al.* [161, 162] showed a method to make 3D colloidal crystals with a controlled thickness via the Langmuir-Blodgett technique. Functionalized silica particles in the diameter range from 220 to 1100 nm were spread over the water surface of a Langmuir trough. After compression of the layer of particles on the water-air interface, a hydrophilic glass slide or silicon wafer was immersed in the liquid. The substrate was then pulled up at such a speed that one layer of particles was deposited on it. Up to 25 layers could be deposited sequentially. These are methods to make nearly perfect crystals on a substrate. However, the presence of the substrate is a disadvantage for some further treatments.

It is known that face centered cubic (FCC) crystals of high index spheres do not have a PBG because of its symmetry [163, 164]. The symmetry can be broken by using particles that are anisotropic in shape or in dielectric constant [165]. Particles that can be made in large quantities and that are monodisperse enough to crystallize, usually are spherical. It has been shown that inorganic particles can be deformed by irradiation with a high-energy ion

beam [166, 167]. However, Velikov *et al.* [168] observed that when a colloidal crystal of silica particles supported by a substrate is irradiated with a high-energy ion beam, cracks form parallel to the direction of irradiation due to stresses that build up by shrinkage of the film while it is attached to the substrate. It is anticipated that in freestanding colloidal crystalline films stress will not form, because they can shrink freely [169].

Making freestanding colloidal crystalline films is, however, not trivial. Few methods to fabricate them have been reported. Li *et al.* [134] made freestanding films of silica particles at a water-air interface. A beaker with a dispersion of silica particles in water, covered by a large glass container, was heated on a heating plate. This established a temperature gradient that induced flow of the particles. Particles that came in contact with the water-air interface were kept there by surface tension forces together with evaporation. Capillary forces and electrostatic interactions between the particles then made them arrange in 2D monolayers and later in 3D multilayers. Gu *et al.* [170] formed freestanding films by dipping a 1 cm diameter copper ring in a dispersion of polystyrene particles and subsequently dried it at ambient temperature. At the center of the film, the crystals consisted of 3 to 6 layers. They used a second method to make freestanding films. Drops of a 50-vol% dispersion were placed on a hydrophobic substrate. At the air-water-air interface of the thus formed hemispherical bubbles crack-free colloidal crystals formed after drying.

In this chapter we will describe an additional method to make freestanding films of colloidal crystals. First, a film is made by spin coating a drop of silica particles in a viscous liquid consisting of a monomer and a photoinitiator. The matrix of the particles can then be fixed by UV illumination (see Chapter 4). It is then so elastic and strong that it can be lifted off the substrate. The matrix can be removed without destruction of the order. We will show our first results of ion irradiation experiments of such freestanding films in which no crack formation occurs. Furthermore, preliminary experiments are described in which not the matrix but the particles are removed without destruction of the order.

## 5.2 Experimental details

### 5.2.1 Making freestanding films

To make freestanding films of silica colloids arranged in a crystalline structure fixed in a polymer matrix we did the following. First, we spin coated a film of micron-sized silica particles dispersed in ethoxylated trimethylolpropane triacrylate (ETPTA, Aldrich). We used silica particles of two different sizes: 1) 0.79  $\mu\text{m}$  diameter particles of which a 0.4  $\mu\text{m}$  diameter core was fluorescently labeled with fluorescein isothiocyanate (FITC) and 2) 1.2  $\mu\text{m}$  diameter silica particles of which a 0.4  $\mu\text{m}$  diameter core was also labeled with FITC.

The particles were synthesized by the Stöber method [83]. The fluorescent dye was incorporated by the method described in Reference [84].

In Chapter 4 we described in detail the formation of colloidal crystalline films by spin coating [21]. We used a P6700 spin coater of Specialty Coating Systems. A 15–20  $\mu\text{l}$  dispersion was spread on a 22 mm diameter circular microscopy slide. Next, this substrate was rotated at a low speed of 200–800 rpm for 1–2 minutes to spread the dispersion more or less homogeneously over the substrate. Then, it was rotated at 1000–4000 rpm for a few minutes to reach the desired film thickness that can be set by choosing the correct spin speeds and spin times. Crystalline films were obtained from dispersions with particle volume fractions in the range from  $\phi = 0.20$  to 0.50.

To the dispersion 1 wt% of the photoinitiator 2-hydroxy-2-methyl-propiophenone (Darocur 1173, 97%, Aldrich) was added. This allowed us to fix the structure by illuminating the film with UV light that initiated the radical polymerization reaction. UV illumination was done after placing the sample in a glass sample chamber that was filled with nitrogen. The nitrogen was needed to keep the concentration of radicals high enough. The UV lamp (UVGL-58, UVP), used in the short wave UV light setting emitting 254 nm light, was positioned outside this sample chamber. The light was attenuated by the glass container before it reached the sample. Only 55% of the 254 nm light was transmitted by the glass. Decreasing the light intensity was necessary to prevent a too high intensity that would cause a too high polymerization rate and a flow that would destroy the structure of the particles. The matrix was completely polymerized after a few minutes.

In the outer 1–2 mm ring of a spin coated sample, the particles were in general not ordered. This ring could easily be cut away with a sharp scalpel. With a razor blade the remaining film was then carefully detached from the substrate.

### 5.2.2 Selective removal of the polymer matrix

To increase the refractive index contrast between the colloids and the matrix of such a freestanding film the polymer was selectively removed. This was done by heating the sample placed in an alumina crucible in a temperature controlled oven. The temperature was increased at a maximum rate of  $1^\circ\text{C}/\text{s}$  to  $500^\circ\text{C}$ , kept at that temperature for 3 hours, and decreased to room temperature at a maximum cooling rate of  $1^\circ\text{C}/\text{s}$ . Heating and cooling was done at such low rates to prevent the structure to shrink unevenly, which can cause the formation of cracks in the crystal.

Alternatively, removing the polymer matrix was also done by plasma etching with an oxygen plasma. We used a Plasmalab 80+ ICP plasma etcher (Oxford Instruments), a reactive ion etching (RIE) plasma etcher.

### 5.2.3 Selective removal of the silica particles

To obtain an inverted crystal of air spheres in a polymer matrix, the silica particles were etched. Two methods were used. One was immersing the free-standing film for about 10 minutes in an aqueous HF solution with a concentration of 8 wt%. The second method was by plasma etching (Plasmalab 80+ ICP, Oxford Instruments). The plasma was a mixture of CHF<sub>3</sub> and Ar. The flow rate of both gases was 25 sccm. The etch time was 14 minutes.

### 5.2.4 Spectroscopy

Transmission spectra were taken with a Fourier transform infra-red (FT-IR) spectrometer (Vertex 70, Bruker). A Hyperion 2000 microscope (Bruker) was coupled to the spectrometer to be able to select a specific area of the sample. We measured in the spectral range from 10000 to 4000 cm<sup>-1</sup>. The source was a tungsten lamp. We used a mercury-cadmium-telluride (MCT) detector to detect the transmitted light. As a background signal, we first measured a transmission spectrum of a 1 mm objective glass (Menzel). Next, the sample was placed on this glass slide. We then selected a desired part of the sample with the microscope and measured a transmission spectrum.

### 5.2.5 Ion beam deformation

Freestanding films of crystallized silica colloids in air were irradiated with an ion beam to deform the particles. We used 30 MeV Si<sup>5+</sup> ions [171]. The fluence was  $5 \times 10^{14}$  ions/cm<sup>2</sup>. During irradiation the temperature was kept at 90 K.

The scanned ion beam ran horizontally. The sample holder was placed vertically perpendicular to the direction of the ion beam. One edge of the freestanding films was attached to a silicon substrate with an electrically conductive adhesive (Loctite 3880). The surface of the film was thus perpendicular the direction of the beam, but locally the orientation could have been slightly different because of slight curling ( $< 10^\circ$ ) of the samples.

## 5.3 Results and discussion

### 5.3.1 Freestanding films

To obtain a freestanding film of crystallized silica colloids in a polymer matrix, we first prepared such a film on a substrate by spin coating. Spin coating of a droplet of micron-sized silica particles dispersed in the monomer ethoxylated trimethylolpropane triacrylate (ETPTA) resulted in a uniform film of particles arranged in hexagonal layers parallel to the substrate. The thickness of the films was between 6  $\mu\text{m}$  and 20  $\mu\text{m}$  depending on the spin speed and spin time. The process and resulting structures are described in detail in Chapter 4. The



results in Chapter 4 suggested that the nearest-neighbor distance of the particles sensitively depended on experimental conditions as the particle size and ionic strength of the medium. Figure 5.1 illustrates this with some confocal microscopy images. The spacing of the silica particles in a hexagonal layer ranged from 1.1 times to as much as 1.4 times their diameter. The separation between the layers was in all cases approximately 0.8 times the in-plane inter-particle distance. The particles that were 1.1 times their diameter spaced were almost touching each other and we will refer to these structures as “structures of touching particles”. The particles that were 1.4 times their diameter spaced, were not touching each other in any direction and we will refer to those structures as “structures consisting of non-touching particles”. The two structures have, however, the same symmetry and can be regarded as close-packed structures, but consisting of spheres with a diameter 1.1 or 1.4 times the physical diameter of the particles.

The polymerized spin coated films with ordered silica particles could carefully be lifted off the substrate with a scalpel. Without damage films as thin as 6  $\mu\text{m}$ , with 5-6 layers of non-touching 0.79  $\mu\text{m}$  or 3 layers of non-touching 1.2  $\mu\text{m}$  diameter particles, were lifted off their substrate (Figure 5.2). The films were flexible and could be bent. They had a tendency to curl such that the side originally attached to the substrate, was on the outside of the resulting roll.

### 5.3.2 Selective removal of the polymer matrix

The refractive index contrast between the particles and their surrounding medium can be greatly increased by removing the polymer matrix. One method was to heat the freestanding films in an oven to 500°. Even when effort was made to place the films as flat as possible in the oven, the samples curled during heating. This was disadvantageous for further experiments. The fact that the films stayed intact was, however, very promising. For comparison, we heated crystals in a polymer matrix without lifting the film from the substrate with the same heating program. Those films fell apart into small pieces, likely due to adhesion to the substrate. This makes them useless for applications.

Freestanding films stayed intact during heating and became whitish because of the large refractive index difference between the silica particles and the air which causes scattering of the light. Spin coated films supported by a substrate (Chapter 4) and freestanding films showed Bragg reflections under white light illumination. When illuminating a film after the polymer matrix had been removed, also Bragg colors appeared. This indicates that the particles were still ordered.

The polymer melted in the electron beam, but after removal of the polymer matrix the structure could be examined with scanning electron microscopy (SEM, Philips XL30 FEG). Figure 5.3 shows some of the resulting crystals of

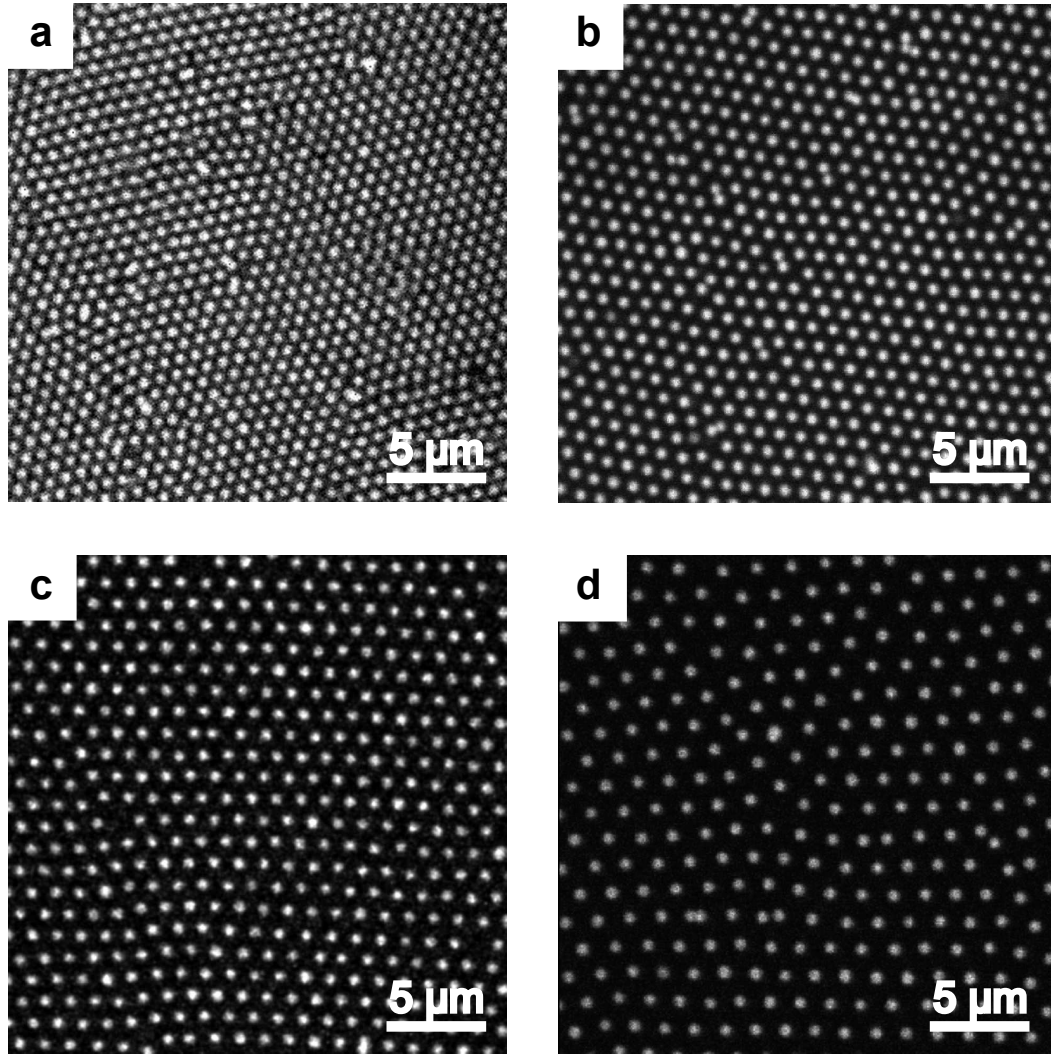


**Figure 5.1:** Confocal micrographs of polymerized spin coated films of silica particles in ETPTA supported by a glass substrate. Different in-plane interparticle distances were obtained. The  $0.79\ \mu\text{m}$  diameter particles formed both touching structures with in-plane interparticle distances of  $0.85\ \mu\text{m}$  (a) and non-touching structures with an in-plane interparticle distance of  $1.06\ \mu\text{m}$  (b). Also  $1.2\ \mu\text{m}$  diameter particles formed both touching (c) and non-touching structures (d) with an in-plane interparticle distance of  $1.27\ \mu\text{m}$  and  $1.68\ \mu\text{m}$  respectively. The  $z$ -separation of the layers was 0.8 times the in-plane interparticle distance, i.e. similar to that in FCC-like structures.

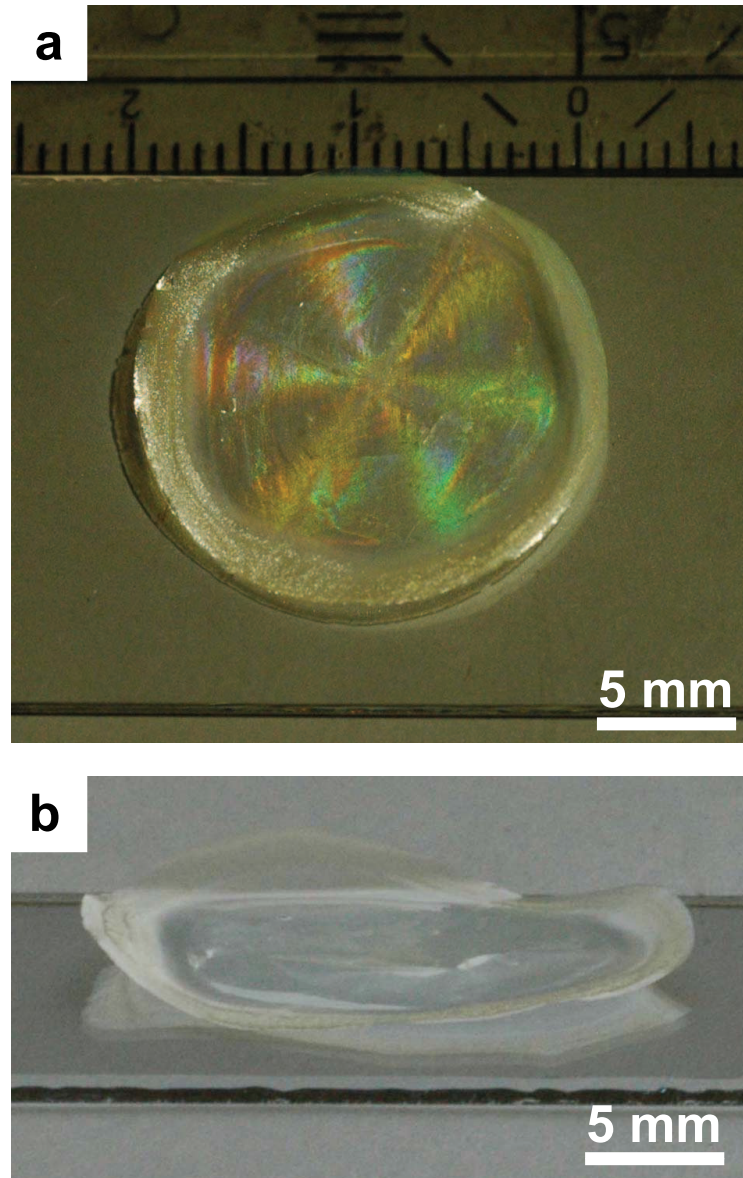


**Figure 5.2:** Photographs of a freestanding colloidal crystalline film of silica particles in a polymer matrix formed by spin coating. The diameter of the circular film was 22 mm. a) Under white light illumination a six-armed diffraction star appeared indicating hexagonal layers of particles parallel to the surface of the film. b) A side view shows that the film curled.

silica particles in air. Because the films were freestanding no stress arose that could destroy the crystals or that caused crack formation. A crystalline film as large as 0.5 mm stayed intact (Figure 5.3a). It was only broken into three pieces because these crystals of silica particles in air are very brittle. We heated both touching and non-touching freestanding crystalline films. Figure 5.3b shows that the crystallinity of a film of touching spheres was retained. Also structures of non-touching spheres were crystalline after heating and removal of the polymer matrix. The distances between the particles changed compared to the distances before removal of the polymer matrix. Obviously, the particles of neighboring layers were touching or else the structures would have collapsed. In some cases the in-plane interparticle distance also changed. Instead of staying non-touching within one layer some structures became also touching within the hexagonal layers. Figure 5.3c is an example of a structure of 1.2  $\mu\text{m}$  diameter particles that do not only touch particles of the underlying layer, but also neighboring particles in the same layer although they were non-touching before heating. Due to heating the whole sample contracted resulting in a structure of touching particles. The in-plane nearest-neighbor distances were 1.60  $\mu\text{m}$  and 1.11  $\mu\text{m}$ , before and after removal of the polymer matrix respectively. The separation between the particles after heating was even smaller than their size of 1.16  $\mu\text{m}$  measured with transmission electron microscopy before heating. Silica particles synthesized via a Stöber growth are porous and therefore, it is not uncommon that they shrink on the order of 10% in volume when they are severely heated [158, 159].

Something different happened when we heated a non-touching structure of 0.79  $\mu\text{m}$  diameter particles. Figure 5.3d shows that after removal of the polymer matrix, the particles are still not touching neighboring particles in the same layers. Apparently the film contraction was in this case not isotropically. The in-plane distance between the particles decreased from 1.06  $\mu\text{m}$  to 0.97  $\mu\text{m}$ , but still not as much as needed to make the structure completely touching. Now, the symmetry of the structure changed. First, it had an FCC-like symmetry, but now the structure consisted of hexagonal layers that were compressed in the direction normal to the hexagonal layers.

Because the symmetry changes the optical properties, it is interesting to understand why and when the symmetry of the structure changes during removal of the polymer matrix. Differences between these samples were 1) the particle diameter and 2) the number of layers. The film of 1.2  $\mu\text{m}$  diameter particles that became touching consisted of 3–4 layers. The film of 0.79  $\mu\text{m}$  diameter particles that contracted anisotropically consisted of 7–9 layers. These differences do not give an obvious explanation for the different behavior and more experiments have to be done.

The polymer matrix can in principle also be removed by etching with an oxygen plasma [21]. SEM images (Figure 5.4) show, however, that polymer is only removed from the top part of the sample. That the plasma does not



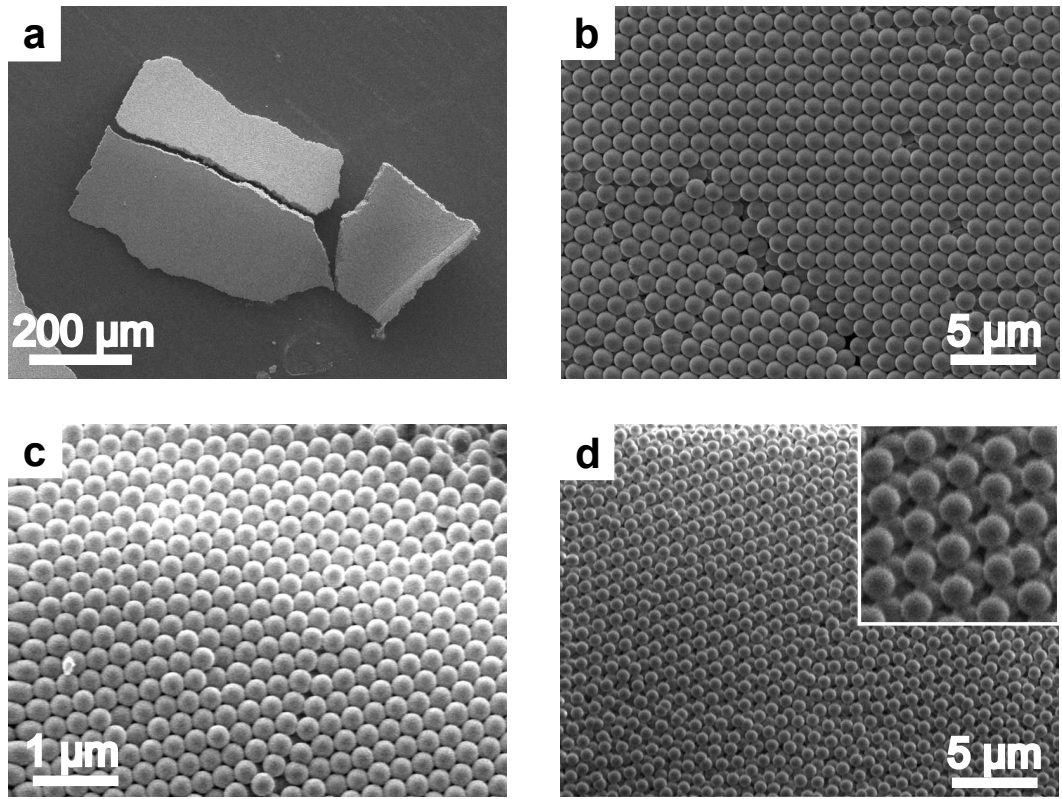


**Figure 5.3:** SEM images of crystals of silica colloids in air. The crystals were fabricated by spin coating. The polymer matrix was then removed by heating it in an oven to 500°C. a) A crystal of 1.2  $\mu\text{m}$  diameter silica particles as large as 0.5 mm stayed intact during removal of the polymer matrix. b) Close-up of the crystal of panel (a) showing that it had a close-packed structure. c) A crystal of 1.2  $\mu\text{m}$  diameter silica particles that was non-touching before heating, became touching. d) A crystal of 0.79  $\mu\text{m}$  diameter silica particles that was non-touching before heating, stayed so. The inset is a 5  $\mu\text{m}$  x 5  $\mu\text{m}$  area. To decrease charging of the sample, the crystal in panel (c) was coated with a thin layer of carbon before imaging.

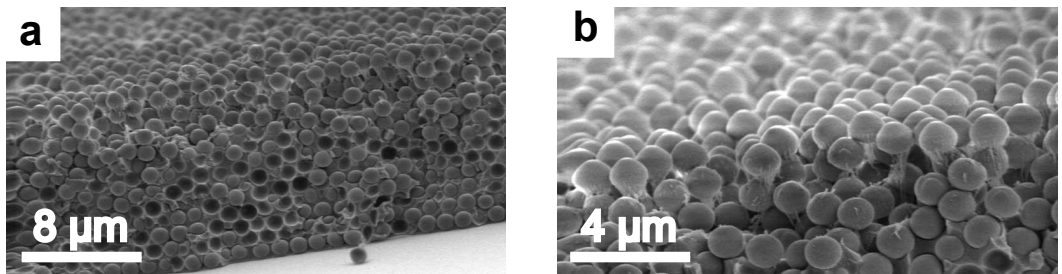


**Figure 5.4:** SEM images after treating a spin coated film of 1.2  $\mu\text{m}$  diameter particles with an oxygen plasma. The plasma only entered the top few layers. b) Close-up showing that also at the top of the structure the plasma did not reach sites underneath a silica particle.

penetrate the whole sample is probably caused by the fact that we used a reactive ion etching (RIE) plasma etcher. This means that in the RF chamber a plasma is created by a strong radio frequency electromagnetic field. A bias voltage then attracts the plasma to the sample. The plasma is thus strictly directed in one direction and it cannot reach sites below an object, e.g. a silica particle. Because only polymer at the top part of crystalline films is etched away, heating to 500°C is a better method to obtain crystals of silica particles in air.

### 5.3.3 Selective removal of the silica particles

The first method used to remove the silica particles was wet etching with an HF solution. After etching and drying in air the film was white. Instead of silica particles that nearly match the refractive index of the matrix, the polymer film now contained holes that caused scattering of light and turned the film opaque. Under white light illumination Bragg colors appeared. Before treating the film with HF, the silica particles could be detected with a confocal microscope after excitation of the FITC molecules in the particle cores with the 488 nm line of an Ar laser of the microscope. After wet etching and soaking the film in a refractive index matching mixture of glycerol and water (84:16 wt%) no fluorescent signal was measured. Clearly the particles were all etched away.

To image the resulting structure the fluorescent dye rhodamine B isothiocyanate (RITC) was dissolved in the glycerol/water mixture surrounding the etched film. In a confocal microscopy image taken in fluorescent mode only several holes appeared. In the original structure of silica particles in the polymer matrix, not all particles touched each other failing to form a continuous network. The fluorescently labeled dye could therefore only fill a few interconnected holes at the surface (Figure 5.5a). Conversely, in an image taken in transmission objects that are not refractive index matched show up, i.e. empty holes. Figure 5.5b is such a transmission measurement and it shows an ordered array of holes. Many more holes show up than in the image taken in fluorescent mode. Apparently holes formed, but they were not filled with the glycerol/water refractive index matching solvent mixture. Although the particles did not form a continuous network, they were all etched. This indicates that the aqueous HF solution could penetrate the polymer matrix even though the mixture of glycerol and water with RITC could not.

A second method to selectively remove the silica particles was by plasma etching. As is shown in Figure 5.6 all silica particles at the surface were removed. A regular pattern of holes remained after the silica etch. Again, material underneath an object, like the one in Figure 5.6b, had not been etched. Wet etching with HF resulted in a better removal of the silica particles. It is, however, not known whether the silica residues were completely removed from the polymer film or that traces of it stayed behind in the holes.

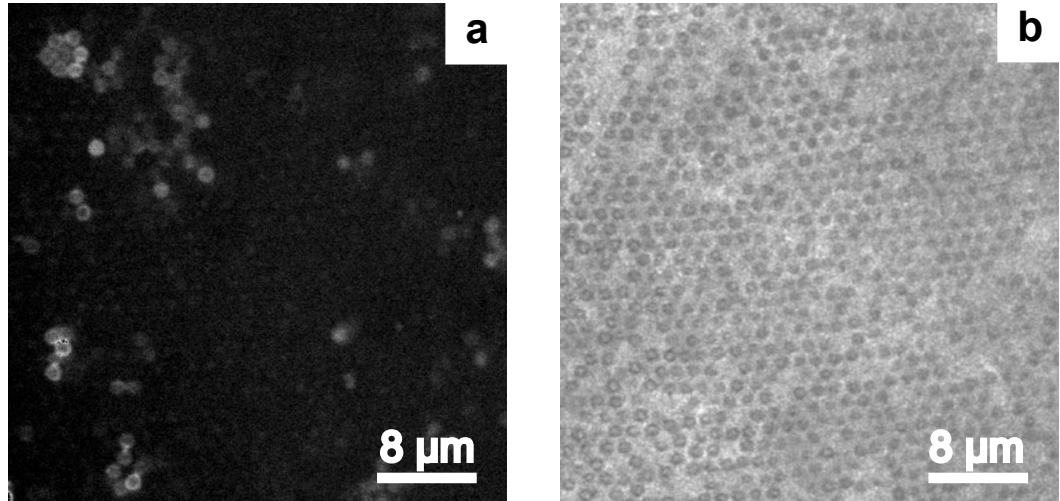


**Figure 5.5:** Confocal microscopy images after wet etching a colloidal crystalline film originally consisting of  $1.2\ \mu\text{m}$  diameter silica particles with HF. a) An image in fluorescent mode shows where a fluorescently labeled fluid penetrated the holes. b) In transmission the unfilled holes are visible. The two images are complementary.

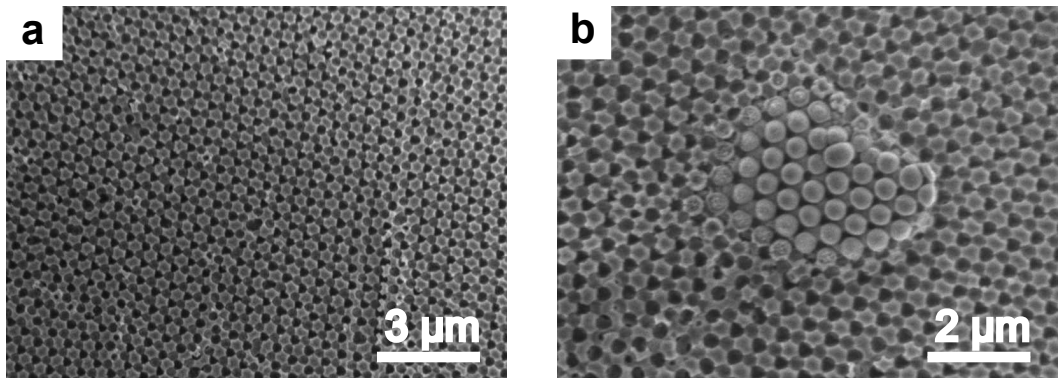


**Figure 5.6:** SEM images of a spin coated film after removing the silica particles at the surface by plasma etching. b) A piece of the film that fell upside down on top of the etched side of the sample shows the size of the originally present silica colloids. The particles were  $0.4\ \mu\text{m}$  in diameter. To reduce charging of the sample, the crystal was coated with a thin layer of carbon before imaging.

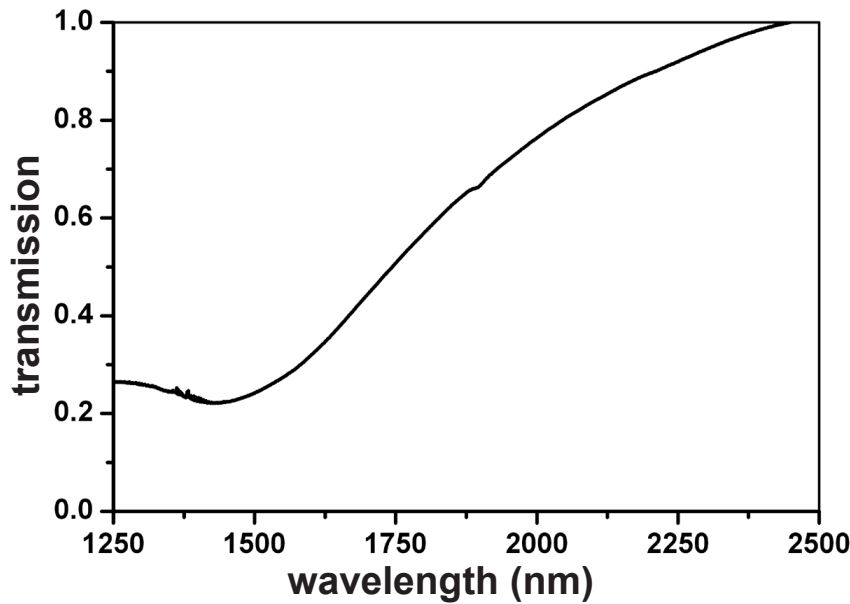


**Figure 5.7:** Transmission spectrum of a freestanding colloidal crystalline film consisting of approximately 8 crystalline layers of  $0.79\ \mu\text{m}$  diameter particles that were non-touching within the hexagonal layers. The spectrum was taken under normal incidence.

#### 5.3.4 Spectroscopy

Silica colloids have a refractive index of about 1.45 [84]. The refractive index of the polymer ETPTA was measured to be 1.49 (see Chapter 4). This refractive index contrast is too small to observe peaks in a transmission spectrum of films with a thickness of  $6\ \mu\text{m}$  and approximately 8 crystalline layers, to give information about the crystal structure. Removing the polymer matrix greatly enhances the contrast.

Confocal microscopy measurements showed that before removal of the polymer matrix the film consisted of particles arranged in hexagonal layers (Figure 5.1). SEM images (Figure 5.3c) showed that at least at the surface of the sample the order was retained. Assuming that the internal structure is also conserved during burning of the polymer a Bragg peak should be observed in a transmission spectrum. From the position of a Bragg peak the distance between the layers can then be calculated.

A transmission spectrum obtained from a freestanding film of silica particles in air is depicted in Figure 5.7. The measurement was done at normal incidence, i.e. perpendicular to the hexagonal layers. The spectrum contains a minimum around 1440 nm. The minimum is shallow, but is expected to become sharper upon decreasing the refractive index contrast, which reduces scattering.

The position of a Bragg peak can be calculated with Bragg's law, which



reads:

$$m \lambda = 2 n d \sin \theta. \quad (5.1)$$

$m$  indicates the diffraction order,  $\lambda$  is the wavelength,  $n$  is the effective refractive index of the crystal,  $d$  is the distance between the layers and  $\theta$  is the angle of incidence. The distance between the layers can be obtained from geometrical considerations. The particles of this sample were 790 nm in diameter as determined with transmission electron microscopy (TEM). From SEM images, e.g. Figure 5.3c, we determined that the in-plane distance between the particles was 975 nm. Since neighboring layers had to touch, the layer separation had to be 554 nm. Compared to a face centered cubic crystal the structure was compressed in the direction perpendicular to the layers. The particle volume fraction can be calculated from this geometrical model and was  $\phi = 0.57$ . For the effective refractive index we calculated the volume averaged refractive index. The refractive index of silica grown via a Stöber growth is  $\approx 1.45$  [84] and the effective refractive index was calculated to be  $n = 1.26$ . The spectrum was measured at normal incidence. The first order Bragg peak is then expected around  $\lambda = 1392$  nm. This is close enough to the position of the dip found in the transmission spectrum to say that the assumptions made in the calculation were correct. We take this as a confirmation that the separation between the layers was 554 nm.

### 5.3.5 Ion beam deformation

Freestanding colloidal crystalline films were irradiated with 30 MeV  $\text{Si}^{5+}$  ions. The photograph in Figure 5.8 shows a sample after ion beam irradiation. Crystalline films as large as 5 mm stayed intact, despite of the high stresses that form during irradiation. SEM images showed that no cracks formed (Figure 5.9). This is in great contrast with the result of ion beam irradiation of crystalline films supported by a substrate, in which case cracks formed every 2  $\mu\text{m}$  [168].

Figure 5.10 contains SEM images of a freestanding film of close-packed 1.2  $\mu\text{m}$  diameter silica particles before and after irradiation. All particles deformed in the same direction. Their aspect ratio was 1.33 after irradiation. Also 0.76  $\mu\text{m}$  diameter silica particles of a freestanding colloidal crystalline film deformed (Figure 5.11). Their aspect ratio after deformation was 1.04. Because of curling of the films the orientation and thus the direction of the beam and the direction of deformation was different for the different samples. Just as is known for single particles [172], the smaller particles in the films were less deformed than the larger particles.

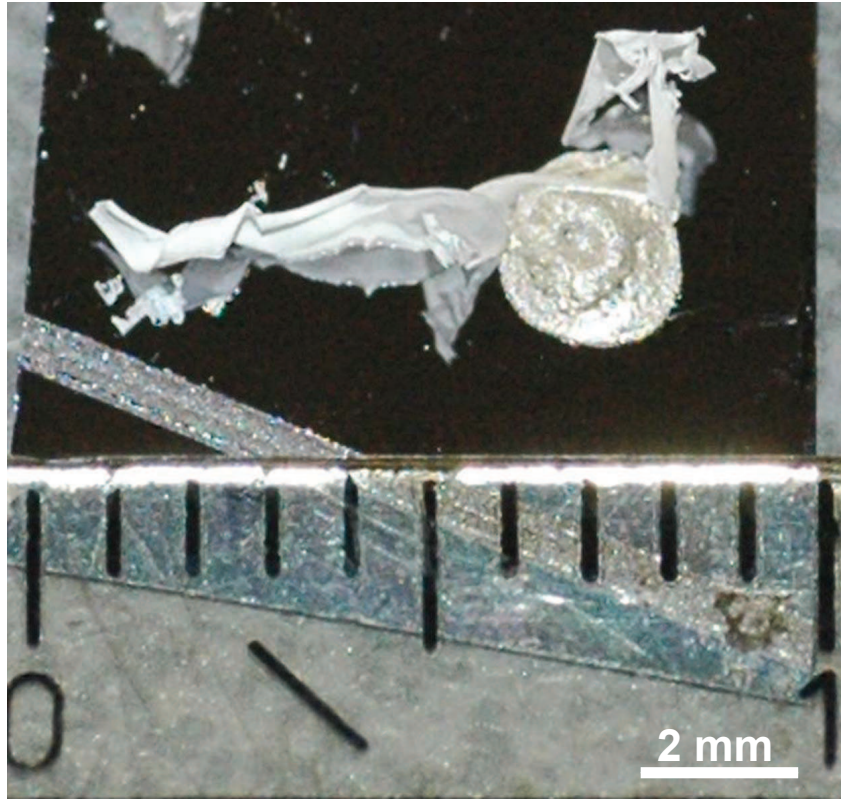


**Figure 5.8:** Photograph of a freestanding colloidal crystalline film after ion beam irradiation. Although the film was as long as 5 mm, it stayed intact. The bottom right corner of the film was attached to the substrate with a conductive adhesive.

## 5.4 Conclusion

We prepared colloidal crystalline freestanding films of silica particles in a polymer matrix, crystals of silica particles in air, and ordered air spheres in a freestanding polymer matrix. Also optical measurements and ion beam deformation experiments were performed. By spin coating colloidal crystalline films consisting of silica particles of  $0.79\ \mu\text{m}$  or  $1.2\ \mu\text{m}$  in diameter in a polymer matrix were formed. In these films the particles were arranged in randomly stacked hexagonal layers. Both structures in which the particles were touching and non-touching were formed.

The polymer matrix could be removed by heating the samples to  $500^\circ\text{C}$  or by etching it with an oxygen plasma. Plasma etching was less effective, because it only removed the polymer from the top part of the film. In neither case cracks formed and the samples were still crystalline after these treatments. When the polymer matrix was removed by heating, structures consisting of non-touching  $1.2\ \mu\text{m}$  diameter particles became touching. The whole structure contracted isotropically. Non-touching structures of  $0.79\ \mu\text{m}$  diameter particles contracted anisotropically. The particles came into contact with particles from

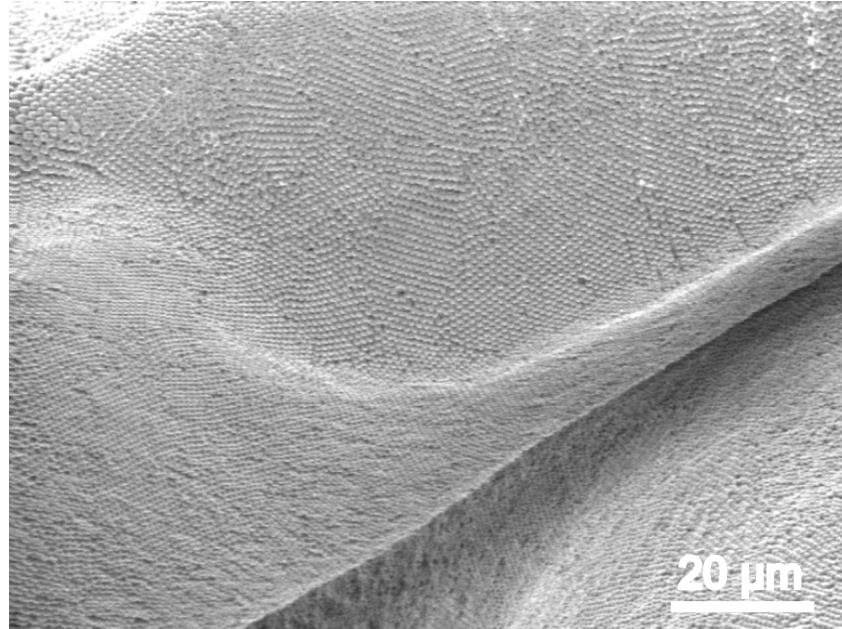


**Figure 5.9:** SEM image of a freestanding colloidal crystalline film of originally  $1.2\ \mu\text{m}$  diameter silica particles after irradiation with  $30\ \text{MeV}\ \text{Si}^{5+}$  ions. No cracks formed.

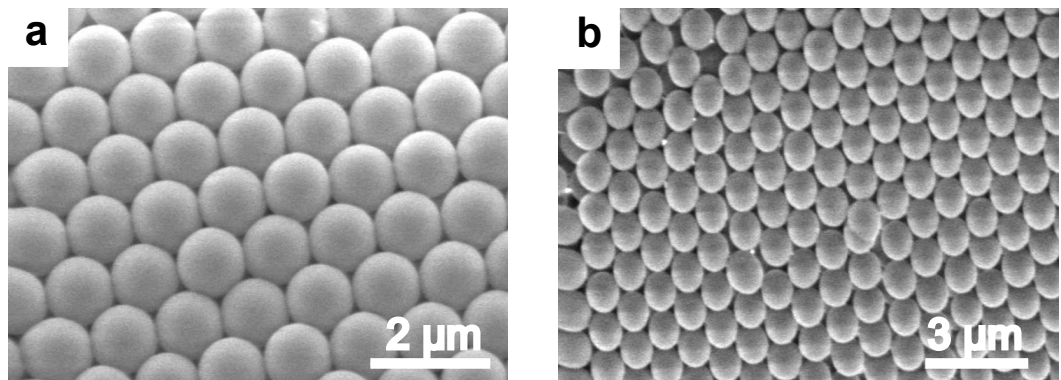


**Figure 5.10:** SEM images of a freestanding colloidal crystalline film of touching  $1.2\ \mu\text{m}$  diameter silica particles a) before and b) after ion beam irradiation. The images were taken at an angle of  $45^\circ$ .

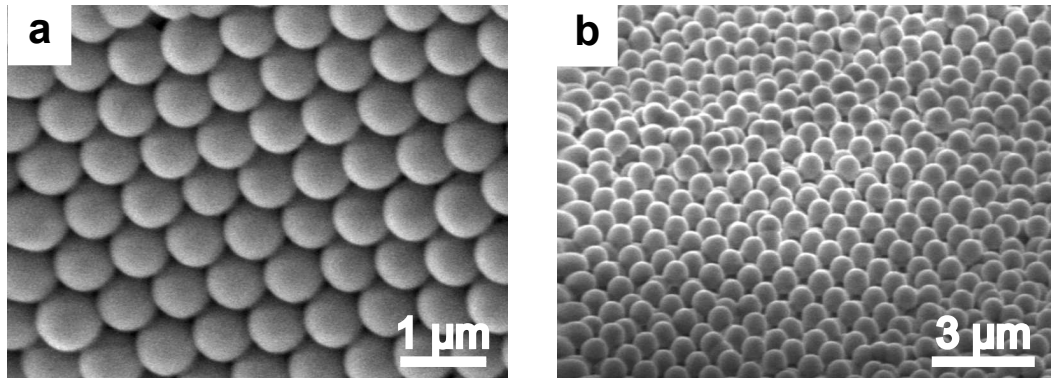


**Figure 5.11:** SEM images of a freestanding colloidal crystalline film of  $0.79\ \mu\text{m}$  diameter silica particles a) before and b) after ion beam irradiation. The particles did not touch neighboring particles of the same layer. The images were taken at an angle of  $45^\circ$ .

neighboring layers, but they did not touch particles in the same layer. The symmetry of the structure had changed. More research is needed to reveal the origin of the different behavior of the two types of films.

Inverted crystals of air-spheres in a polymer matrix could be obtained by etching the silica particles with an 8 wt% HF solution or by plasma etching. Again, plasma etching was less successful, because the plasma only penetrated the top part of the crystalline films.

A non-touching structure of silica particles in air showed a dip in a transmission spectrum around 1440 nm. We compared this with the position of a Bragg peak that would appear due to diffraction from the hexagonal layers. Assuming that neighboring layers were touching, we calculated from the in-plane interparticle distance that a Bragg peak would appear at 1392 nm. The dip in the spectrum lay close to this wavelength and we concluded that the minimum in transmission was indeed caused by diffraction from the hexagonal layers that were calculated to be 554 nm spaced from each other.

By irradiating freestanding crystalline films of silica particles with 30 MeV  $\text{Si}^{5+}$  ions the particles could be deformed as observed before. Contrary to what was observed before for colloidal crystalline films on a substrate, no cracks formed during irradiation. Films as large as a few millimeters stayed intact.

## Acknowledgements

Plasma etching was done together with Job Thijssen at AMOLF, Amsterdam. We thank Chris Rétif for his assistance at these experiments. The MeV ion irradiation experiments were done with the Van de Graaff ion accelerator of the Surface, Interfaces and Devices group (SID, Utrecht University). We would

like to thank them for allowing us to use their setup. Carlos van Kats is acknowledged for performing these irradiations. Joan Penninkhof is thanked for her assistance with these experiments. Furthermore, we would like to thank Job Thijssen and Dannis 't Hart for their assistance with the FTIR measurements. Finally, Job Thijssen and Carlos van Kats are acknowledged for SEM measurements. Dannis 't Hart is acknowledged for synthesizing the 0.79  $\mu\text{m}$  diameter silica particles.

## Epitaxial colloidal crystal growth of strings of colloidal dipoles

### Abstract

We show how to control structure formation in colloidal suspensions in all three dimensions using a local non-uniform electric field. The electric field had local modulations because one of the electrodes of the parallel plate capacitor carried a 2D pattern of bulges. Such templates were made by placing micron-sized silica particles in ethanol one by one in a regular pattern on a glass substrate by means of optical tweezers. To prevent surface tension forces from destroying the structure during drying, the templates were preserved by critical point drying or they were protected by growing a thin layer of silica after which we could let the ethanol simply evaporate. The templates were then coated with a conductive layer of gold. With one of these patterned electrodes on one side, an alternating current electric field was applied over various colloidal suspensions. At low particle volume fractions and a root-mean square field strength of 0.35-0.71 kV/mm the particles arranged in strings along the field lines. In systems of particles with a higher dielectric constant than the suspending medium these strings formed right on top of the bulges of the patterned electrode. The dielectrophoretic force present in non-uniform electric fields attracts the particles to regions with a higher field strength. When the dielectric constant of the particles was lower than that of the suspending medium the dielectrophoretic force was reversed, thus repelling the particles from the regions with a higher field strength, and strings formed not on top of the particles of the template but rather in between.



## 6.1 Introduction

External fields affect the structure of colloidal suspensions [55, 173]. Under gravity colloids with a hard-sphere like potential form hexagonal layers that are mostly randomly stacked. They have, however, a tendency to form the lowest free energy structure, i.e. face centered cubic (FCC) crystals instead of hexagonal close packed (HCP) structures [7] because of the slightly higher thermodynamic stability of FCC [140]. Shear can induce crystallization of concentrated hard-sphere like [10] or charged [11] suspensions and hexagonal layers form in the velocity-vorticity plane [10]. In an electric field colloidal particles with a dielectric constant different from the surrounding medium acquire an induced dipole moment. They can then form strings, (metastable) sheets or body centered cubic (BCC) structures. Which of these structures forms, depends on the electric field strength, time as some of the observed structures are metastable, and the particle concentration [43, 44, 174, 175]. Via these parameters there is control over the type of structures formed, but not over their orientation and placement. By using a structured wall with the symmetry and orientation of a desired crystal plane crystallization, in 3D can be manipulated in ways that are similar to epitaxial crystal growth. This includes the growth of crystals that are out of equilibrium [176, 177]. The use of a structured wall in the presence of external electric or magnetic interactions could induce the lateral positioning of strings of dipoles that form under the influence of the induced dipolar interactions.

Manipulating the lateral position of colloidal particles in order to arrange particles in the solution above a pattern has been done for magnetic particles. Using polymer-on-polymer stamping Lyles *et al.* [178] made templates with micrometer precision. The magnetic particles were nicely localized on the pattern. The number of particles at each site of the template was, however, not fixed. In some cases several particles clustered together on one site of the template. In the case of electric fields, electrohydrodynamic flows around particles close to an electrode surface have been used to induce crystallization by attractions between the particles [179, 180]. Later this approach was extended by using light induced patterns of higher and lower conductivity on semiconductor electrodes, which allowed for more control over where crystallization takes place [181]. However, this method is limited to only several crystal layers in the direction perpendicular to the electrode. Velev and co-workers were able to extend their electric field induced structuring to extended structures in 3D [182]. Their method consisted of using metallic nanoparticles to achieve self-assembly of these particles using electric fields into wire-like structures. The local field on such a thin metallic wire attracted other particles by dielectrophoretic forces. However, there was no lateral control over particle positions and in addition particles were touching in the external electric field direction.

In this chapter, we describe experiments in which we control, in all three

dimensions, the structure that particles form. By using a parallel plate capacitor of which one electrode contained a regular surface pattern we create a non-uniform electric field close to the electrode surface. Varying the electric field strength further away from the electrode surface, together with the ionic strength, controls the spacing of the strings of dipoles that form along the field lines, while the pattern on the electrodes influences the position perpendicular to the field lines. The frequency of the electric field is chosen to be so high ( $> \text{MHz}$ ) that the ions in the double layer cannot follow the field thus limiting the dipolar interactions to the polarizability of the particles in the solvent. We will describe in detail how we made these templates on the electrodes with optical tweezers and how we conserved the structures. Next, we will show our first results on structure formation of various colloidal systems in alternating current electric fields.

## 6.2 Colloids in electric fields

In an electric field,  $\vec{E}_{loc}$ , colloids acquire an induced dipole moment

$$\vec{p} = \frac{\pi}{6} \epsilon_{eff} \epsilon_0 \sigma^3 \vec{E}_{loc}. \quad (6.1)$$

$\sigma$  is the particle radius and  $\vec{E}_{loc}$  is the local electric field strength.  $\epsilon_0$  is the frequency dependent dielectric constant of vacuum.  $\epsilon_{eff}$  is the effective dielectric constant of the particles in the suspending medium, which depends on the overall particle concentration, because the induced dipole moments of surrounding particles alter the local field strength around a particle. At low particle concentrations and low field strengths, the effective dielectric constant can be expressed by the Clausius-Mossotti equation  $\epsilon_{eff} = 3\beta\epsilon_m$  [183].  $\epsilon_m$  is the frequency dependent dielectric constant of the suspending medium and at the high frequencies used in our experiments,  $\beta$  is given by  $\beta = \frac{\epsilon_p - \epsilon_m}{\epsilon_p + 2\epsilon_m}$ . Depending on its sign the induced dipoles are directed oppositely to the electric field ( $\epsilon_p < \epsilon_m$ ) or in the same direction as the field ( $\epsilon_p > \epsilon_m$ ) (see Figure 6.1). The interaction energy between two dipoles  $i$  and  $j$  is given by

$$\frac{u_{dip}(r_{ij})}{k_B T} = \frac{\gamma}{2} \left( \frac{\sigma}{r_{ij}} \right)^3 (1 - 3\cos^2\theta_{ij}), \quad (6.2)$$

where  $\gamma = \frac{p^2}{2\pi\epsilon_m\epsilon_0\sigma^3k_B T}$ .  $\theta_{ij}$  is the angle between the electric field and the vector connecting particles  $i$  and  $j$  (see Figure 6.1). The interaction is attractive when  $\theta_{ij} < 54.7^\circ$  and repulsive otherwise. The attraction is at its maximum when  $\theta_{ij} = 0$ , meaning that the particles prefer to align along the field lines and form strings.

Due to induced dipole interactions the particles form strings along the field lines. There is no preference over the lateral position of the strings. This



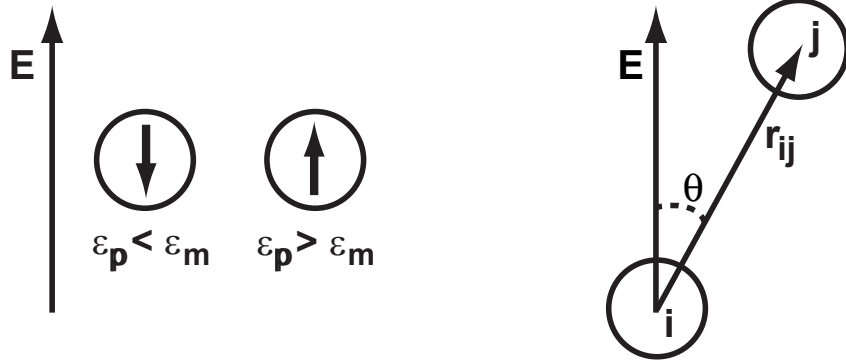


**Figure 6.1:** Depending on the dielectric contrast between particle,  $\epsilon_p$ , and suspending medium,  $\epsilon_m$ , the induced dipole moment is oriented along or opposite to the external electric field ( $E$ ). Two dipoles attract each other when the angle  $\theta_{ij} < 54.7^\circ$ . At larger angles,  $\theta_{ij}$ , they repel each other.

is different in an inhomogeneous field. When there is a field gradient, the particles are exposed to an additional, dielectrophoretic force.

$$\vec{F} = -\frac{2}{3}\pi\sigma^3\epsilon_{eff}\epsilon_0 \nabla E^2(r) \quad (6.3)$$

Particles with a dielectric constant lower than that of the medium,  $\epsilon_p < \epsilon_m$  will go towards regions with the lowest electric field and particles with a higher dielectric constant,  $\epsilon_p > \epsilon_m$  are attracted to the highest field region [184].

### 6.3 Experimental details

A schematic outline of the experiment is given in Figure 6.2. First, a patterned electrode was made of micron-sized silica particles by positioning them one by one with optical tweezers in a regular pattern on a glass substrate with or without an indiumtin oxide (ITO) layer using oppositely charged surfaces and particles. The positioning of particles with optical tweezers was done in a cell filled with ethanol. Secondly, the pattern was preserved by critical point drying (CPD) or it had to be protected from surface tension forces by growing a layer of silica ( $\text{SiO}_2$ ) over it. Templates made on glass without ITO were then coated with a conductive layer of gold. With this template the electric field cell, a parallel plate capacitor, was then assembled. Finally, the cell was filled with a colloidal suspension and an electric field was applied.

#### 6.3.1 Fabrication of patterned electrodes

Two types of substrates were used to stick the silica particles on: no. 0 glass slides (Menzel) coated with indiumtin oxide (ITO, Thin Film Devices, USA) or uncoated 18 mm diameter circular no. 1 microscopy glass slides (Menzel).

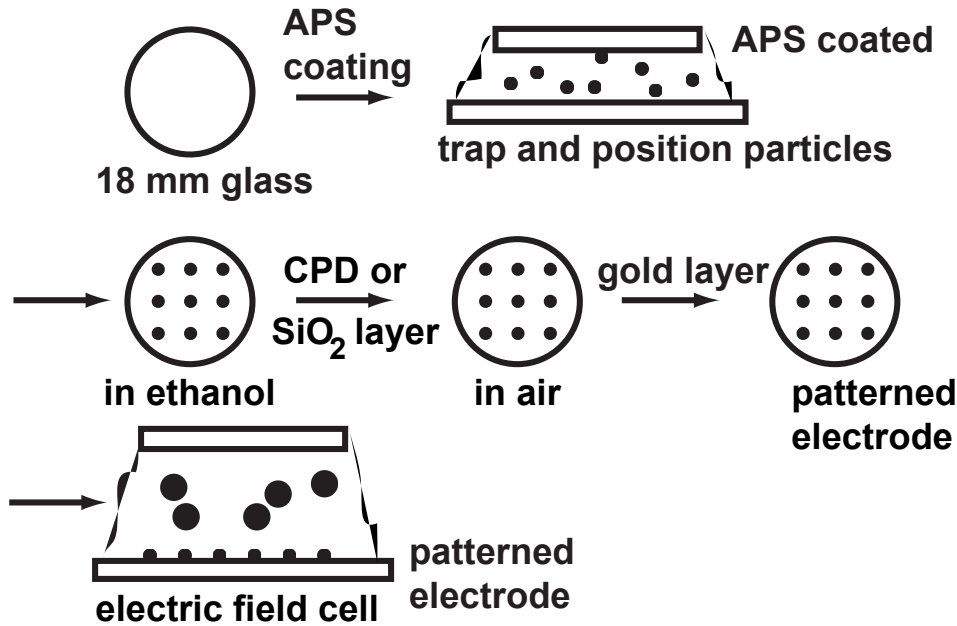


**Figure 6.2:** Outline of the experiment. Silica particles are one by one positioned in a regular pattern on a 18 mm diameter glass substrate by means of optical tweezers. This pattern was then preserved by critical point drying or by growing a thin layer of silica over it. Next, a conducting layer of gold was deposited. This electrode was then used to control the lateral position where electric field induced strings of particles formed.

In both cases the substrates were first made positively charged, as described before [84, 185], by coating them in a mixture of 180 ml technical ethanol, 4.5 ml ammonia (25%) and 23.5 ml 3-aminopropyltriethoxysilane (APS) for at least 1 hour. They were rinsed with ethanol and dried by blowing a nitrogen flow over it. All chemicals were used as received.

A scratch was made on one side of the substrate to be able to relocate the template later on in the electric field cell. The cell to trap and position the particles with optical tweezers was made with at the bottom a 22 mm diameter no. 1 microscopy glass slide (Menzel). On this slide a 10- $\mu$ l droplet of a dilute dispersion of 1.2  $\mu$ m diameter silica particles in ethanol was put. Over the droplet a previously APS coated glass substrate was then lowered with the scratch on the bottom side. Care had to be taken not to leave any air inside the cell. Surface tension forces at the gas-liquid interface of an air bubble that passes by would destroy the structure. Hot melted candle wax was then put around the sides. The wax sealed the cell after cooling down and prevented evaporation of the ethanol for at least 1 hour.

The optical tweezers setup was as described in Reference [186]. We used a Nd:YVO<sub>4</sub> (Spectra Physics, Millennia IR, 10W, cw) with a wavelength of 1064 nm and a TEM<sub>00</sub> mode profile. The beam was expanded six times with a beam

expander (Melles Griot), then it was attenuated using a half-lambda zero-order wave plate (Newport). Via a polarizing beam splitter cube only the vertically polarized light was selected. This light was coupled into two acousto-optic deflectors (AODs, IntraAction Corp., DTD-274HA6, 4 mm  $\times$  4 mm aperture). One diffracted the beam in vertical and the other in horizontal direction. A diaphragm selected the (1,1) order for trapping. Finally, a telescope with lenses broadened the beam two times to a total of twelve times before the beam was guided to a 100 $\times$  1.4 numerical aperture objective (Leica). This objective guided the laser beam into the sample through the bottom side of the sample.

To make the pattern, a particle was selected at the bottom of the cell and it was trapped in the focus of the beam. Then, the sample was moved downwards until the particle reached the top slide. Because silica particles were negatively charged, they stayed attached to the top slide that was made positively charged. This was repeated for each particle until the pattern was complete.

### 6.3.2 Conservation of the template

In many cases, the ethanol used in the cell to trap and stick the particles has to be removed. Simply allowing the ethanol to evaporate creates surface tension forces at the gas-liquid interface that often, for micron-sized particles, destroy the pattern. Removing the ethanol had to be done in a different and safe way. Two methods were used: 1) critical point drying, eliminating surface tension effects; 2) growing a thin layer of silica over the pattern that attaches the particles to the substrate. The ethanol could then be safely allowed to evaporate.

For critical point drying we used a Baltec 030 critical point dryer (CPD). The principle of critical point drying is to bring the medium into its supercritical state by heating it at constant volume above its critical point. The supercritical fluid is let out of the sample chamber at constant temperature. Below the critical pressure the fluid becomes a gas. This phase transition occurs without a discontinuity in the density and therefore without an interface between the two phases with concomitant destructive surface tension forces. The fluid that we used was carbon dioxide because of its accessible critical point and because it is not toxic. Ethanol, which was present in the trapping cell, has a low solubility in liquid CO<sub>2</sub>. Acetone has a high solubility and therefore the ethanol was first exchanged for acetone.

The CPD sample chamber was filled with acetone (p.a.). The candle wax was removed with a scalpel and both slides of the sample with dispersion in between were transferred to the CPD sample chamber. Then, the 22 mm unpatterned bottom slide was removed. Removing the unpatterned slide only after transfer to the CPD minimized the chance of evaporation. The CPD sample chamber was then cooled to 10°C and was completely filled by adding liquid carbon dioxide. When the sample chamber was completely filled the pressure

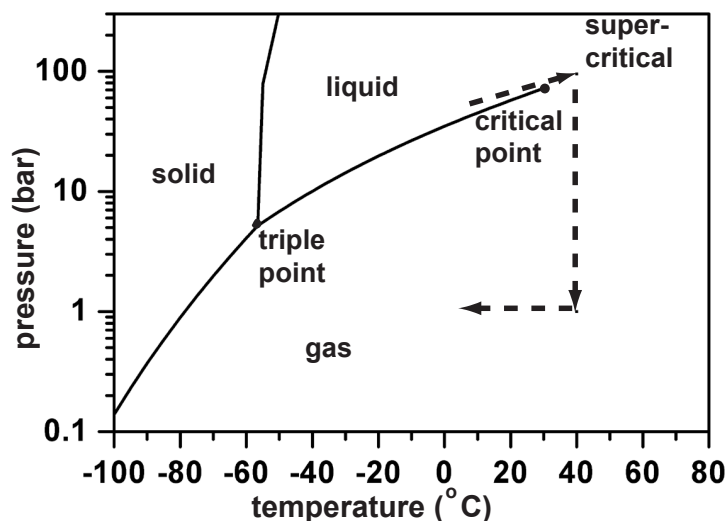


**Figure 6.3:** Phase diagram of carbon dioxide [187, 188]. Arrows indicate the different stages in the critical point drying process.

inside was about 50 bar. The medium was exchanged every 5-8 minutes with liquid  $\text{CO}_2$  until all acetone and traces of other liquids were removed. The CPD sample chamber was then heated to  $40^\circ\text{C}$ , thereby increasing the pressure to 90 bar.  $\text{CO}_2$  has a critical point of  $31^\circ\text{C}$  at 74 bar. At  $40^\circ\text{C}$  and 90 bar,  $\text{CO}_2$  was thus supercritical. This supercritical fluid could then be slowly, i.e. in at least 1 hour, let out of the CPD sample chamber. Figure 6.3 shows the phase diagram of  $\text{CO}_2$  in which arrows indicate the route followed in the critical point drying process.

An alternative and less labor-intensive method to preserve the pattern is to anchor the particles to the substrate with a thin layer of silica. To do so, instead of transferring the patterned glass slides into the CPD, they were put in a mixture of technical ethanol, ammonia (25%) and tetraethoxysilane (TES). To control the thickness of the silica layer we used the method described by Vossen *et al.* [185]. We added a known number of small silica seeds of which we measured the size by static light scattering (SLS). A silica layer will grow both on the template and on the small silica seeds. If no silica seeds would be added, the amount of TES needed to grow a silica layer of a few nanometers would be so small that it cannot be accurately measured. By adding silica seeds the surface immensely increases, making it possible to accurately add the amount of TES needed to grow a layer of a certain thickness with nanometer control. The layers that we grew, were 15 nm in thickness. The final thickness could be determined by measuring the radius of the seed particles afterwards with SLS again. Assuming that the growth rate on top of the template was the same as that on the seeds, the size difference of the seeds before and after layer growth, was the layer thickness. After growing this layer of silica the sample could simply be rinsed with ethanol and dried in air.

### 6.3.3 Electric field cell

Templates made on ITO coated glass were now ready for making the electric field cell, but the other templates need an additional preparation step. We first had to coat them with a conductive layer of gold. This was done with a Cressington 208hr sputter coater equipped with a layer thickness meter. Because gold does not wet glass very well, the template was first coated with a 3-nm layer of chromium. The chromium target was sandblasted to remove most of the oxide layer and placed in the sputter coater. The plasma was first pink. When the color had changed into deep blue we opened the shutter to deposit the chromium. Then, the chromium target was exchanged for a gold target and a 10-nm layer of gold was deposited. This layer thickness was chosen because it is thick enough to conduct, but still thin enough to be able to image particles through the gold with a microscope.

Next, the electric field cell was assembled. The configuration of cells for dispersions with polymethylmethacrylate (PMMA) particles was slightly different from cells for dispersions with silica colloids. In both cases the top electrode was a no. 0 (thickness 80-120  $\mu\text{m}$ ) ITO coated glass slide. For dispersions with PMMA the coating was on the outside of the cell, because the particles interacted with the coating. Electric fields needed to induce structures in the silica dispersions were higher than those needed for PMMA dispersions. With our generator such high fields could only be reached when the conductive layer was on the inside of the cell, decreasing the electrode spacing. The bottom slide was one of the patterned electrodes. Our PMMA particles tended to stick to the walls. Therefore, before using the cell we flushed it with a solution of the stabilizer of the PMMA synthesis in dodecane. This stabilizer consists of poly(hydroxystearic acid) (PHSA) attached to a backbone formed by glycidyl methacrylate and methyl methacrylate units. Silica particles do not stick to glass and no additional coating step was needed in that case.

In both cases we used  $\sim 20 \mu\text{m}$  diameter porous silica spheres as spacers between the electrodes. The typical gap width was 30  $\mu\text{m}$ , which was also the electrode spacing for cells for dispersions with silica. The electrode spacing for cells for PMMA systems was  $\sim 150 \mu\text{m}$ . After filling the cell with the dispersion the cell was first sealed with hot candle wax and then with no. 68 UV-curing optical adhesive (Norland). The candle wax prevented contact between the dispersion and the glue. The glue was used for a tighter sealing of the cell. We applied 1 MHz alternating current electric fields. Using high frequency AC fields prevented polarization of the double layer surrounding the particles.

### 6.3.4 Colloidal systems

We used two types of systems and categorize them by the dielectric contrast between the particles and the suspending medium. Of the first type were systems consisting of particles with a dielectric constant higher than that of the medium

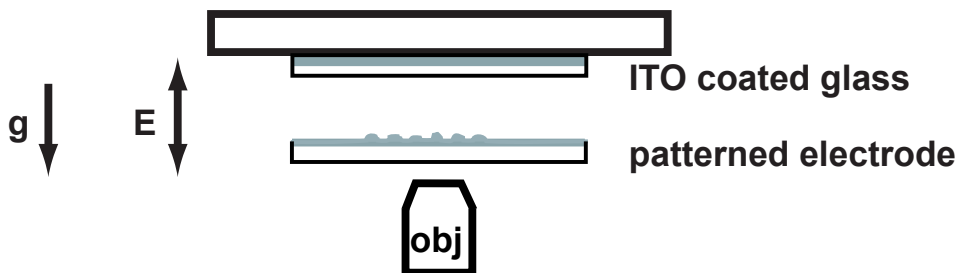


**Figure 6.4:** Schematic representation of the electric field cell (not drawn to scale). The conducting layers are depicted in grey. In all cells the conducting layer of the top slide was indiumtin oxide (ITO). This layer was on the outside of the cell for PMMA systems and on the inside for  $\text{SiO}_2$  systems. The bottom slide was either coated with gold or with ITO. This layer was always on the inside of the cell and contained the template.

$\epsilon_p > \epsilon_m$ . We used  $3.34 \mu\text{m}$  diameter Nile-Red labeled polymethylmethacrylate (PMMA) particles ( $\epsilon \approx 2.6$  [189]) dispersed in *cis*-decahydronaphthalene (*cis*-decalin,  $\epsilon = 2.176$  at  $25^\circ\text{C}$  [190]) at a volume fraction of  $\phi = 0.10$ . We also used  $1.2 \mu\text{m}$  diameter silica particles ( $\epsilon = 4.3$  [191]) in ethoxylated trimethylolpropane triacrylate (ETPTA, Aldrich,  $\epsilon = 3$  [23]). A  $0.4 \mu\text{m}$  diameter core of these particles was fluorescently labeled with fluorescein isothiocyanate (FITC). Of the second type were systems containing particles with a dielectric constant lower than that of the medium,  $\epsilon_p < \epsilon_m$ . As a system with particles of a dielectric constant lower than that of the solvent, we used  $1.4 \mu\text{m}$  diameter PMMA particles labeled with 7-nitrobenzo-2-oxa-1,3-diazol (NBD) dispersed in cyclohexylbromide (CHB,  $\epsilon = 7.92$  at  $25^\circ\text{C}$  [192]) at a volume fraction of  $\phi = 0.04$ .

The PMMA particles were synthesized using the method described by Bosma *et al.* [193]. For the silica particles we used a Stöber growth [83]. To label the core of the silica particles with a fluorescent dye we used the method of Van Blaaderen and Vrij [84].

## 6.4 Results and discussion

### 6.4.1 Fabrication of patterned electrodes

Positioning silica particles with optical tweezers on ITO coated glass was not without difficulties. The ITO coating absorbed light from the  $1064 \text{ nm}$  trapping laser that was used with a laser output of  $0.2\text{--}0.5 \text{ W}$ . This heated the ethanol to its boiling point. Gas bubbles formed and these bubbles severely changed the position of particles that had been stuck to the glass. To stick particles with this setup on ITO coated glass, the laser power had to be decreased. The laser power was set to its minimum of  $0.2 \text{ W}$  and the polarization of the

light was rotated such that a larger fraction was guided into the beam dump. A disadvantage of decreasing the laser power is that the trapping stiffness decreases, thereby decreasing the accuracy of positioning the particles. Sticking particles on bare glass did not present such problems. Bare glass was thus the preferred substrate. We made regular square symmetric and hexagonal patterns with interparticle distances between  $2\ \mu\text{m}$  and  $12\ \mu\text{m}$ .

Critical point drying was the main method used to remove the ethanol from the cell in which the template was made. It appeared to be a very delicate process. Sometimes the pattern was distorted and in some cases the pattern had completely vanished. As it is not possible to examine the sample during the critical point drying process, no definite answer can be given what went wrong.

Possible reasons for failures are 1) that the number of cycles used to exchange the initial medium for  $\text{CO}_2$  is insufficient; fluid that does not become supercritical at  $40^\circ\text{C}$  at 90 bar then stays behind, 2) that the fluid level drops too far during an exchange cycle by which a destructive gas-liquid interface passes the structure, 3) that the flow during exchange of the medium is so strong that the particles detach from the substrate. Critical point drying was successful when the number of exchange cycles was 15 times. After 10 cycles dry ice formed on a board at the outlet of the CPD, indicating that the content of the CPD sample chamber was mainly  $\text{CO}_2$ . Five additional exchange cycles were done to be sure that traces of acetone and ethanol were removed. The last traces could be difficult to remove because of capillary forces that trap small quantities in ‘necks’ around the particles.

Figure 6.5 shows a  $10 \times 8$  pattern of particles positioned on glass with a separation of  $9.9\ \mu\text{m}$ . On the left, the pattern was still soaked in ethanol. Critical point drying perfectly preserved the pattern. No particles were displaced or removed from the substrate and no additional particles attached to the surface.

Another method to remove ethanol without destroying the structure was to coat the pattern with a thin layer of silica. A layer of 15 nm was thick enough to attach the particles so strongly to the substrate that surface tension forces at the gas-liquid interface did not displace the particles. This is illustrated in Figure 6.6. Growing a protective layer of silica over the template is less labor-intensive than critical point drying. It has, however, the disadvantage that besides particles present from the trapping dispersion, small particles added to control the layer thickness are attached to the substrate. On the template in Figure 6.6b only one such particle, indicated by the arrow, was present, but often their number was much higher. These small seed particles will also influence the electric field pattern.



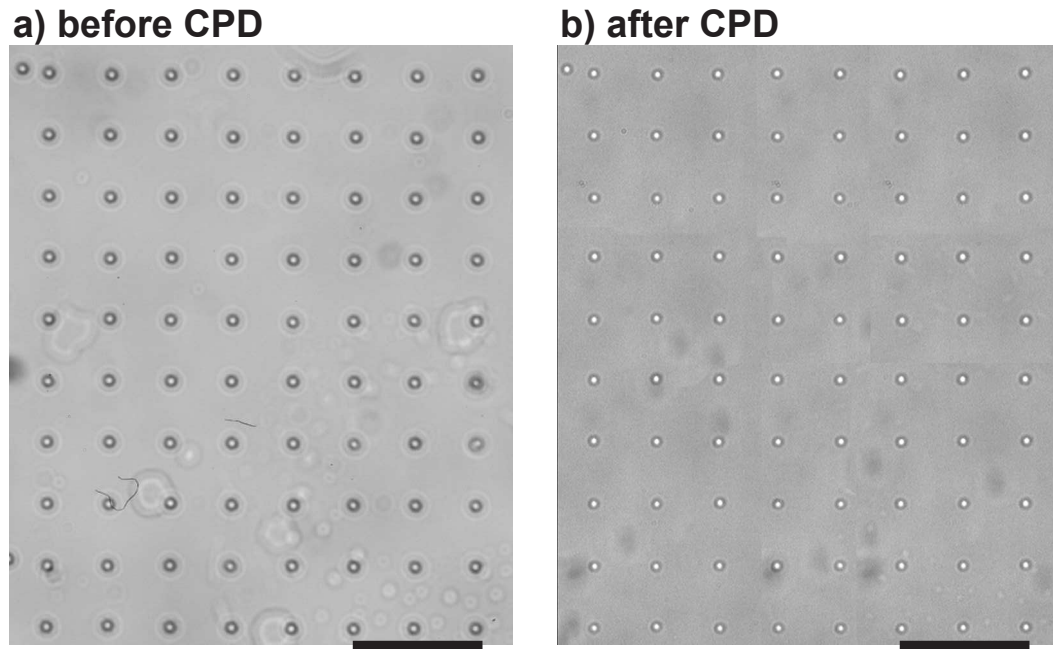


**Figure 6.5:** Pattern of  $1.2\ \mu\text{m}$  diameter silica particles that were positioned on a glass substrate by means of optical tweezers a) before and b) after critical point drying. The particles were placed  $9.9\ \mu\text{m}$  apart. The scale bars are  $20\ \mu\text{m}$ .

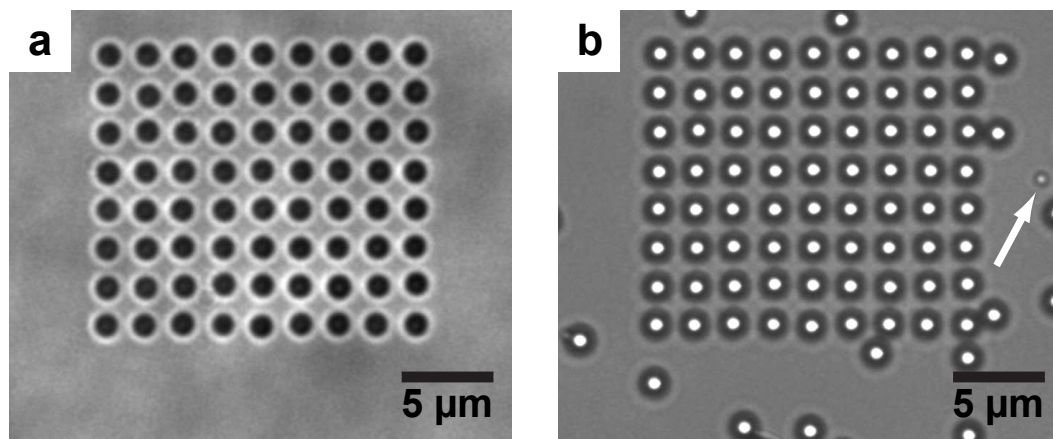


**Figure 6.6:** Pattern of  $1.2\ \mu\text{m}$  diameter silica particles positioned on a glass slide by means of optical tweezers can be protected from the destroying forces of surface tension forces by growing a layer of silica over it. The particles were placed  $2.1\ \mu\text{m}$  apart. The arrow indicates one of the small seed particles that were used to control the thickness of the grown layer.



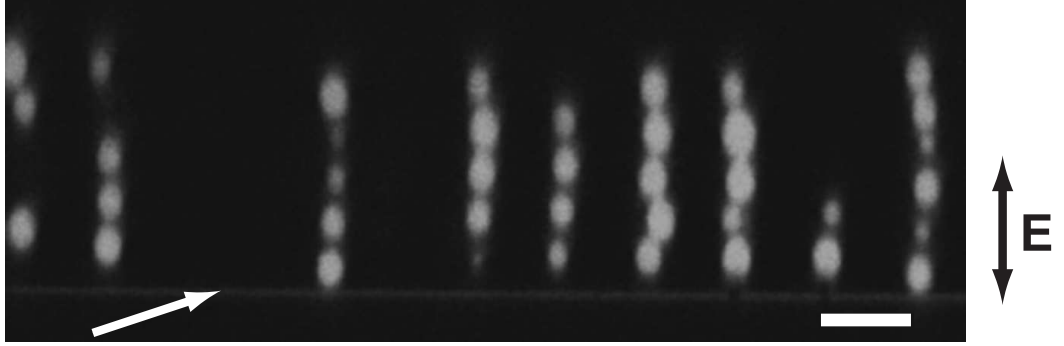


**Figure 6.7:**  $xz$ -confocal microscopy image of PMMA particles in *cis*-decalin. In an AC field with  $E_{rms} = 0.35$  kV/mm strings formed. The bottom plate carried a template of particles spaced  $9.9 \mu\text{m}$ . The strings formed on top of this template. The arrow points at the only site in this plane on top of which no string formed. The scale bar is  $10 \mu\text{m}$ .

#### 6.4.2 Guiding the attachment of dipolar particle strings

##### Particles with $\epsilon_p$ higher than $\epsilon_m$ of the medium

Before the  $3.34 \mu\text{m}$  diameter PMMA particles had sedimented in the *cis*-decalin, the electric field was quickly ramped up to  $E_{rms} = 0.35$  kV/mm. Immediately, strings of particles formed, some of which spanned the complete gap. The bottom electrode contained a regular pattern of silica particles over which metal was deposited and the strings formed right on top of this template at a regular spacing equal to the spacing of the particles of the template (Figure 6.7). The electric field strength is higher at the metal covered particles. PMMA has a higher dielectric constant than the medium and in a non-uniform electric field the dielectrophoretic force pushes the particles towards the particles forming the template. To determine whether a string of particles formed on top of every particle of the template, images were taken in the  $xy$ -plane at different heights between the electrodes (Figure 6.8). The template was the one shown in Figure 6.5. On top of almost every site of the template a string of PMMA particles formed. Higher in the sample the template became less recognizable. Most but not all strings were electrode spanning and the closer the top electrode was approached the more positions of the template were unfilled. Strings may also be not exactly parallel to the field lines, but may wiggle. This causes deviations from the template. Especially on the right side of the images several touching particles are present. Apparently, at this field strength and volume fraction sheets and single strings coexist.

This mechanism to form strings on a template also holds for other systems, provided that the particles have a higher dielectric constant than the medium. An example is a dispersion of silica particles in ethoxylated trimethylolpropane triacrylate (ETPTA). On the template shown in Figure 6.9a strings

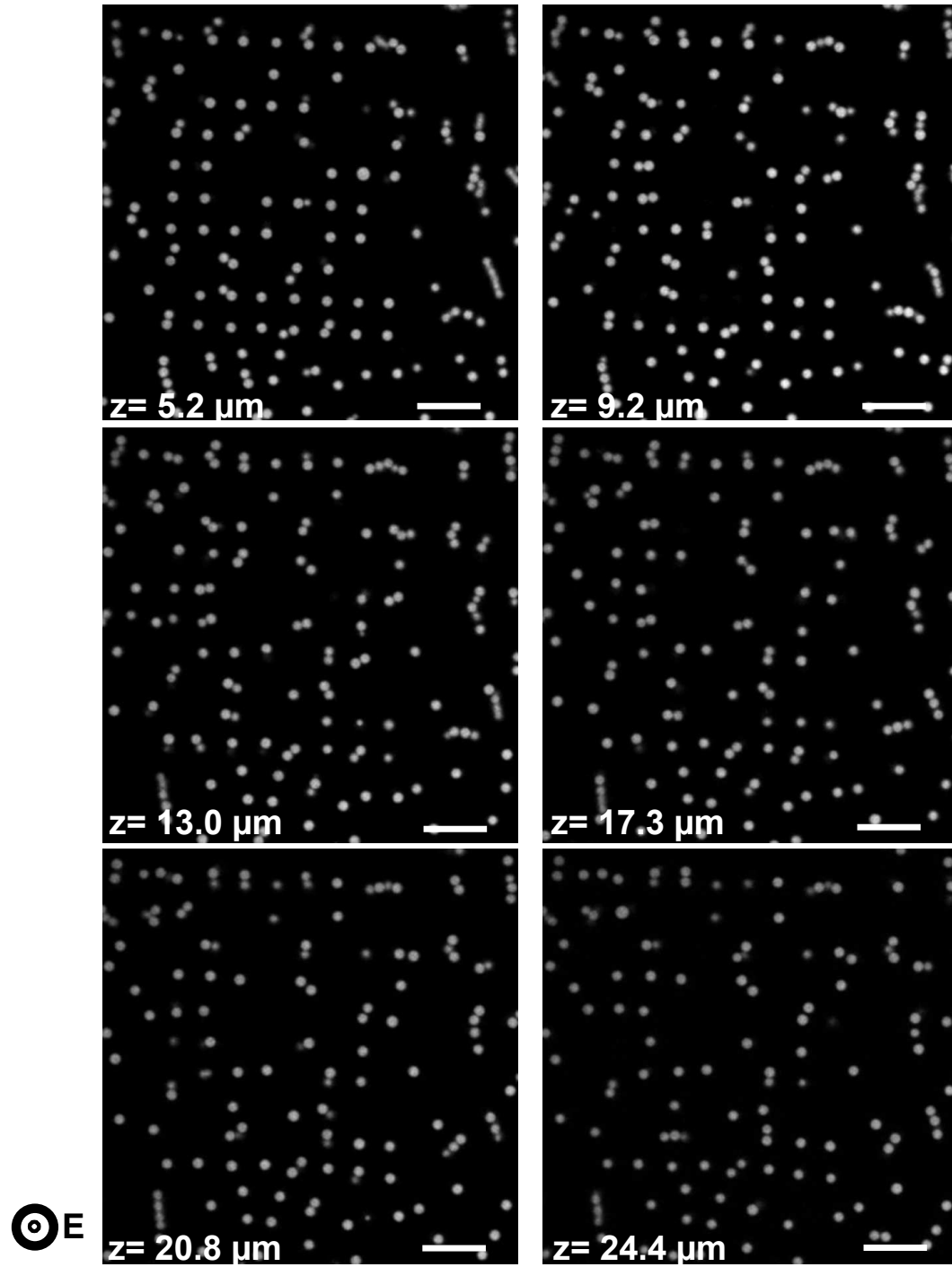


**Figure 6.8:** In *cis*-decalin  $3.34\ \mu\text{m}$  diameter PMMA particles in an AC field with  $E_{rms} = 0.35\ \text{kV/mm}$  formed strings. Confocal microscopy images taken at different positions along the electric field (starting at the bottom) show that they formed on top of the template on the bottom electrode. The template was the template shown in Figure 6.5 and consisted of  $10 \times 8$  particles positioned  $9.9\ \mu\text{m}$  apart. The electrode spacing was  $28\ \mu\text{m}$ . The scale bars are  $20\ \mu\text{m}$ .

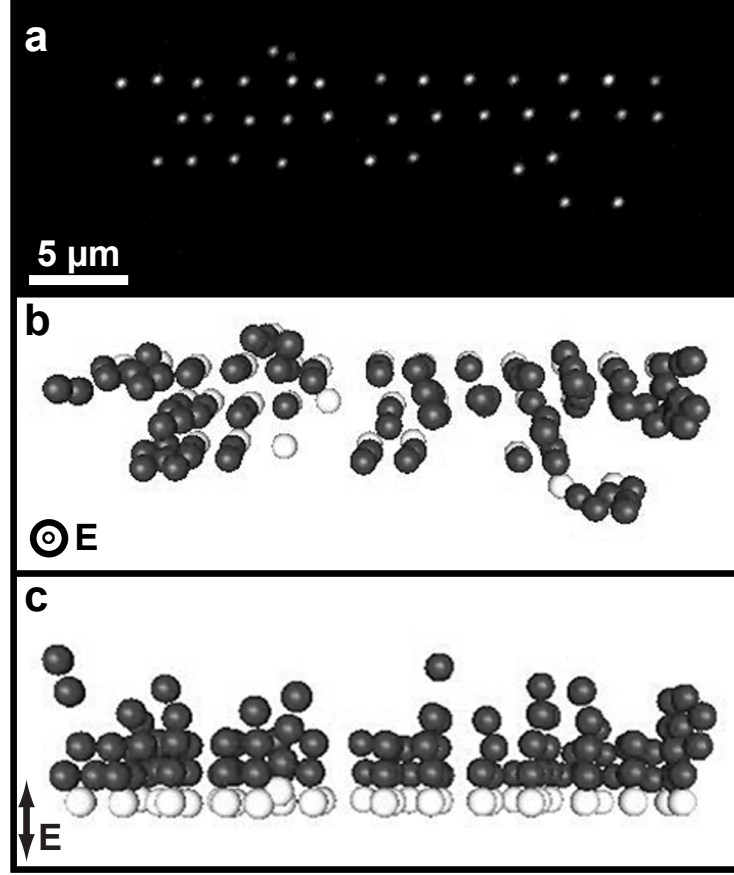


**Figure 6.9:** Silica particles dispersed in ETPTA tend to go to regions of higher field strength. a) Confocal micrograph of the particles of the template that were separated by  $2.1 \mu\text{m}$ . A top (b) and side (c) view reconstructed from the particle coordinates, show that the silica particles in the dispersion formed strings on top of this template. Consecutive particles in one strings were touching each other.

of silica particles formed (Figure 6.9b and c). The applied electric field was  $E_{rms} \approx 0.71 \text{ kV/mm}$ . The strings of silica particles in ETPTA were not electrode spanning, whereas those of PMMA particles in *cis*-decalin were. The polarizability,  $\beta$ , of silica in ETPTA is twice as large as that of PMMA in *cis*-decalin. The induced dipole moment of our silica particles was, however, much smaller than that of the used PMMA particles. The induced dipole moment is proportional to  $\sigma^3$ . The PMMA particles were  $3.34 \mu\text{m}$  in diameter and the silica particles  $1.2 \mu\text{m}$ . The induced dipole moment of the PMMA particles in *cis*-decalin was, thus, 7 times as large as that of the silica particles in ETPTA. Much higher field strengths were therefore needed to form strings and even higher fields to form electrode spanning strings. A disadvantage of such high field strengths is that at high local volume fractions a body centered tetragonal structure is the thermodynamically stable structure [43]. The strings will

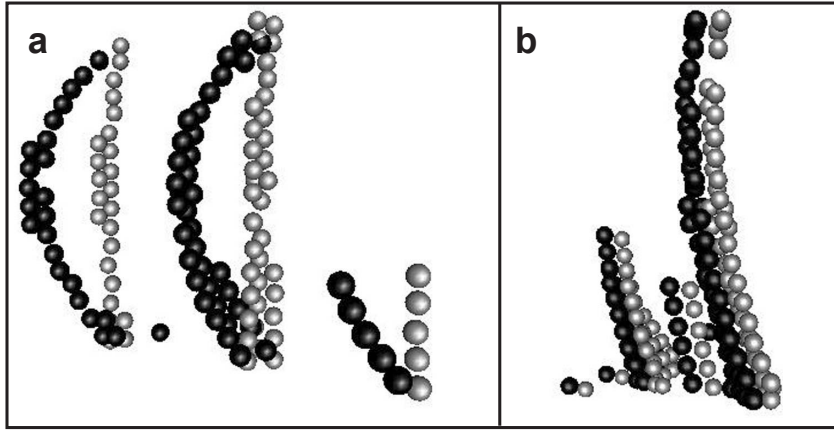


**Figure 6.10:** Computer generated reconstructions of the structure before (light grey) and after (black) polymerization of the medium. The coordinates were extracted from confocal images using algorithms similar to those used by Crocker and Grier [104], but extended to 3D as described in Reference [43]. a) When the intensity of the light was too high, polymerization was so fast that the structures deformed. b) When the light was attenuated by a 1 mm microscope slide that transmitted only 55% of light with a wavelength of 254 nm, polymerization took about 1 minute. This was slow enough to prevent the structure from deforming. The coordinates of the particles after drying are shifted by 2  $\mu\text{m}$  for clarity.

attract each other and not follow the template any more. The system of silica in ETPTA has, however, the advantage that the structures can be fixed by polymerizing the medium by illumination with UV light. In Chapter 3 we showed that crystal structures do not deform during polymerization, but also in dilute systems with only strings our experiments show that no deformations occur provided that the polymerization rate is low. Figure 6.10 shows electric field induced strings before polymerization with the field on (light grey spheres) and after polymerization and after switching off the field (dark grey spheres). Figure 6.10a also shows that shear can be used on top of the method demonstrated in this chapter to give additional control over structures before polymerization.

#### Particles with $\epsilon_p$ lower than $\epsilon_m$ of the medium

PMMA particles have a lower dielectric constant than CHB and Equation 6.3 predicts that they go to regions of lower electric field strength. PMMA particles in CHB acquire a charge and show long range Coulombic repulsion [44] making the strings repel each other. The template was adapted to this situation and the particles on the electrode were placed 9.7  $\mu\text{m}$  apart from each other. In Figure 6.11 circles indicate their position.

When an alternating current electric field was quickly ramped from zero to  $E_{rms} = 0.35 \text{ kV/mm}$  electrode spanning strings formed. In this system, the

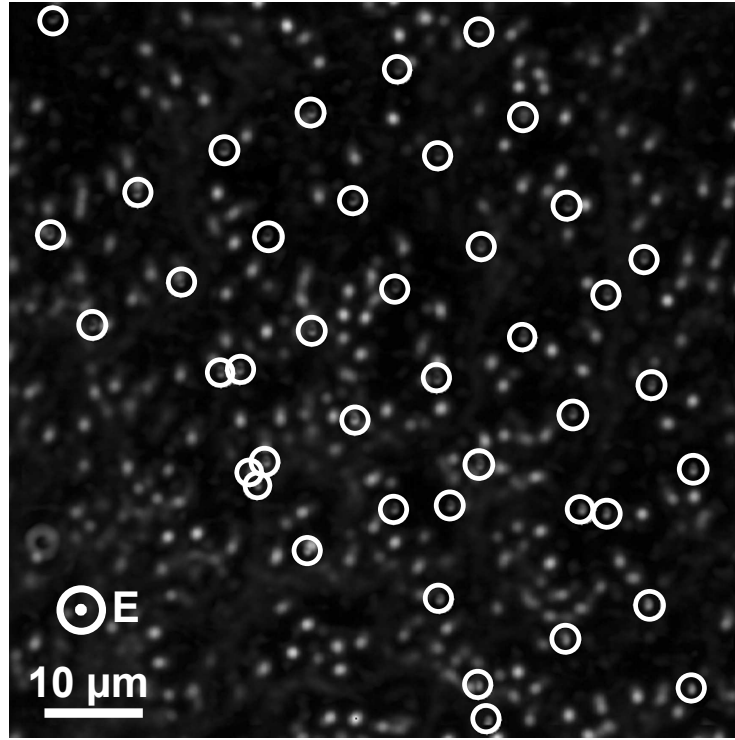


**Figure 6.11:** A projection of all particles on the plane perpendicular to the electric field direction shows that PMMA particles in CHB formed structures that were not on top of the template on the electrode. The circles indicate the particles of the template.

strings did not form on top of the template where the electric field strength was locally higher, but rather in between. This is in agreement with the theory that particles with a dielectric constant lower than that of the suspending medium go to lower field strength regions. And it can also be used in directing structures.

## 6.5 Conclusion and outlook

We have shown that it is possible to manipulate structure formation in all three dimensions using a locally non-uniform electric field on top of one of the electrodes. One of the electrodes of a parallel plate capacitor was patterned by placing micron-sized silica particles one by one with optical tweezers in a regular pattern on a glass substrate. To make the patterned substrate conductive, it was either coated with indiumtin oxide (ITO) before positioning the particles or coated with a 10-nm layer of gold after conserving the pattern of particles. To dry the structures without them being destroyed by surface tension forces that occur when a gas-liquid interface passes by, the structures were dried by critical point drying or protected from these forces by growing a silica layer of

at least 15 nm over it.

By choosing the components of the colloidal system such that the dielectric constant of the particles was either higher or lower than that of the solvent, the particles were attracted to or repelled from the template. Although this was not used yet, these two effects could be made to reinforce the formation of desired structures. PMMA particles in cyclohexylbromide (CHB) or silica particles in DMSO went to regions with a lower field strength, away from features created on the template. PMMA particles in *cis*-decalin or silica in ethoxylated trimethylolpropane triacrylate (ETPTA) went towards higher field regions. Strings formed on top of the template. Strings of PMMA in *cis*-decalin even were electrode spanning.

It has been shown before [44] that the spacing in the electric field direction in solvents such as CHB can be dramatically tuned from touching spheres to separations of many micrometers by simply changing the ionic strength. Although our results are preliminary, it is clear that orienting 3D structure formation of dipolar strings in this way allows for much larger structures and better control over particle positions than the methods previously used [179, 180, 194]. It has recently been shown that PbSe nanocrystals have a permanent dipole moment [195–197]. Therefore, even without an external field these quasi-spherical particles form chains [197]. A system of PbSe nanocrystals may also be used to fabricate strings that nucleate on a template. By combining electrically induced structure formation and shear, even more crystal structures are expected to be made.

## Acknowledgements

First of all, Dirk Vossen and Astrid van der Horst are thanked for instructing us how to make patterns with optical tweezers. We would like to thank Chris Schneijdenberg (Celbiologie, Utrecht University) for allowing us to perform critical point drying experiments with their apparatus when ours was broken. We further thank Hans Meeldijk (Electron Microscopy, Utrecht) for the use of the sputter coater. Christina Christova is acknowledged for experiments in which we observed that strings of PMMA particles nucleated on top of particles that were accidentally stuck to one of the electrodes. Furthermore, Mirjam Leunissen is thanked for instructing us how to make the electric field cells and for synthesizing the 1.4  $\mu\text{m}$  NBD-PMMA particles. Andrew Campbell is acknowledged for synthesizing the 3.34  $\mu\text{m}$  Nile-Red-PMMA particles. Finally, we thank Michiel Hermes, Job Thijssen and Esther Vermolen for helpful discussions.





# References

- [1] R. Brown. A brief account of microscopical observations made in the months of June, July and August, 1827, on the particles contained in the pollen of plants; and on the general existence of active molecules in organic and inorganic bodies. *Philosophical Magazine*, 4:161, 1828.
- [2] A. Brongniart. Mémoire sur la génération et le développement de l'embryon dans les végétaux phanérogames. *Annales des Sciences Naturelles*, 12:14, 1827.
- [3] M.D. Haw. Colloidal suspensions, Brownian motion, molecular reality: a short history. *Journal of Physics: Condensed Matter*, 14:7769, 2002.
- [4] W.G. Hoover and F.H. Ree. Melting transition and communal entropy for hard spheres. *Journal of Chemical Physics*, 49:3609, 1968.
- [5] P.N. Pusey and W. van Megen. Phase behaviour of concentrated suspensions of nearly hard colloidal spheres. *Nature*, 320:340, 1986.
- [6] C.M. Soukoulis. *Photonic crystals and light localization in the 21st century*. Kluwer Academic Publishers, 2001.
- [7] J.P. Hoogenboom, P. Vergeer, and A. van Blaaderen. A real-space analysis of colloidal crystallization in a gravitational field at a flat bottom wall. *Journal of Chemical Physics*, 119:3371, 2003.
- [8] A. Yethiraj, J.H.J. Thijssen, A. Wouterse, and A. van Blaaderen. Large-area electric-field-induced colloidal single crystals for photonic applications. *Advanced Materials*, 16:596, 2004.
- [9] B.J. Ackerson and P.N. Pusey. Shear-induced order in suspensions of hard spheres. *Physical Review Letters*, 61:1033, 1988.
- [10] M.D. Haw, W.C.K. Poon, and P.N. Pusey. Direct observation of oscillatory-shear-induced order in colloidal suspensions. *Physical Review E*, 57:6859, 1998.
- [11] T. Sawada, Y. Suzuki, A. Toyotama, and N. Iyi. Quick fabrication of gigantic single-crystalline colloidal crystals for photonic crystal applications. *Japanese Journal of Applied Physics*, 40:L1226, 2001.
- [12] S.H. Park, D. Qin, and Y. Xia. Crystallization of mesoscale particles over large areas. *Advanced Materials*, 10:1028, 1998.
- [13] T. Kanai, T. Sawada, A. Toyotama, and K. Kitamura. Air-pulse-drive fabrication of photonic crystal films of colloids with high spectral quality. *Advanced Functional Materials*, 15:25, 2005.
- [14] R.M. Amos, T.J. Sheperd, J.G. Rarity, and P. Tapster. Shear-ordered face-centered cubic photonic crystals. *Electronics Letters*, 36:1411, 2000.
- [15] R.M. Amos, J.G. Rarity, P.R. Tapster, and T.J. Shepherd. Fabrication of large-area face-centered-cubic hard-sphere colloidal crystals by shear alignment. *Physical Review E*, 61:2929, 2000.

- [16] R.M. Amos, D.M. Taylor, T.J. Shepherd, J.G. Rarity, and P. Tapster. Tunable shear-ordered face-centered cubic photonic crystals. In C.M. Soukoulis, editor, *Photonic crystals and light localization in the 21st century*, pages 263–278. Kluwer Academic Publisher, 2001.
- [17] I. Cohen, T.G. Mason, and D.A. Weitz. Shear-induced configurations of confined colloidal suspensions. *Physical Review Letters*, 93:046001, 2004.
- [18] T. Ruhl and G.P. Hellmann. Colloidal crystals in latex films: rubbery opals. *Macromolecular Chemistry and Physics*, 2002:3502, 2001.
- [19] T. Ruhl, P. Spahn, and G.P. Hellmann. Artificial opals prepared by melt compression. *Polymer*, 44:7625, 2003.
- [20] T. Ruhl, P. Spahn, H. Winkler, and G.P. Hellmann. Large area monodomain order in colloidal crystals. *Macromolecular Chemistry and Physics*, 205:1385, 2004.
- [21] P. Jiang and M.J. McFarland. Large-scale fabrication of wafer-size colloidal crystals, macroporous polymers and nanocomposites by spin-coating. *Journal of the American Chemical Society*, 126:13778, 2004.
- [22] P. Jiang and M.J. McFarland. Wafer-scale periodic nanohole arrays templated from two-dimensional nonclose-packed colloidal crystals. *Journal of the American Chemical Society*, 127:3710, 2005.
- [23] P. Jiang, T. Prasad, M.J. McFarland, and V.L. Colvin. Two-dimensional nonclose-packed colloidal crystals formed by spincoating. *Applied Physics Letters*, 89:011908, 2006.
- [24] M. Tomita and T.G.M. van de Ven. The structure of sheared ordered lattices. *Journal of Colloid and Interface Science*, 99:374, 1984.
- [25] L.B. Chen, C.F. Zukoski, B.J. Ackerson, H.J.M. Hanley, G.C. Straty, J. Barker, and C.J. Glinka. Structural changes and orientational order in a sheared colloidal suspension. *Physical Review Letters*, 69:688, 1992.
- [26] P. Holmqvist, M.P. Lettinga, J. Buitenhuis, and J.K.G. Dhont. Crystallization kinetics of colloidal spheres under stationary shear flow. *Langmuir*, 21:10976, 2005.
- [27] J. Vermant and M.J. Solomon. Flow-induced structure in colloidal suspensions. *Journal of Physics: Condensed Matter*, 17:R187, 2005.
- [28] E.J. Stancik, G.T. Gavranovic, M.J.O. Widenbrant, A.T. Laschitsch, J. Vermant, and G.G. Fuller. Structure and dynamics of particle monolayers at a liquid-liquid interface subjected to shear flow. *Faraday Discussions*, 123:145, 2003.
- [29] E.J. Stancik, A.L. Hawkinson, J. Vermant, and G.G. Fuller. Dynamic transitions and oscillatory melting of a two-dimensional crystal subjected to shear flow. *Journal of Rheology*, 48:159, 2004.
- [30] V.A. Tolpekin, M.H.G. Duits, D. van den Ende, and J. Mellema. Aggregation and breakup of colloidal particle aggregates in shear flow, studied with video microscopy. *Langmuir*, 20:2614, 2004.
- [31] M. Minsky. Memoir on inventing the confocal scanning microscope. *Scanning*, 10:128, 1988.

- [32] A. van Blaaderen and P. Wiltzius. Real-space structure of colloidal hard-sphere glasses. *Science*, 270:1177, 1995.
- [33] T. Solomon and M.J. Solomon. Stacking fault structure in shear-induced colloidal crystallization. *Journal of Chemical Physics*, 124:134905, 2006.
- [34] D. Derks, H. Wisman, A. van Blaaderen, and A. Imhof. Confocal microscopy of colloidal dispersions in shear flow using a counter-rotating cone-plate shear cell. *Journal of Physics: Condensed Matter*, 16:S3917, 2004.
- [35] G.I. Taylor. *Proceedings of the Royal Society London*, 29:501, 1934.
- [36] N. Grizzuti and O. Bifulco. Effects of coalescence and breakup on the steady state morphology of an immiscible polymer blend in shear flow. *Rheologica Acta*, 36:406, 1997.
- [37] K.H. de Haas, D. van den Ende, C. Blom, E.G. Altena, G.J. Beukema, and J. Mellema. A counter-rotating Couette apparatus to study deformation of a sub-millimeter sized particle in shear flow. *Review of Scientific Instruments*, 39:1391, 1998.
- [38] V. Breedveld, D. van den Ende, M. Bosscher, R.J.J. Jongschaap, and J. Mellema. Measuring shear-induced self-diffusion in a counterrotating geometry. *Physical Review E*, 63:021403, 2001.
- [39] A.L. Rogach, N.A. Kotov, D.S. Koktysh, J.W. Ostrander, and G.A. Ragoisha. Electrophoretic deposition of latex-based 3D colloidal photonic crystals: a technique for rapid production of high-quality opals. *Chemistry of Materials*, 12:2721, 2000.
- [40] T. C. Halsey and W. Toor. Structure of electrorheological fluids. *Physical Review Letters*, 65:2820, 1990.
- [41] R. Tao and J.M. Sun. Three-dimensional structure of induced electrorheological solid. *Physical Review Letters*, 67:398, 1991.
- [42] R. Tao and Q. Jiang. Simulation of structure formation in an electrorheological fluid. *Physical Review Letters*, 73:205, 1994.
- [43] U. Dassanayake, S. Fraden, and A. van Blaaderen. Structure of electrorheological fluids. *Journal of Chemical Physics*, 112:3851, 2000.
- [44] A. Yethiraj and A. van Blaaderen. A colloidal model system with an interaction tunable from hard-sphere to soft and dipolar. *Nature*, 421:513, 2003.
- [45] M. Sullivan, K. Zhao, C. Harrison, R.H. Austin, M. Megens, A. Hollingsworth, W.B. Russel, Z. Cheng, T. Mason, and P.M. Chaikin. Control of colloids with gravity, temperature gradients, and electric fields. *Journal of Physics: Condensed Matter*, 15:S11, 2003.
- [46] M.T. Sullivan, K. Zhao, A.D. Hollingsworth, R.H. Austing, W.B. Russel, and P.M. Chaikin. An electric bottle for colloids. *Physical Review Letters*, 96:015703, 2006.
- [47] M.E. Leunissen. *Manipulating colloids with charges and electric fields*. PhD thesis, Utrecht University, 2007.
- [48] A. Ashkin. Acceleration and trapping of particles by radiation pressure. *Physical Review Letters*, 24:156, 1970.

- [49] A. Ashkin, J.M. Dziedzic, J.E. Bjorkholm, and S. Chu. Observation of a single-beam gradient force optical trap for dielectric particles. *Optics Letters*, 11:288, 1986.
- [50] A. Ashkin. Optical trapping and manipulation of neutral particles using lasers. *Proceedings of the National Academy of Sciences*, 94:4853, 1997.
- [51] S.A. Asher, J. Holtz, L. Liu, and Z. Wu. Self-assembly motif for creating submicron periodic materials. Polymerized crystalline colloidal arrays. *Journal of the American Chemical Society*, 116:4997, 1994.
- [52] Y. Iwayama, J. Yamanaka, Y. Takiguchi, M. Takasaka, K. Ito, T. Shinohara, T. Sawada, and M. Yonese. Optically tunable gelled photonic crystal covering almost the entire visible light wavelength region. *Langmuir*, 19:977, 2003.
- [53] S.H. Foulger, P. Jiang, A.C. Lattam, D.W. Smith, Jr. J. Ballato, D.E. Dausch, S. Grego, and B.R. Stoner. Photonic crystal composites with reversible high-frequency stop band shifts. *Advanced Materials*, 15:685, 2003.
- [54] A.C. Arsenault, T.J. Clark, L. von Freymann, G. Cademartiri, R. Sapienza, J. Bertolotti, E. Vekris, S. Wong, V. Kitaev, I. Manners, R.Z. Wang, S. John, D. Wiersma, and G.A. Ozin. From colour fingerprinting to the control of photoluminescence in elastic photonic crystals. *Nature Materials*, 5:179, 2006.
- [55] H. Löwen. Colloidal soft matter under external control. *Journal of Physics: Condensed Matter*, 13:R415, 2001.
- [56] B.J. Ackerson and N.A. Clark. Shear-induced melting. *Physical Review Letters*, 46:123, 1981.
- [57] I.W. Hamley, J.A. Pople, C. Booth, Y.-W. Yang, and S.M. King. A small-angle neutron-scattering study of shear-induced ordering in the cubic phase of a block copolymer gel. *Langmuir*, 14:3182, 1998.
- [58] Y.D. Yan, J.K.G. Dhont, C. Smits, and H.N.W. Lekkerkerker. Oscillatory-shear-induced order in nonaqueous dispersions of charged colloidal spheres. *Physica A*, 202:68, 1994.
- [59] M.J. Stevens and M.O. Robbins. Simulations of shear-induced melting and ordering. *Physical Review E*, 48:3778, 1993.
- [60] D.E. Smith, H.P. Babcock, and S. Chu. Single-polymer dynamics in steady shear flow. *Science*, 283:1724, 1999.
- [61] B.J. Ackerson and N.A. Clark. Shear-induced partial translational ordering of a colloidal solid. *Physical Review A*, 30:906, 1984.
- [62] J.-F. Berret, D.C. Roux, G. Porte, and P. Lindner. Shear-induced isotropic-to-nematic phase transition in equilibrium polymers. *Europhysics Letters*, 25:521, 1994.
- [63] O. Volkova, S. Cutillas, and G. Bossis. Shear banded flows and nematic-to-isotropic transition in ER and MR fluids. *Physical Review Letters*, 82:233, 1999.
- [64] M.P. Lettinga, K.O. Kang, P. Holmqvist, A. Imhof, D. Derks, and J.K.G. Dhont. Nematic-isotropic spinodal decomposition kinetics of rodlike viruses. *Physical Review E*, 73:011412, 2006.

- [65] R.G. Larson. *The structure and rheology of complex fluids*. Oxford University Press, Oxford, 1999.
- [66] Ch. Münch and J. Kalus. New shear apparatus for in situ small-angle X-ray scattering experiments. *Review of Scientific Instruments*, 70:187, 1999.
- [67] P. Panine, M. Gradzielski, and T. Narayanan. Combined rheometry and small-angle X-ray scattering. *Review of Scientific Instruments*, 74:2451, 2003.
- [68] L. Porcar, W.A. Hamilton, P.D. Butler, and G.G. Warr. A vapor barrier Couette shear cell for small angle neutron scattering measurements. *Review of Scientific Instruments*, 73:2345, 2002.
- [69] E. Eiser, F. Molino, and G. Porte. Nonhomogeneous textures and banded flow in a soft cubic phase under shear. *Physical Review E*, 61:6759, 2000.
- [70] M. Kisilak, H. Anderson, N.S. Babcock, M.R. Stetzer, S.H.J. Idziak, and E.B. Sirota. An X-ray extensional flow cell. *Review of Scientific Instruments*, 72:4305, 2001.
- [71] S. Ashdown, I. Marković, R.H. Ottewill, P. Lindner, R.C. Oberthür, and A.R. Rennie. Small-angle neutron-scattering studies on ordered polymer colloid dispersions. *Langmuir*, 6:303, 1990.
- [72] P. Baroni, C. Pujolle-Robic, and L. Noirez. Integrated neutron Couette system for nonequilibrium studies of polymers under flow. *Review of Scientific Instruments*, 72:2686, 2001.
- [73] D. Beysens, M. Gbadamassi, and L. Boyer. Light-scattering study of a critical mixture of shear flow. *Physical Review Letters*, 43:1253, 1979.
- [74] J.W. van Egmond, D.E. Werner, and G.G. Fuller. Time-dependent small-angle light scattering of shear-induced concentration fluctuations in polymer solutions. *Journal of Chemical Physics*, 96:7742, 1992.
- [75] J. Läger and W. Gronski. A melt rheometer with integrated small angle light scattering. *Rheologica Acta*, 34:70, 1995.
- [76] M. Paques, A. Imhof, A. van Blaaderen, and Y. Nicolas. *Method and device for imaging the dynamic behaviour of microstructures under the influence of deformation*. European Patent Application, 2001.
- [77] T. Palberg and R. Biehl. Sheared colloidal crystals in confined geometry: a real space study on stationary structures under shear. *Faraday Discussions*, 123:1, 2002.
- [78] R. Biehl and T. Palberg. Real space and Fourier microscopy of colloidal suspensions confined to a parallel plate geometry. *Review of Scientific Instruments*, 75:906, 2004.
- [79] Y. Nicolas, M. Paques, A. Knaebel, A. Steyer, J.P. Münch, T.B.J. Blijdenstein, and G.A. van Aken. Microrheology: Structural evolution under static and dynamic conditions by simultaneous analysis of confocal microscopy and diffusing wave spectroscopy. *Review of Scientific Instruments*, 74:3838, 2003.
- [80] A. van Blaaderen. Quantitative real-space analysis of colloidal structures and dynamics with confocal scanning light microscopy. *Progress in Colloid and Polymer Science*, 104:59, 1997.

- [81] W.K. Kegel and A. van Blaaderen. Direct observation of dynamical heterogeneities in colloidal hard-sphere suspensions. *Science*, 287:290, 2000.
- [82] U. Gasser, E.R. Weeks, A. Schofield, P.N. Pusey, and D.A. Weitz. Real-space imaging of nucleation and growth in colloidal crystallization. *Science*, 292:258, 2001.
- [83] W. Stöber, A. Fink, and E. Bohn. Controlled growth of monodisperse silica spheres in the micron size range. *Journal of Colloid and Interface Science*, 26:62, 1968.
- [84] A. van Blaaderen and A. Vrij. Synthesis and characterization of colloidal dispersions of fluorescent, monodisperse silica spheres. *Langmuir*, 8:2921, 1992.
- [85] J. Vermant. Large-scale structures in sheared colloidal dispersions. *Current Opinion in Colloid and Interface Science*, 6:489, 2001.
- [86] N.A. Spenley, M.E. Cates, and T.C.B. McLeish. Nonlinear rheology of worm-like micelles. *Physical Review Letters*, 71:939, 1993.
- [87] R.W. Mair and P.T. Callaghan. Observation of shear banding in worm-like micelles by NMR velocity imaging. *Europhysics Letters*, 36:719, 1996.
- [88] M.M. Britton and P.T. Callaghan. Two-phase shear band structures at uniform stress. *Physical Review Letters*, 26:930, 1997.
- [89] J.B. Salmon, A. Colin, S. Manneville, and F. Molino. Velocity profiles in shear-banding wormlike micelles. *Physical Review Letters*, 90:228303, 2003.
- [90] A. Imhof, A. van Blaaderen, and J.K.G. Dhont. Shear melting of colloidal crystals of charged spheres studied with rheology and polarizing microscopy. *Langmuir*, 10:3477, 1994.
- [91] J.K.G. Dhont, M.P. Lettinga, Z. Dogic, T.A.J. Lenstra, H. Wang, S. Rathgeber, P. Carletto, L. Willner, H. Freilinghaus, and P. Lindner. Shear-banding and microstructure of colloids in shear flow. *Faraday Discussions*, 123:157, 2003.
- [92] L.B. Chen and C.F. Zukoski. Discontinuous shear thinning in ordered suspensions. *Physical Review Letters*, 65:44, 1990.
- [93] L.B. Chen, B.J. Ackerson, and C.F. Zukoski. Rheological consequences of microstructural transitions in colloidal crystals. *Journal of Rheology*, 38:193, 1994.
- [94] B.J. Ackerson, J.B. Hayter, N.A. Clark, and L. Cotter. Neutron scattering from charge stabilized suspensions undergoing shear. *Journal of Chemical Physics*, 84:2344, 1986.
- [95] B.J. Ackerson. Shear induced order and shear processing of model hard sphere suspensions. *Journal of Rheology*, 34:553, 1990.
- [96] M.J. Stevens, M.O. Robbins, and J.F. Belak. Shear melting of colloids: a nonequilibrium phase diagram. *Physical Review Letters*, 66:3004, 1991.
- [97] R.L. Hoffman. Discontinuous and dilatant viscosity behavior in concentrated suspensions. II. theory and experimental tests. *Journal of Colloid and Interface Science*, 46:491, 1974.
- [98] A. Tsuchida, E. Takyo, K. Taguchi, and T. Okubo. Kinetic analysis of colloidal crystallization in shear flow. *Colloid and Polymer Science*, 282:1105, 2004.



- [99] S. Butler and P. Harrowell. Kinetics of crystallization in a shearing colloidal suspension. *Physical Review E*, 52:6424, 1995.
- [100] S. Butler and P. Harrowell. The shear induced disordering transition in a colloidal crystal: nonequilibrium Brownian dynamic simulations. *Journal of Chemical Physics*, 103:4653, 1995.
- [101] R. Blaak, S. Auer, D. Frenkel, and H. Löwen. Crystal nucleation of colloidal suspensions under shear. *Physical Review Letters*, 93:068303, 2004.
- [102] P. Panine, T. Narayanan, J. Vermant, and J. Mewis. Structure and rheology during shear-induced crystallization of a latex suspension. *Physical Review E*, 66:022401 (4), 2002.
- [103] B.J. Ackerson. Shear induced order of hard sphere suspensions. *Journal of Physics: Condensed Matter*, 2:SA389, 1990.
- [104] J.C. Crocker and D.G. Grier. Methods of digital video microscopy for colloidal studies. *Journal of Colloid and Interface Science*, 179:298, 1996.
- [105] D. Derks. *Colloidal suspensions in shear flow- a real space study*. PhD thesis, Utrecht University, 2006.
- [106] L.B. Chen, M.K. Chow, B.J. Ackerson, and C.F. Zukoski. Rheological and structural transitions in colloidal crystals. *Langmuir*, 10:2817, 1994.
- [107] A.C. Dogariu and R. Rajagopalan. Optical traps as force transducers: The effects of focusing the trapping beam through a dielectric interface. *Langmuir*, 16:2770, 2000.
- [108] D.E. Bornside, R.A. Brown, P.W. Ackmann, J.R. Frank, A.A. Tryba, and F.T. Geyling. The effect of gas phase convection on mass transfer in spin coating. *Journal of Applied Physics*, 73:585, 1993.
- [109] I.M. Thomas. High laser damage threshold porous silica antireflective coating. *Applied Optics*, 25:1481, 1986.
- [110] I.M. Thomas. Single layer  $\text{Al}_2\text{O}_3\cdot\text{H}_2\text{O}$  and multilayer  $\text{Al}_2\text{O}_3\cdot\text{H}_2\text{O}\cdot\text{SiO}_2$  optical coatings prepared from colloidal suspensions. *Applied Optics*, 28:4013, 1989.
- [111] A.G. Emslie, F.T. Bonner, and L.G. Peck. Flow of a viscous liquid on a rotating disk. *Journal of Applied Physics*, 29:858, 1958.
- [112] B.D. Washo. Rheology and modeling of the spin coating process. *IBM Journal of Research and Development*, 21:190, 1977.
- [113] D. Meyerhofer. Characteristics of resist films produced by spinning. *Journal of Applied Physics*, 49:3993, 1978.
- [114] D.E. Bornside, C.W. Macosko, and L.E. Scriven. On the modeling of spin coating. *Journal of Imaging Technology*, 13:122, 1987.
- [115] S. Middleman. The effect of induced air-flow on the spin coating of viscous liquids. *Journal of Applied Physics*, 62:2530, 1987.
- [116] S.K. Wilson, R. Hunt, and B.R. Duffy. The rate of spreading in spin coating. *Journal of Fluid Mechanics*, 413:65, 2000.
- [117] A. Acrivos, M.J. Shah, and E.E. Petersen. On the flow of a non-Newtonian liquid on a rotating disk. *Journal of Applied Physics*, 31:963, 1960.



- [118] S.A. Jenekhe and S.B. Schuldt. Coating flow of non-Newtonian fluids on a flat rotating disk. *Industrial and Engineering Chemistry Fundamentals*, 23:432, 1984.
- [119] S. Matsumoto, Y. Takashima, T. Kamiya, A. Kayano, and Y. Ohita. Film thickness of a Bingham fluid on a rotating disk. *Industrial and Engineering Chemistry Fundamentals*, 21:198, 1982.
- [120] S. Coe-Sullivan, J. S. Steckel, W-K. Woo, M.G. Bawendi, and V. Bulovic. Large-area ordered quantum-dot monolayers via phase separation during spin-casting. *Advanced Functional Materials*, 15:1117, 2005.
- [121] A. Mihi, M. Ocaña, and H. Míguez. Oriented colloidal-crystal thin films by spin-coating microspheres dispersed in volatile media. *Advanced Materials*, 18:2244, 2006.
- [122] D.Y. Wang and H. Möhwald. Rapid fabrication of binary colloidal crystals by stepwise spin-coating. *Advanced Materials*, 16:244, 2004.
- [123] K.P. Velikov, C.G. Christova, R.P.A. Dullens, and A. van Blaaderen. Layer-by-layer growth of binary colloidal crystals. *Science*, 296:106, 2002.
- [124] G.A. Ozin and S.M. Yang. The race for the photonic chip: Colloidal crystal assembly in silicon wafers. *Advanced Functional Materials*, 11:95, 2001.
- [125] D. Xia and S.R.J. Brueck. A facile approach to directed assembly of patterns of nanoparticle using interference lithography and spin coating. *Nano Letters*, 2004.
- [126] D. Xia and S.R.J. Brueck. Lithographically directed deposition of silica nanoparticles using spin coating. *Journal of Vacuum Science and Technology B*, 22:3415, 2004.
- [127] P.H. Walker and J.G. Thompson. Some physical properties of paints. *Proceedings/ Annual meeting American Society for testing and materials*, 22:464, 1922.
- [128] M.E. Leunissen, A. van Blaaderen, A.D. Hollingsworth, M.T. Sullivan, and P.M. Chaikin. Electrostatics at the oil-water interface, stability, and order in emulsions and colloids. *Proceedings of the National Academy of Sciences*, 104:2585, 2007.
- [129] Leica. Range of filtercubes. 2003.
- [130] J. Eichler, C.P. Herz, I. Naito, and W. Schnabel. Laser flash photolysis investigation of primary processes in the sensitized polymerization of vinyl monomers IV: experiments with hydroxy alkylphenones. *Journal of Photochemistry*, 12:225, 1980.
- [131] R.L. Hoffman. Discontinuous and dilatant viscosity behavior in concentrated suspensions. I. observation of a flow instability. *Transactions of the Society of Rheology*, 16:155, 1972.
- [132] J.P. Hoogenboom. *Colloidal epitaxy, a real-space analysis*. PhD thesis, Utrecht University, 2002.
- [133] J.P. Hoogenboom, D. Derks, P. Vergeer, and A. van Blaaderen. Stacking faults in colloidal crystals grown by sedimentation. *Journal of Chemical Physics*, 117:11320, 2002.

- [134] W. Li, T. Fu, and S. He. Preparation of free-standing silica 3D colloidal crystal film at water-air interface. *Materials Science and Engineering A*, 441:239, 2006.
- [135] P.N. Pusey, W. van Megen, P. Bartlett, B.J. Ackerson, J.G. Rarity, and S.M. Underwood. Structure of crystals of hard colloidal spheres. *Physical Review Letters*, 63:2753, 1989.
- [136] N.A.M. Verhaegh, J.S. van Duijneveldt, A. van Blaaderen, and H.N.W. Lekkerkerker. Direct observation of stacking disorder in a colloidal crystal. *Journal of Chemical Physics*, 102:1416, 1995.
- [137] P.J. Steinhardt, D.R. Nelson, and M. Ronchetti. Bond-orientational order in liquids and glasses. *Physical Review B*, 28:784, 1983.
- [138] P. Rein ten Wolde, M.J. Ruiz-Montero, and D. Frenkel. Numerical calculation of the rate of crystal nucleation in a Lennard-Jones system at moderate undercooling. *Journal of Chemical Physics*, 104:9932, 1996.
- [139] L.V. Woodcock. Entropy difference between the face-centered cubic and hexagonal close-packed crystal structures. *Nature*, 385:141, 1997.
- [140] S. Pronk and D. Frenkel. Can stacking faults in hard-sphere crystals anneal out spontaneously? *Journal of Chemical Physics*, 110:4589, 1999.
- [141] S.C. Mau and D.A. Huse. Stacking entropy of hard-sphere crystals. *Physical Review E*, 59:4396, 1999.
- [142] P. Pieranski, L. Strzelecki, and B. Pansu. Thin colloidal crystals. *Physical Review Letters*, 50:900, 1983.
- [143] D.H. Van Winkle and C.A. Murray. Layering transitions in colloidal crystals as observed by diffraction and direct-lattice imaging. *Physical Review A*, 34:562, 1986.
- [144] S. Naser, C. Bechinger, P. Leiderer, and T. Palberg. Finite-size effects on the closest packing of hard spheres. *Physical Review Letters*, 79:2348, 1997.
- [145] C.A. Murray. Phases of thin colloidal layers. *MRS Bulletin*, 23:33, 1998.
- [146] A.B. Fontecha, H.J. Schöpe, H. König, T. Palberg, R. Messina, and H. Löwen. A comparative study on the phase behaviour of highly charged colloidal spheres in a confining wedge geometry. *Journal of Physics: Condensed Matter*, 17:S2779, 2005.
- [147] M. Schmidt and H. Löwen. Freezing between two and three dimensions. *Physical Review Letters*, 76:4552, 1996.
- [148] J.A. Britten and I.M. Thomas. Non-Newtonian flow effects during spin coating large-area optical coatings with colloidal suspensions. *Journal of Applied Physics*, 71:972, 1992.
- [149] R.A. Robinson and R.H. Stokes. *Electrolyte solutions*. Butterworths scientific publications, London, 1955.
- [150] V.P. Bykov. Spontaneous emission from a medium with a band spectrum. *Soviet Journal of Quantum Electronics*, 4:861, 1975.
- [151] E. Yablonovitch. Inhibited spontaneous emission in solid-state physics and electronics. *Physical Review Letters*, 58:2059, 1987.

- [152] S. John. Strong localization of photons in certain disordered dielectric superlattices. *Physical Review Letters*, 58:2486, 1987.
- [153] P. Jiang, J.F. Bertone, K.S. Hwang, and V.L. Colvin. Single-crystal colloidal multilayers of controlled thickness. *Chemistry of Materials*, 11:2132, 1999.
- [154] A. van Blaaderen, R. Ruel, and P. Wiltzius. Template-directed colloidal crystallization. *Nature*, 385:321, 1997.
- [155] J.C. Hulthen and R.P. van Duyne. Nanosphere lithography: A materials general fabrication process for periodic particle array surfaces. *Journal of Vacuum Science and Technology A*, 13:1553, 1995.
- [156] Z.Z. Gu, A. Fujishima, and O. Sato. Fabrication of high-quality opal films with controllable thickness. *Chemistry of Materials*, 14:760, 2002.
- [157] M. Egen and R. Zentel. Tuning the properties of photonic films from polymer beads by chemistry. *Chemistry of Materials*, 14:2176, 2002.
- [158] A.A. Chabanov, Y. Jun, and D.J. Norris. Avoiding cracks in self-assembled photonic band-gap crystals. *Applied Physics Letters*, 84:3573, 2004.
- [159] F. García-Santamaría, H. Míguez, M. Ibisate, F. Meseguer, and C. López. Refractive index properties of calcined silica submicrometer spheres. *Langmuir*, 18:1942, 2002.
- [160] F. Pan, J. Zhang, C. Cai, and T. Wang. Rapid fabrication of large-area colloidal crystal monolayers by a vortical surface method. *Langmuir*, 22:7101, 2006.
- [161] S. Reculosa and S. Ravaine. Synthesis of colloidal crystals of controllable thickness through the Langmuir-Blodgett technique. *Chemistry of Materials*, 15:598, 2003.
- [162] S. Reculosa, P. Massé, and S. Ravaine. Three-dimensional colloidal crystals with a well-defined architecture. *Journal of Colloid and Interface Science*, 279:471, 2004.
- [163] K.M. Leung and Y.F. Liu. Full vector wave calculation of photonic band structures in face-centered-cubic dielectric media. *Physical Review Letters*, 65:2646, 1990.
- [164] H.S. Sozuer, J.W. Haus, and R. Inguva. Photonic bands - convergence problems with the plane-wave method. *Physical Review B*, 45:13962, 1992.
- [165] J. W. Haus, H. S. Sozuer, and R. Inguva. Photonic bands- ellipsoidal dielectric atoms in an FCC lattice. *Journal of Modern Optics*, 39:1991, 1992.
- [166] E. Snoeks, A. van Blaaderen, T. van Dillen, C.M. van Kats, M.L. Brongersma, and A. Polman. Colloidal ellipsoids with continuously variable shape. *Advanced Materials*, 12:1511, 2000.
- [167] T. van Dillen, A. Polman, W. Fukarek, and A. van Blaaderen. Energy-dependent anisotropic deformation of colloidal silica particles under MeV Au irradiation. *Applied Physics Letters*, 78:910, 2001.
- [168] K.P. Velikov, T. van Dillen, A. Polman, and A. van Blaaderen. Photonic crystals of shape-anisotropic colloidal particles. *Applied Physics Letters*, 81:838, 2002.

- [169] A. Kosiorek, W. Kandulski, H. Glaczynska, and M. Giersig. Fabrication of nanoscale rings, dots, and rods by combining shadow nanosphere lithography and annealed polystyrene nanosphere masks. *Small*, 1:439, 2005.
- [170] Z.Z. Gu, D. Wang, and H. Möwald. Self-assembly of microspheres at the air/water/air interface into free-standing colloidal crystal films. *Soft Matter*, 3:68, 2007.
- [171] J.J. Penninkhof, T. van Dillen, S. Roorda, C. Graf, A. van Blaaderen, A.M. Vredenberg, and A. Polman. Anisotropic deformation of metallo-dielectric core-shell colloids under MeV ion irradiation. *Nuclear Instruments and Methods in Physics Research B*, 242:523, 2006.
- [172] T. van Dillen, E. van der Giessen, P.R. Onck, and A. Polman. Size-dependent ion-beam-induced anisotropic plastic deformation at the nanoscale by nonhydrostatic capillary stresses. *Physical Review B*, 74:132103, 2006.
- [173] A. van Blaaderen. Colloids under external control. *MRS Bulletin*, 29:85, 2004.
- [174] H.R. Ma, W.J. Wen, W.Y. Tam, and P. Sheng. Dielectric electrorheological fluids: theory and experiment. *Advances in Physics*, 52:343, 2003.
- [175] A.P. Hynninen and M. Dijkstra. Phase behavior of dipolar hard and soft spheres. *Physical Review E*, 72:051402, 2005.
- [176] J.P. Hoogenboom, A. Yethiraj, A.K. van Langen-Suurling, J. Romijn, and A. van Blaaderen. Epitaxial crystal growth of charged colloids. *Physical Review Letters*, 89:256104, 2002.
- [177] J.P. Hoogenboom, A.K. van Langen-Suurling, J. Romijn, and A. van Blaaderen. Hard-sphere crystals with hcp and non-close-packed structure grown by colloidal epitaxy. *Physical Review Letters*, 90:138301, 2003.
- [178] B. F. Lyles, S.T. Terrot, P.T. Hammond, and A.P. Gast. Directed patterned adsorption of magnetic beads on polyelectrolyte multilayers on glass. *Langmuir*, 20:3028, 2004.
- [179] M. Trau, D.A. Saville, and I.A. Aksay. Field-induced layering of colloidal crystals. *Science*, 272:706, 1996.
- [180] M. Böhmer. In situ observation of 2-dimensional clustering during electrophoretic deposition. *Langmuir*, 12:5747, 1996.
- [181] R.C. Hayward, D.A. Saville, and I.A. Aksay. Electrophoretic assembly of colloidal crystals with optically tunable micropatterns. *Nature*, 404:56, 2000.
- [182] K.D. Hermanson, S.O. Lumsdon, J.P. Williams, E.W. Kaler, and O.D. Velev. Dielectrophoretic assembly of electrically functional microwires from nanoparticle suspensions. *Science*, 294:1082, 2001.
- [183] C.J.F. Böttcher. *Theory of electric polarization*, volume 1. Elsevier, Amsterdam, 2nd edition, 1973.
- [184] H. Pohl. *Dielectrophoresis: the behavior of neutral matter in non-uniform electric fields*. Cambridge Univ. Press, Cambridge, 1978.
- [185] D.L.J. Vossen, M.J.A. de Dood, T. van Dillen, T. Zijlstra, E. van der Drift, A. Polman, and A. van Blaaderen. Novel method for solution growth of thin silica films from tetraethoxysilane. *Advanced Materials*, 12:1434, 2000.

- [186] D.L.J. Vossen, A. van der Horst, M. Dogterom, and A. van Blaaderen. Optical tweezers and confocal microscopy for simultaneous three-dimensional manipulation and imaging in concentrated colloidal dispersions. *Review of Scientific Instruments*, 75:2960, 2004.
- [187] S. Angus, B. Armstrong, and K.M. de Reuck. *International thermodynamic tables of the fluid state. Carbon dioxide*. Pergamon Press, Oxford, 1976.
- [188] R. Span and W. Wagner. A new equation of state for carbon dioxide covering the fluid region from the triple-point temperature to 1100 K at pressures up to 800 MPa. *Journal of Physical and Chemical Reference Data*, 25:1509, 1996.
- [189] Mikhailov and Borisova. *Polymer Science USSR*, 2:387, 1961.
- [190] P. Staudhammer and W.F. Seyer. The dielectric constant of cis- and trans-decahydronaphthalene and cyclohexane as a function of temperature and frequency. *Journal of the American Chemical Society*, 80:6491, 1958.
- [191] Kaye and Laby. *Tables of physical and chemical constants*. B.
- [192] W.M.Jr. Heston, E.J. Hennelly, and C.P. Smyth. Dielectric constants, viscosities, densities, refractive indices and dipole moment calculations for some organic halides. *Journal of the American Chemical Society*, 72:2071, 1950.
- [193] G. Bosma, C. Pathmamanoharan, E.H.A. de Hoog, W.K. Kegel, A. van Blaaderen, and H.N.W. Lekkerkerker. Preparation of monodisperse, fluorescent PMMA-latex colloids by dispersion polymerization. *Journal of Colloid and Interface Science*, 245:292, 2002.
- [194] M. Trau, S. Sankaran, D.A. Saville, and I.A. Aksay. Electric-field-induced pattern-formation in colloidal dispersions. *Nature*, 374:437, 1995.
- [195] K.S. Cho, D.V. Talapin, W. Gaschler, and C.B. Murray. Designing PbSe nanowires and nanorings through oriented attachment of nanoparticles. *Journal of the American Chemical Society*, 127:7140, 2005.
- [196] A.J. Houtepen, R. Koole, D. Vanmaekelbergh, J. Meeldijk, and S.G. Hickey. The hidden role of acetate in the PbSe nanocrystal synthesis. *Journal of the American Chemical Society*, 128:6792, 2006.
- [197] A.J. Houtepen. *Charge injection and transport in quantum confined systems with disorder*. PhD thesis, Utrecht University, 2007.

## Summary

Colloidal systems are frequently encountered in life. Take for example milk, blood, smoke and foams. Colloidal suspensions are often exposed to an external field, e.g. to gravity, shear flow, confinements or electric fields. These fields can alter their macroscopic properties. It is known that the macroscopic behavior is coupled to the microstructure. Therefore, we examine colloidal dispersions in external fields on a microscopic level. Our systems consist of spherical micron-sized silica or latex particles that are, at least at the beginning, dispersed in a liquid.

At high concentrations colloidal particles can form colloidal crystals. Because the size of colloids is on the order of the wavelength of visible light, colloidal crystals are sometimes called photonic crystals. The regular stacking of particles produces special optical properties caused by diffraction. When the symmetry and the dielectric contrast of such a photonic colloidal crystal are correct, it may even have a photonic bandgap. Such photonic crystals can for example be applicable as optical filters, switches or waveguides. To control structure formation in colloidal suspensions several methods can be used. In this thesis shear flow and an electric field are used to control crystallization.

To examine the effect of shear flow on colloidal dispersions *in situ*, we designed a new parallel plate shear cell with a zero-velocity plane that can be mounted on top of a confocal microscope. In Chapter 2 we described the characterization of this plate-plate shear cell. The plates were microscopy slides. The bottom slide was 24 mm  $\times$  50 mm, the top slide was 15 mm  $\times$  30 mm. They both had a maximum travel of 1 cm and for the systems that we study an oscillatory shear with such a large amplitude can be regarded as a continuous shear. The gap width was variable between 20–200  $\mu\text{m}$ . With a silicone oil in between the plates only fluctuated over a distance 1–2  $\mu\text{m}$  perpendicular to the axis of motion, when they were traversing laterally over a distance of 1 cm. We verified that the flow profile of a dilute suspension of micron-sized silica particles was linear.

We used this setup to examine the behavior of suspensions of micron-sized silica particles in the fluid-crystal coexistence region under shear. These experiments are described in Chapter 3. The flow profile of such a crystallizing colloidal dispersion was not linear. At the walls a sliding layer structure formed of which the local viscosity was 1.5 times smaller than that of the liquid-like structure in the middle of the gap. At low shear rates the hexagonal layers of a crystal that align parallel to the velocity-vorticity plane showed a zigzag motion. We also examined shear melting and crystallization. Shear melting appeared to be a local process in which the local order sometimes increased

and sometimes decreased while the average order decreased. Shear induced crystallization occurred uniformly over the sample and the order increased monotonously.

Chapter 4 deals with colloidal crystalline films fabricated by spin coating. The crystals consisted of micron-sized particles and the structure could be made permanent by polymerizing the dispersing medium. Randomly stacked hexagonal layers formed parallel to the substrate. The particles were sometimes touching and sometimes non-touching. The interparticle spacing probably depended subtly on the surface charge of the particles and the ionic strength of the medium. The symmetry of the structure was as that of a face centered cubic-like crystal. Colloidal crystals formed by sedimentation always have a fluid-like layer on top. Crystals formed by spin coating were different and were crystalline all the way to the top. This is one of the indications that crystal formation started at the air interface with a 2D layer that grew into a 3D multilayer structure while it was sedimenting.

From these spin coated crystals freestanding colloidal crystalline films were made, which is described in Chapter 5. Either the silica particles or the polymer matrix could then be removed without crack formation. With MeV high-energy ion beams freestanding crystalline films of micron-sized silica particles in air were deformed. Again, the crystals stayed crack-free, which is important for their applicability as optical components.

Electric fields can also control colloidal structure formations. In the experiments described in Chapter 6, we used a high frequency alternating current electric field to induce the formation of strings of particles along the field lines. The electric field was applied in a parallel plate capacitor. The bottom electrode contained a 2D pattern, made by positioning silica particles one by one by means of optical tweezers. This template modulated the electric field strength. Depending on the dielectric contrast between the particles and the surrounding medium, the particles were either attracted or repelled from the template. In this way, we could not only control structure formation along the field lines, but also along the gradient of the electric field strength.

We showed that electric field induced crystals can be made permanent by polymerizing the solvent. If the matrix is elastomeric, the structure can subsequently be deformed by a shear. Combining two external fields at the same time will also be possible in our parallel plate shear cell. The setup can be adapted such that an electric field can be applied in addition to a shear flow. This opens up possibilities to make crystals with even different symmetries.



## Samenvatting voor iedereen

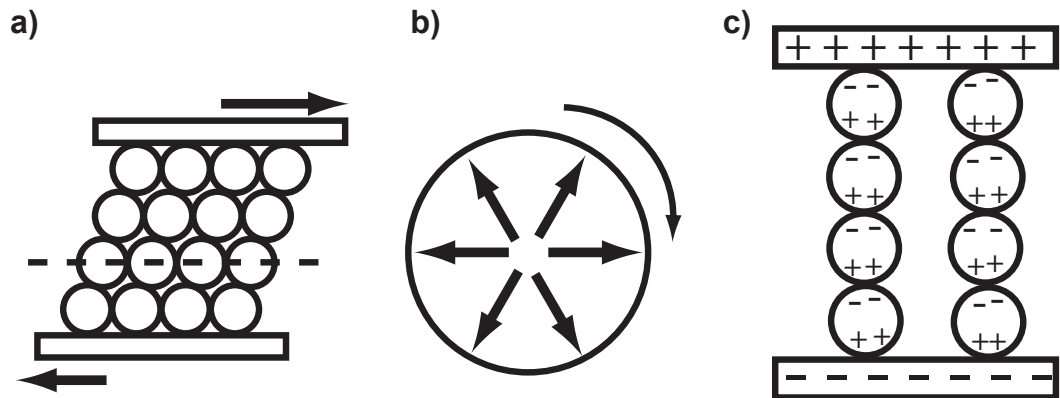
Zonder het ons continu te realiseren, komen we in het dagelijks leven vaak met colloïdale suspensies in aanraking. Bekende voorbeelden zijn melk, bloed, rook en schuim. Wat ze gemeenschappelijk hebben, is dat het microscopisch kleine objecten zijn in een omgeving die gemaakt is van een ander type materiaal: vetdruppels in water, rode bloedlichaampjes in serum, vaste deeltjes in lucht of gas in een vloeistof. In dit proefschrift beperken we ons tot colloïdale suspensies bestaande uit vaste ronde bolletjes van glas of latex die, initieel, in een vloeistof zitten.

De ronde deeltjes kunnen zich in regelmatige structuren of kristallen ordenen. Omdat de deeltjes van dezelfde orde van grootte zijn als de golflengte van zichtbaar licht, worden deze kristallen soms fotonische kristallen genoemd. Afhankelijk van de manier van stapelen en het gekozen materiaal van de deeltjes en hun omgeving, kan een kristal een zogenaamde fotonische “bandgap” hebben. Dit houdt in dat een bepaald spectrum van golflengten van licht, dus een bepaald kleurenspectrum, zich niet door het kristal kan voortplanten. Een dergelijk kristal kan bijvoorbeeld gebruikt worden als een filter voor die kleur licht.

Omdat we zelf willen kunnen bepalen in welk kleureng gebied een dergelijk kristal werkzaam is, willen we controle hebben over kristalvorming. Er bestaan verschillende manieren om dit te doen. In het werk beschreven in dit proefschrift doen we dat door middel van een stromingsveld of een elektrisch veld.

Om de colloïdale suspensies goed gedefinieerd te laten stromen hebben we een speciale opstelling gebouwd. Hij bestaat uit twee glasplaatjes die met een instelbare snelheid in tegengestelde richting langs elkaar bewegen (zie figuur 6.12a). Beide glasplaatjes hebben een oppervlak van enkele vierkante centimeters. De afstand tussen de glasplaatjes is echter slechts een haardikte. De te bestuderen vloeistof met deeltjes gaat stromen door het bewegen van de glasplaatjes. Terwijl het stroomt, meten we de positie van de deeltjes met een microscoop. Om te zorgen dat we een bepaalde groep deeltjes over langere tijd kunnen volgen, moeten we ervoor zorgen dat ze niet uit beeld stromen. Hiervoor is deze opstelling zo gebouwd dat er een vlak is dat niet beweegt ten opzichte van de microscoop. Dit vlak kan op elke gewenste hoogte ingesteld worden. Onder andere om een vlak te creëren dat niet beweegt ten opzichte van de microscoop, is het heel belangrijk dat de platen parallel aan elkaar bewegen. Met deze en andere vereisten is rekening gehouden in het ontwerp en metingen beschreven in hoofdstuk 2 laten zien dat de uiteindelijke opstelling aan de eisen voldoet.

In de in hoofdstuk 3 beschreven experimenten hebben we deze opstelling



**Figuur 6.12:** a) De opstelling om een colloïdale suspensie goed gedefinieerd te laten stromen bestaat uit twee glasplaatjes die in tegengestelde richting langs elkaar bewegen. Bij lage stromingssnelheden ordenden de deeltjes zich in lagen. De gestippelde lijn is een vlak dat niet beweegt ten opzichte van de microscoop. b) Deeltjes kunnen ook geordend worden door ze op een ronddraaiende plaat te leggen waardoor ze radieel naar buiten geslingerd worden. c) Een elektrisch veld kan voor een ongelijke verdeling van + en - ladingen zorgen, waardoor deeltjes ketens kunnen vormen.

gebruikt om een suspensie met een groot aantal deeltjes per volume-eenheid in een stromingsveld te bestuderen. De concentratie van deeltjes was in deze suspensie zo hoog, dat de deeltjes zonder een stromingsveld geordende kristallijne gebiedjes begonnen te vormen. Door een langzame stroming oriënteerden deze gebiedjes zich in dezelfde richting waardoor een groot kristallijn gebied ontstond. Was de stroming echter snel, dan werden de geordende gebieden stuk gemaakt en “smolt” het kristal. De deeltjes waren weer wanordelijk verspreid over de ruimte. Hoe dit in zijn werk ging, hebben we kwantitatief onderzocht. Het was interessant om te zien dat kristalliseren en smelten in een stromingsveld anders verlopen dan zonder een stromingsveld.

In plaats van stroming in één richting, kun je een vloeistof ook vanuit een punt radieel naar buiten laten stromen, net als in een centrifuge (zie figuur 6.12b). Deze vorm van stroming is in hoofdstuk 4 gebruikt om dunne films van geordende colloïden in een vloeistof te maken. Een druppel werd in het midden van een rond platliggend glaasje gelegd dat vervolgens snel rond werd gedraaid. De deeltjes ordenden zichzelf in lagen parallel aan het glaasje. Door een vloeistof te gebruiken die onder invloed van ultraviolet licht hard wordt, konden de deeltjes vastgezet worden zodat de structuur permanent werd.

Een op deze wijze gemaakte dunne film van geordende deeltjes bleek na permanent maken van de structuur, hard én flexibel genoeg te zijn om los te halen van het glaasje. Het is niet triviaal om een zichzelf ondersteunende film van geordende colloïdale deeltjes te maken, maar het is wel belangrijk voor toepassingen. Hoe we dit voor elkaar hebben gekregen en wat we verder met deze zichzelf ondersteunende films gedaan hebben, staat beschreven in

hoofdstuk 5.

In de experimenten van hoofdstuk 6 hebben we een elektrisch veld gebruikt om controle uit te oefenen over structuurvorming. De deeltjes bezitten zowel positieve als negatieve ladingen, maar netto zijn ze neutraal geladen. Het elektrisch veld zorgt ervoor dat aan de ene kant van het deeltje meer + ladingen gaan zitten en aan de andere kant meer - ladingen. De + en - geladen kanten van verschillende deeltjes trekken elkaar aan, zodat de deeltjes ketens vormen (zie figuur 6.12c). De elektroden van de cel waarmee we het elektrisch veld aanleggen, zijn vlakke glaasjes met een geleidende coating. Op een van de twee elektroden hebben we deeltjes in een regelmatig patroon gelegd. Dit hebben we met een optische pincet gedaan, een intense gefocusseerde laserbundel. Stuk voor stuk pakten we met deze optische pincet een microscopisch klein deeltje en we plaatsten deze op de toekomstige elektrode. Dit patroon van deeltjes beïnvloedde de lokale elektrische veldsterkte. Afhankelijk van het onderzochte systeem vormden de ketens van deeltjes zich juist wel of niet bovenop dit patroon.

We hebben met al deze experimenten verschillende methoden laten zien om controle uit te oefenen over de structuurvorming van microscopisch kleine deeltjes, namelijk door middel van een stroming of een elektrisch veld. Deze twee of nog andere externe velden zijn ook te combineren. Dit geeft ons de mogelijkheid om in de toekomst structuren met weer een andere symmetrie te maken, al naar gelang de vereisten voor hun toepassing.



# Dankwoord

Het is bijna niet te geloven, maar het is af. Dit proefschrift is niet het enige dat ik aan de afgelopen vier jaar heb overgehouden. Aan mijn tijd in de Soft Condensed Matter groep hou ik ook een heleboel leuke herinneringen over. Voor beide wil ik een aantal mensen bedanken.

Allereerst, wil ik mijn promotor Alfons van Blaaderen bedanken. De vier jaren waren veel te kort om al je ideeën uit te voeren, maar saai waren ze daardoor allerm minst! Arnout Imhof, zeker voor shear-gerelateerde onderwerpen was je een onmisbare factor. Dank je wel voor de discussies die we hierover hadden en je realisme met betrekking tot de tijd die een mens nodig heeft om een experiment uit te voeren. Ik ben blij dat je mijn co-promotor was.

Vervolgens wil ik iedereen van het IGF bedanken die geholpen heeft bij het vervaardigen van Hippos. In het bijzonder wil ik hier Joost Brand voor bedanken. Zonder de shear cell had dit proefschrift er heel anders uit gezien. Ik heb af en toe flink op de shear cell lopen vloeken, maar als je er handigheid mee krijgt, blijkt het een prachtig meetinstrument te zijn en ik denk dat velen na mij nog veel plezier van deze shear cell zullen hebben. Mijn complimenten voor dit resultaat en bedankt voor alle tijd die je erin gestoken hebt. Hans Wisman, dank je wel voor het werk aan de elektronica, want zonder besturingsprogramma ben je nergens.

Met mijn directe collega's binnen de Soft Condensed Matter groep had ik het niet beter kunnen treffen. Er is altijd wel iemand om je te helpen, bijvoorbeeld Carlos van Kats om te helpen bij het openen van een fles APS, Dirk Vossen of Astrid van der Horst voor alles betreffende de tweezers, Didi Derks voor het analyseren van de bananen en kamelen, Mirjam Leunissen om uit te leggen hoe je via vier(!) programma's een geschikt plaatje maakt. Verder waren er natuurlijk de onmisbare kopjes groene thee, de roddels op het lab, de tafeltenniswedstrijdjes die soms wel een best of 25 werden, de etentjes, uitstapjes naar SEM, plasma etser, ellipsometer, ijsbaan of theater. En midden in de nacht in de gang van een oud klooster sake drinken doe je ook niet elke dag. Job Thijssen, Esther Vermolen, Rianne van Eerd, Roel Dullens, Leonard Kraaijenbrink, Carmen Zoldesi, Andrea Fortini, Peter van Oostrum, Teun Vissers en andere groepsgenoten het was gezellig! Ook mijn kamergenoten Joan Penninkhof, Johan Stiefelhagen, Dannis 't Hart en Astrid van der Horst wil ik bedanken voor de gezelligheid. Minder groot is mijn dank voor de kennismaking met Pink Floyd, maar misschien kom ik daar nog overheen, want -het is ongeloofelijk maar waar- Origin begin ik ook steeds meer te waarderen.

Binnen de kortste keren wist iedereen van de groep dat ik tafeltennis. Per-

soonlijk vind ik tafeltennis een van de slechtste sporten om je verstand op nul te zetten. De ontspanning die ik ervan kreeg, heb ik dan ook voornamelijk aan de mensen eromheen te danken: iedereen van Docos, Play Fair en de trainingsgroep in Amsterdam, hopelijk kunnen we binnenkort weer een balletje gaan slaan. SAYUSA-teamies Sabrina Mac Mootry en Saskia van der Gugten; Sheila Tol, Nadia Huizer en coach Wim Jägers, dank voor jullie luisterende oren waar mijn verhaal dan ook over ging. Ik heb waardering voor al jullie pogingen te begrijpen wat ik die vier jaar deed en vooral waarom. Ik rij graag nog een keertje de wereld met jullie rond.

Het is allemaal niet gemakkelijk geweest, maar gelukkig komt het Walt Disney type einde ook in de werkelijkheid voor. Mam, pap en Yu San, het was fijn te weten dat jullie ook geloofden in de strakke planning die ik aan het einde noodgedwongen volgde. Ik ben blij dat we nu samen van het resultaat en vooral van de tijd hierna kunnen genieten.

# Curriculum vitae

Yu Ling Wu was born on 18 June 1980 in Amsterdam, the Netherlands. After she obtained her “VWO diploma” in 1998 at het Stedelijk Gymnasium in Haarlem she started studying Chemistry at the University of Amsterdam (UvA). In her final year she did her research project under the supervision of dr. Erika Eiser in the Complex Fluid group. She examined the phase behavior of the amphiphilic tri-block copolymers Pluronic F68 and F108. In 1999 she received a grand from the Association of the Dutch Chemical Industry (Vereniging Nederlandse Chemische Industrie (VNCI)) for her results as a chemistry student. In October 2002 she obtained her masters degree with honors.

From 2003 until 2007 she worked in the Soft Condensed Matter Group at the Utrecht University of prof. dr. A. van Blaaderen as a PhD student. She examined how to control colloidal crystallization by shear and electric fields. Techniques that she used were among others confocal scanning laser microscopy and optical tweezers. The work resulted in this thesis.